

IOWA STATE UNIVERSITY

Digital Repository

Graduate Theses and Dissertations

Iowa State University Capstones, Theses and
Dissertations

2018

Jet longitudinal double spin asymmetry in PHENIX $p+p \sqrt{s} = 510 \text{ GeV}$

Milap Patel
Iowa State University

Follow this and additional works at: <https://lib.dr.iastate.edu/etd>

 Part of the [Physics Commons](#)

Recommended Citation

Patel, Milap, "Jet longitudinal double spin asymmetry in PHENIX $p+p \sqrt{s} = 510 \text{ GeV}$ " (2018). *Graduate Theses and Dissertations*. 16739.
<https://lib.dr.iastate.edu/etd/16739>

This Dissertation is brought to you for free and open access by the Iowa State University Capstones, Theses and Dissertations at Iowa State University Digital Repository. It has been accepted for inclusion in Graduate Theses and Dissertations by an authorized administrator of Iowa State University Digital Repository. For more information, please contact digirep@iastate.edu.

Jet longitudinal double spin asymmetry in PHENIX $p + p\sqrt{s} = 510 GeV$

by

Milap Patel

A dissertation submitted to the graduate faculty
in partial fulfillment of the requirements for the degree of

DOCTOR OF PHILOSOPHY

Major: Nuclear Physics

Program of Study Committee:
John Lajoie, Major Professor
Marzia Rosati
Adam Kaminski
David Atwood
Nathan Neihart

The student author, whose presentation of the scholarship herein was approved by the program of study committee, is solely responsible for the content of this dissertation. The Graduate College will ensure this dissertation is globally accessible and will not permit alterations after a degree is conferred.

Iowa State University

Ames, Iowa

2018

Copyright © Milap Patel, 2018. All rights reserved.

DEDICATION

I would like to dedicate this thesis to my parents for providing me with an amazing life. You guys are awesome! Also to all the friends and colleagues who helped me throughout my thesis work.

TABLE OF CONTENTS

LIST OF TABLES	vii
LIST OF FIGURES	viii
ACKNOWLEDGEMENTS	xiv
ABSTRACT	xv
CHAPTER 1. OVERVIEW	1
1.1 Introduction	1
1.2 Brief History	1
1.3 The Standard Model	3
1.4 Proton Structure	4
1.4.1 Proton Spin Structure	7
1.5 Gluon Spin Contribution	11
1.6 Jets	12
1.6.1 Jet Reconstruction Algorithms	17
1.7 Kinematics	19
1.7.1 Variables	19
1.7.2 Jet Variables	21
CHAPTER 2. THE EXPERIMENT	22
2.1 RHIC	22

2.2	Polarization	22
2.2.1	Siberian Snakes	24
2.2.2	Polarimetry	25
2.3	PHENIX	29
2.3.1	BBC	29
2.3.2	Drift Chamber	30
2.3.3	Pad Chambers	30
2.3.4	Electromagnetic Calorimeter	31
2.4	Ring-Imaging Cherenkov Detector	32
2.5	Data Acquisition and Triggers	32
2.5.1	Minimum Bias Trigger	33
2.5.2	EMCal/RICH Trigger	34
CHAPTER 3. DATA ANALYSIS		40
3.1	Run Quality Assurance	40
3.1.1	DAQ Condition	41
3.1.2	Spin Database and Polarization	41
3.2	Event Selection	41
3.3	Track Selection	42
3.3.1	Modified Quality Cut	42
3.3.2	Pair Cut	44
3.3.3	EMCal and PC3 Matching	45
3.3.4	Secondary Track Cuts	46
3.4	Cluster Selection	48
3.4.1	EMCal Hot/Dead Map	48
3.4.2	Cluster Cuts	49
3.4.3	Time of Flight	50
3.4.4	Cluster-track Matching	50

3.5	Jet Reconstruction	51
3.5.1	Jet Level Cuts	51
3.6	Fake Jets Subtraction	52
3.7	Spin Sorting	54
3.7.1	Spin Pattern	55
3.7.2	Relative Luminosity	55
3.7.3	Beam Polarization	56
3.7.4	Fake Jet Subtraction for Spin Pattern	56
CHAPTER 4. SIMULATIONS		58
4.1	Pythia	58
4.2	PISA	59
4.3	Jet p_T Binning	59
4.4	Simulation Acceptance	60
4.5	Cuts on True Jets	60
4.6	Different Kinematic Simulations	60
CHAPTER 5. PATH TO FINAL RESULTS		66
5.1	Combining Different Response Matrices	66
5.1.1	Ladder Method	66
5.1.2	Cross Section Scaling	67
5.2	Unfolding	69
5.2.1	Singular Value Decomposition	70
5.3	Iterating Input	74
5.4	Different Cuts	74
5.5	Cross Section	75

5.6	A_{LL}	76
5.6.1	Bunch Shuffle	77
5.6.2	Unfolding Systematic	78
5.6.3	Fakejet Systematic	78
5.6.4	Result	78
BIBLIOGRAPHY		90

LIST OF TABLES

Table 3.1	Bits used by each DC wire and PC1 hit.	42
Table 3.2	Spin Pattern Grouping	55
Table 3.3	Weighted Relative Luminosity	56
Table 3.4	Average Polarization	56
Table 5.1	Table of cross section and average $p_{T, True}$ for each bin. Note: Only bins 4-9 are shown in Figure 5.7.	77
Table 5.2	Table of A_{LL} values for each x_T . Note: the last two bins were not show in Figure 5.14	79
Table 5.3	Table of raw A_{LL} values for each x_T . Note: the last four bins were not show in Figure 5.14	79

LIST OF FIGURES

Figure 1.1	The particles in the Standard Model are the building blocks of visible matter in the universe[54].	5
Figure 1.2	Feynmann diagram for deep inelastic scattering a lepton from a proton.	6
Figure 1.3	World data set of proton structure function $F_2(x)$ vs Q^2 at various x [54][35].	8
Figure 1.4	EMC result of the $g_1(x)$ integral and the Ellis-Jaffe sum rule prediction[13].	10
Figure 1.5	Gluon helicity distribution for $Q^2 = 10GeV^2$. The red line shows the DSSV analysis fit for all PHENIX and STAR data until 2009. The blue and black lines using older data (as described in [28]). The dotted lines show 90% confidence interval. The vertical dashed lines show the PHENIX x range $0.05 \leq x \leq 0.2$.	13
Figure 1.6	The integral of Δg over different x ranges. The different points correspond to different data sets as described by [28] and in Figure 1.5. Horizontal axis shows the range where the RHIC data sets help contribute to the calculation, and thus has smaller uncertainty. . .	14
Figure 1.7	Blue points are from $\sqrt{s} = 200GeV$ and red points are $\sqrt{s} = 510GeV$ measured by STAR.	15
Figure 1.8	Part (a) shows an event with two hard partons reconstructed as two jets. Part (b) shows an event with one of the partons emitting a soft gluon, causing an IRC unsafe algorithm to reconstruct all the particles as one jet.	17

Figure 1.9	The coordinate system used in the analysis.	20
Figure 2.1	The RHIC compound and its components.	23
Figure 2.2	Procedure to produce the polarized Hydrogen beam[61].	24
Figure 2.3	The spin vector should precess in the y-direction, but will gradually increase in radius with successive orbits without the Siberian snakes.	25
Figure 2.4	The orbit and spin vector of the particle as it passes through the Siberian Snake. The spin vector is rotated 180°.	26
Figure 2.5	The beamline view of the pC polarimeter with the Carbon target in the center. The recoil Carbon atoms are measured by the six Silicon detectors.	27
Figure 2.6	Experimental setup of ZDC at PHENIX (not to scale)[5].	28
Figure 2.7	This shows an example of the blue and yellow beams having spin vectors in the opposite direction of velocity, hence a (--) configuration.	28
Figure 2.8	This table shows the different spin patterns in Run 13 data set.	29
Figure 2.9	Top is the view along the beamline and bottom is perpendicular to the beamline.	35
Figure 2.10	(a) Single BBC element. (b) Array of 64 elements. (c) BBC mounted in PHENIX, encircling the beam pipe[11].	36
Figure 2.11	Cartoon for a collision seen by BBC[52].	36
Figure 2.12	Left: The DC frame and keystones with wire direction. Middle: X, U, V wire orientations. Right: The different wire layers on keystones[6].	36
Figure 2.13	Cross section of a pad chamber. The anode wires are in front of the pad detectors[6].	37
Figure 2.14	Left: Process of PbSc as a photon or electron enters detector. Right: A PbSc module consisting of 4 towers[12].	37
Figure 2.15	Overview of a PbGl supermodule[12].	38

Figure 2.16	Cutaway view of an arm of the PHENIX RICH detector[10].	38
Figure 2.17	Schematic of the data collection flow in PHENIX.	39
Figure 2.18	Diagram of the procedure for the ERT trigger[60].	39
Figure 3.1	Shows the alpha vs. board for the X2 bit used. East (E) or west (W) is the arm, north (N) or south (S) is positive or negative z along beam axis.	43
Figure 3.2	Similar to figure 3.1, but X2 bad or inefficient areas have been cut out and recorded for use for the modified quality cut.	44
Figure 3.3	This shows the alpha vs. board using the quality (63 31) condition.	45
Figure 3.4	This shows the alpha vs. board using the modified quality condition.	46
Figure 3.5	Top row shows the mean and sigma vs p_T for the EMCAL $d\phi$, while the bottom row shows the signalized mean and sigma vs p_T for EMCAL $d\phi$ calibration. The calibration brings the mean to ~ 0 and the sigma ~ 1 for all the p_T bins.	47
Figure 3.6	Red lines show the cut for the edge regions.	48
Figure 3.7	Ratio of Energy/Momentum of the electron candidates.	49
Figure 3.8	Hot/Dead for each EMCAL sector.	50
Figure 3.9	The Time of Flight distribution for EMCAL clusters.	51
Figure 3.10	The area between the red lines is the good region which is kept.	52
Figure 3.11	The top is the total jets found in black points, the fake jets in red, and the subtracted distribution in green. The bottom shows the ratio of fake jets divided by the total jets.	53
Figure 3.12	The empty region in the last 9 bins in the y-axis are the abort gap. This means that no collisions occurred and hence no events in that crossing ID.	54

Figure 3.13	The left side shows blue helicity of -1 , which is when the spin is in the opposite direction of the velocity. The right side shows yellow helicity of $+1$, i.e. spin in same direction as velocity. This event would be spin pattern 1, according to Table 3.2	55
Figure 3.14	Left plot is spin pattern 0, right is spin pattern 1.	57
Figure 3.15	Left plot is spin pattern 2, right is spin pattern 3. Top plots are the total jets in black, fake jets found in red, and the subtracted in green. The bottom plots are the ratio of fake jets found to the total jets found for each bin.	57
Figure 4.1	This shows the normalized histograms of the hits in the data on the left and the simulation hits on the right. The empty regions are the bad regions of the Drift Chamber and are similar in the simulations and data. Top plots are the NE and NW sections of the DC. SE and SW are shown below in Figure 4.2. E and W denote the different arms while N and S are north or south of the collision point in z-axis (along beam line).	61
Figure 4.2	The SE and SW sections of the DC modified quality cut. The left is from data and right is from simulations.	62
Figure 4.3	This is the 4 EMCal sectors of the west arm. The left plot is clusters in data while the right plot shows the clusters in the simulations. .	63
Figure 4.4	This is the 4 EMCal sectors of the east arm. Sectors 4 and 5 are the two PbGl sectors. The left plot is clusters in data and the right plot is clusters in simulation, as in Figure 4.3 for the west arm.	64

Figure 5.1	Top left starts with the $\text{ckin}(3) = 5$ and $\text{ckin}(3) = 40$ unscaled matched true p_T histograms. The higher $\text{ckin}(3)$ histogram is integrated above the bin where the distribution starts to fall. The higher $\text{ckin}(3)$ histogram is scaled using the ratio of integrals (of the histograms) then added using the weighted sum. The resulting histogram is then used to combine the next higher value $\text{ckin}(3)$. Like taking steps up a ladder.	68
Figure 5.2	The $\log d_i \text{ vs } i$ for unfolding the total reconstructed jets shows the behaviour of exponential drop until leveling out ~ 1	72
Figure 5.3	The top plot is unfolding using different k regularization values. The bottom shows the ratio of the different k regularization to chosen value of $k = 9$. There is a clear difference at the high p_T with different k	73
Figure 5.4	The ratio of the unfolded/true for the standard cuts for each iteration.	74
Figure 5.5	The raw jet distribution for the six different cuts described. These are not ERT trigger efficiency corrected.	76
Figure 5.6	The response matrix 1a) is for standard cuts, 1b) for the 2.5σ cut, 2a) for the 1.5σ cut, 2b) for the DC conversion cuts, 3a) for the tighter CF cut, and 3b) for the combination of 3 cuts.	80
Figure 5.7	The top plot is showing the unfolded cross section with the different cuts as well as the theory predictions. The bottom plot is showing the ratio of the standard cut to the different cuts. The cross section points are plotted at the p_T weighted mean.	81
Figure 5.8	$\frac{A_{LL}}{\text{Error}_{A_{LL}}}$ for each p_T bin.	82
Figure 5.9	Means of Gaussian fit (shown in Figure 5.8 for each bin.	83
Figure 5.10	Sigmas of Gaussian fit (shown in Figure 5.8 for each bin.	84

Figure 5.11 This shows the unfolded A_{LL} for the different sigma cuts. The high p_T points are driven more by the unfolding than data and the red line shows the bin boundary.	85
Figure 5.12 The unfolded with higher energy cuts (in red) is scaled up to match the default (blue) at high p_T	86
Figure 5.13 The unfolded with higher energy cuts (in red) compared to the default (blue).	87
Figure 5.14 The STAR points, theory curves, and the raw and unfolded points are shown in this figure. The blue and red points are the previous STAR measurements, the dashed lines are from theory curves. The pink points are from the unfolded points. The grey band on the pink points is the unfolded systematic, discussed in Section 5.5. The range shown is within the range of high statistics.	88
Figure 5.15 This is shows the points of the larger $x_{T, True}$ range of Figure 5.14 .	89

ACKNOWLEDGEMENTS

I would like to take this opportunity to express my thanks to those who helped me with various aspects of conducting research and the writing of this thesis. First, Dr. John Lajoie for his guidance, patience, and support throughout this research. Second, the collaborators in the MPC-EX and spin groups who also helped guide and assisted me in my research work throughout the PhD. And finally, to the friends who helped keep me sane during grad school.

ABSTRACT

The longitudinal double-spin asymmetry (A_{LL}) in spin-polarized $p+p$ collisions provides insight into the gluon contribution to the proton's spin by accessing the gluon helicity distribution Δg . Prior PHENIX π^0 and STAR jet A_{LL} measurements show a non-zero asymmetries and hence indicate a nonzero Δg in an NLO analysis. The STAR measurements of jet A_{LL} in $\sqrt{s} = 200$ and 510 GeV polarized $p+p$ collisions provide the strongest constraints on Δg at intermediate to high x . A measurement of the jet A_{LL} at $\sqrt{s} = 510$ GeV in PHENIX will provide an important cross-check. This thesis will detail the jet reconstruction techniques tuned for the PHENIX detector and present the measured jet A_{LL} .

CHAPTER 1. OVERVIEW

1.1 Introduction

The Standard Model describes the different elementary particles which compose known matter and the forces which govern our universe. There was a long process of discovery which led to the Standard Model and modern day physics. This chapter goes through this history of discovery and details the importance of this analysis.

1.2 Brief History

The proton was named by Ernest Rutherford and was thought to be a fundamental particle. It had been observed that other elements were composed of the same proton as found in the hydrogen atom. The first hint that there could be an internal structure of the proton came from measuring it's magnetic moment in 1933[44]. The measured magnetic moment was different from the prediction by Paul Dirac's theory for point-like spin $\frac{1}{2}$ particles. The Dirac equation is a relativistic version of Schrodinger's equation and predicts the magnetic moment is given by:

$$\mu = g \frac{e}{2M} \frac{\hbar}{2}, \quad (1.1)$$

where e is electric charge, M is the mass of particle, \hbar is Planck's constant divided by 2π , and $g \cong 2$. The g-factor has been measured to incredible accuracy. The g-factor of the electron is -2.00231930436182 (± 0.00000000000052), while the proton g-factor is 5.585694702 (± 0.000000017)[53]. This deviation by the proton along with discovery of new

hadrons challenged the notion of which particles were truly fundamental.

In 1964, Gell-Mann and George Zweig independently proposed that hadrons were composite particles composed of more fundamental particles, *quarks*.¹ The proposed quark model composed of three quarks: the *up* quark (*u*) with charge $\frac{2}{3}$, the *down* quark (*d*) with charge $-\frac{1}{3}$, and the *strange* quark (*s*) with charge $-\frac{1}{3}$. Each quark had a corresponding anti-quark with opposite charge and all had spin $\frac{1}{2}$. Baryons and mesons were composed of quarks by combination rules:

- Baryons are composed of three quarks and anti-baryons are composed of three anti-quarks.
- Mesons are composed of a quark and an anti-quark.

The quark model made great successes from explaining the baryon and meson resonances. However, there were flaws in the model. For one, no one had discovered any individual quarks. They should be easy to produce since they composed baryons and easy to detect since they had fractional electric charge. There was also the issue spin statistics for fermions. Since quarks were half-integer spin, they cannot occupy the same state, and thus baryons should not be allowed. The solution around this was proposed by O.W. Greenburg, who postulated that the quarks carried a color charge. The quarks came in three flavors of *u*, *d*, and *s*, as well as three different colors: red, green, and blue. With this new color charge, the quarks would have a new degree of freedom and thus three different states to not violate the Pauli Exclusion Principle.

Bjorken and Glashow had also introduced a fourth quark: *charm* (*c*)[19]. By 1974, four leptons (*e*, ν_e , μ , ν_μ) had been detected in laboratories and a universe with four leptons and quarks was a harmonic picture. However, without any detection of the quarks, there were many skeptics who had written off the quark model. What rescued it was the discovery of the *J/ψ* in November 1974. The *J/ψ* was discovered independently by two separate

¹Zweig referred to them as *aces*, but that name did not catch on.

research groups, one at Stanford Linear Accelerator Center (SLAC) led by Burton Richter and the other at Brookhaven National Laboratory (BNL) led by Samuel Ting[15][14]. The J/ψ had two surprising features: it had a long lifetime (about 1000 times larger than a particle of comparable mass should) and it was extremely heavy (3.1 GeV, about three times heavier than the proton). There were additional mesons discovered in quick succession after the J/ψ , in particular the ψ' (psi-prime). There was much theoretical speculation on the explanation of the new discovery, but in the end the quark model provided the most convincing explanation: the J/ψ was a bound state of charm and anti-charm quarks, i.e. $J/\psi = (c\bar{c})$. The upsilon was discovered in 1977 and recognized as a bound state of a new quark, the bottom (b), $\Upsilon = b\bar{b}$ [38]. It became clear from these discoveries that the quark model was indeed correct. The discovery of the sixth quark, the top (t), was finally made in 1995 at Tevatron[2].

1.3 The Standard Model

The grouping of elementary particles and the theory describing the electromagnetic, weak, and strong interactions is known as the Standard Model[39]. There are twelve basic building blocks for all visible matter: six quarks and six leptons, which are all fermions of spin $\frac{1}{2}$. The forces between them are carried by gauge bosons: photons for electromagnetic interactions, gluons for strong interactions, and W^\pm and Z for the weak interactions. Figure 1.1 shows the table of Standard Model particles. The baryons (antibaryons) are bound states of three quarks (antiquarks) and mesons are bound states of a quark and antiquark.

Mathematically, the Standard Model is a quantum field theory[57]. It is invariant under local transformations of the gauge symmetry group $SU(3)_C \otimes SU(2)_L \otimes U(1)_Y$, where C is for color charge, L for weak isospin, and Y for hypercharge. The $SU(3)$ gauge symmetry describes the field theory known as Quantum ChromoDynamics (QCD) while the $SU(2)_L \otimes U(1)_Y$ symmetry group describes the electromagnetic interaction and electroweak interaction. The field theory of electromagnetism is known as Quantum ElectroDynamics

(QED). There are key differences which arise due to the gauge symmetry differences between QCD and QED.

QCD describes strong interactions among quarks and gluons, which is important in hadron collisions. In QCD, the gluons carry color charge which means they can self-interact. In QED, the photons are electrically neutral and so do not self-interact (to first order). The QCD color charge comes in three flavors: red, green, or blue. The QED electric charge is either positive or negative. There are no color charged particles found individually and quarks must combine to form colorless particles, which is known as confinement. As the distance between two color-charged particles increases, the strength of the strong force increases. There is little color force at short distances or high momentum transfers and so the quarks behave like free particles within a confining boundary. This property is called asymptotic freedom. This is in stark contrast to QED, which diminishes in force with distance. Confinement and asymptotic freedom unique features of QCD which determine the behavior of quarks and gluons in particle reactions at different energy scales.

The Higgs boson[1] is the latest particle discovered which is in the Standard Model, however the Standard Model is not yet complete. It does not include gravitational force nor does it explain the existence of dark matter and dark energy, and also fails to explain the matter-antimatter asymmetry in the universe. This analysis focuses on better understanding the spin structure of the proton, which has yet to be fully understood.

1.4 Proton Structure

Deep Inelastic Scattering (DIS) experiments at SLAC were the first to probe the proton and determine that it contained an internal structure[20][22]. The measured angular distribution of the cross-section did not agree with a point-like cross-section, indicating that the proton is not point-like. DIS is a lepton-hadron scattering process in which the lepton, usually an electron, is scattered from a quark in the proton. The process is shown in Figure 1.2. The p is the proton, q is the momentum of a parton within the proton, and $k_{i(f)}$ is the

Standard Model of Elementary Particles

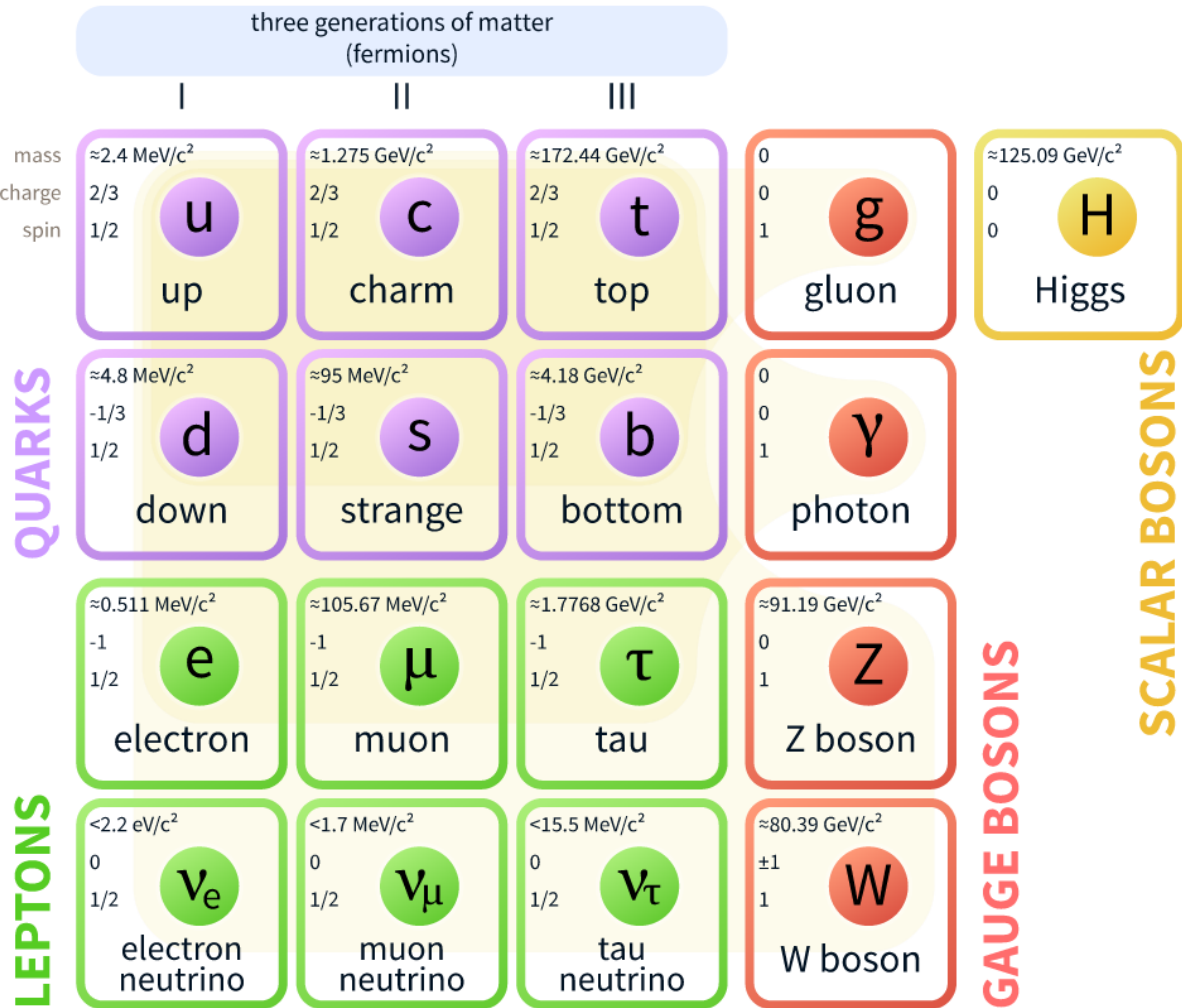


Figure 1.1: The particles in the Standard Model are the building blocks of visible matter in the universe[54].

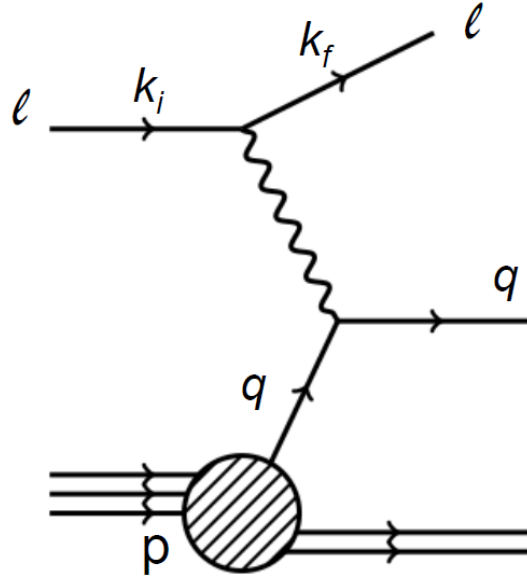


Figure 1.2: Feynmann diagram for deep inelastic scattering a lepton from a proton.

momentum of the incoming (outgoing) lepton. The momentum transfer is written as:

$$Q^2 \equiv -q^2 = k_i^2 - k_f^2 (q^2 < 0) \quad (1.2)$$

$$\nu \equiv E - E' \quad (1.3)$$

$$x = \frac{Q^2}{2p \cdot q} \quad (1.4)$$

Q^2 is the square of momentum transfer of the lepton and parton, ν is the energy carried by the virtual photon where $E(E')$ is the incident (scattered) lepton energy. The four-momentum fraction of the interacting parton is the Bjorken variable x . The momentum transfer (Q^2) defines the resolving power of the lepton probe, i.e. larger energy of lepton means wavelength of lepton is smaller than size of the proton.

The cross section of inelastic electron-proton scattering in the laboratory frame can be written as:

$$\frac{d^2\sigma}{d\Omega dE'} = \left(\frac{d\sigma}{d\Omega} \right)_{Mott} \left(W_2(\nu, Q^2) + 2W_1(\nu, Q^2) \tan^2 \left(\frac{\theta}{2} \right) \right) \quad (1.5)$$

where the Mott cross-section is that of a relativistic electron ($E_e \gg m_e$) scattering, the θ is the scattering angle of the electron, and W_1 and W_2 are the structure functions. James Bjorken proposed that the structure function only depends on x at large Q^2 (called Bjorken scaling), meaning that the proton was composed of point-like particles. Thus,

$$\lim_{Q \rightarrow \infty} MW_1(\nu, Q^2) = F_1(x) \quad (1.6)$$

$$\lim_{Q \rightarrow \infty} \nu W_2(\nu, Q^2) = F_2(x) \quad (1.7)$$

The SLAC result confirmed this Bjorken scaling behavior by measuring the structure function for various Q^2 for fixed x . It was recognized that quarks and gluons are the partons which make up the proton[49].

The unpolarized structure function $F_2(x, Q^2)$ was measured by several DIS experiments: SLAC, Fermi National Laboratory (FNAL), CERN², and at DESY³. Figure 1.3 shows the structure function measured at various x . $F_2(x, Q^2)$ is almost independent of Q^2 above $0.08 < x < 0.4$, indicating the point-like particles in the proton. This doesn't hold at lower x , where the structure function is not flat in Q^2 . This is known as Bjorken scaling violation and is resolved by the existence of gluons. The low x region is when gluons become more visible, inferred from the lack of quark-lepton interactions compared to higher x regions. This low x region is a tool to study gluons inside the proton. However, to directly study gluons, proton-proton collisions with strong interactions are needed.

1.4.1 Proton Spin Structure

Since spin is a fundamental property and the proton is composed of fundamental particles, the question of how the proton spin is carried by its constituent particles is important to understanding QCD. It was expected that the spin $\frac{1}{2}$ valence quarks (uud) would combine to sum the proton spin of $\frac{1}{2}$. Polarized DIS experiments were done to measure the

²Organisation Europeenne pour la Recherche Nucleaire

³Deutsches Elektronen-Synchrotron

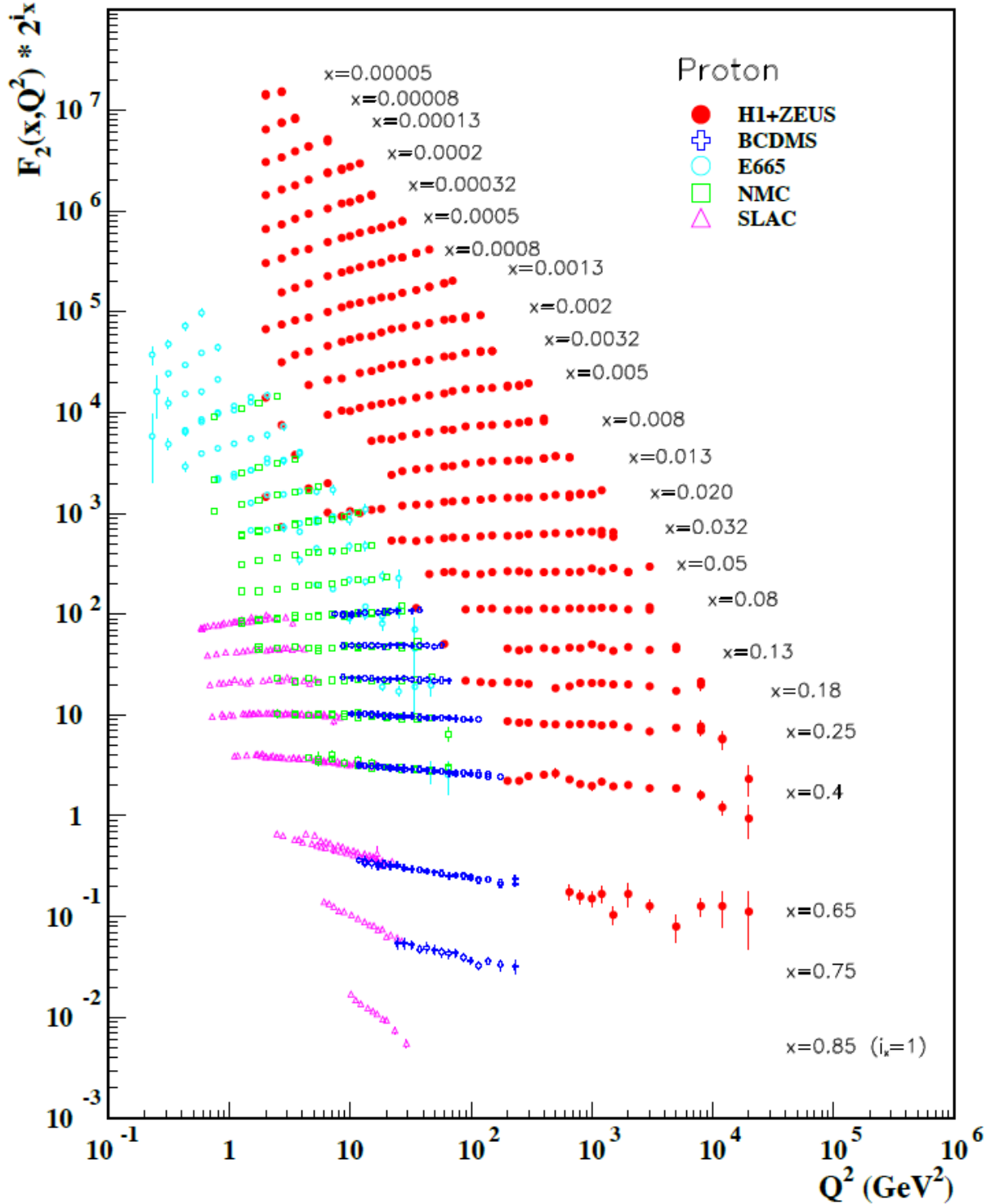


Figure 1.3: World data set of proton structure function $F_2(x)$ vs Q^2 at various x [54][35].

spin-dependent nucleon structure function $g_1(x, Q^2)$, analogous to the unpolarized structure function. The $g_1(x, Q^2)$ nucleon structure function appears as the difference of polarization cross sections and can be measured by asymmetry:

$$A_1 = \frac{d\sigma^{+-} - d\sigma^{++}}{d\sigma^{+-} + d\sigma^{++}} \quad (1.8)$$

where $+-$ ($++$) means the helicities of lepton and proton are opposite (same). The $g_1(x, Q^2)$ can be obtained using the relation:

$$A_1 = \frac{g_1(x, Q^2)}{F_1(x, Q^2)} \quad (1.9)$$

In 1988 the European Muon Collaboration (EMC) at CERN measured the quark contribution to proton spin using longitudinally polarized muon beam scattering from a longitudinally polarized proton target (polarized DIS)[13]. The measured quantity $xg_1(x, Q^2)$ integrated over x at mean Q^2 of $10.7 GeV^2$ gives:

$$\int_0^1 g_1(x) dx = 0.114 \pm 0.012(stat.) \pm 0.026(syst.) \quad (1.10)$$

Figure 1.4 shows the $g_1(x)$ results along with the theoretical prediction from the Ellis-Jaffe sum rule. The Ellis-Jaffe sum rule[30] assumes no polarization from only the valence quarks and does not match what was found from the EMC experiment x range. This indicated that there was missing spin the must be carried by other constituents. This anomaly was called the "spin crisis".

The missing spin was then theorized to be carried by the gluons, sea quarks, and orbital angular momentum of the constituents. The modified sum rule for the proton is given by the Jaffe-Manohar[45] as:

$$\langle S_z^P \rangle = \frac{1}{2}\Delta\Sigma + \Delta G + L_q + L_g \quad (1.11)$$

where $\Delta\Sigma$ is the sum of the quark and anti-quark contribution:

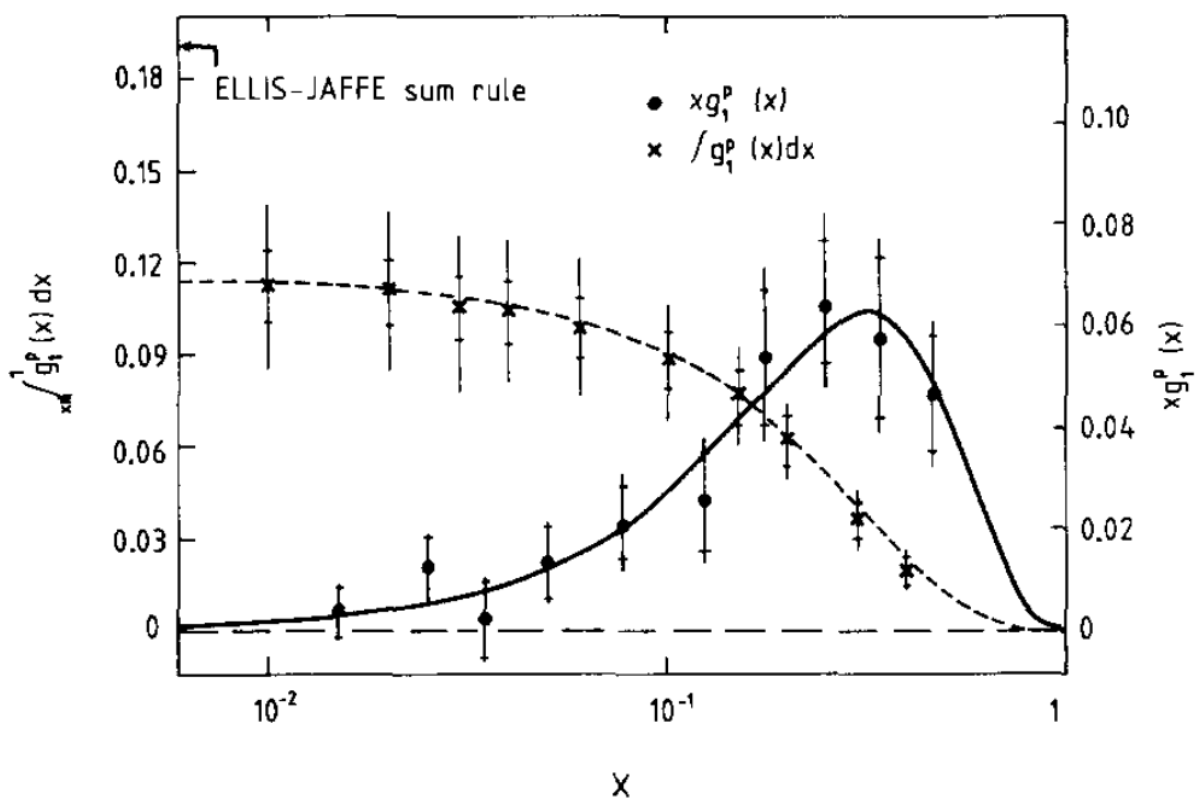


Figure 1.4: EMC result of the $g_1(x)$ integral and the Ellis-Jaffe sum rule prediction[13].

$$\Delta\Sigma = \sum_i [\Delta q_i(x, Q^2) + \Delta \bar{q}_i(x, Q^2)] \quad (1.12)$$

ΔG is the gluon contribution and $L_{q(g)}$ is the orbital angular momentum of quarks (gluons). The quark contribution $\Delta\Sigma$ to the proton spin has been well measured by DIS experiments as $\sim 30\%$ [36][31]. The spin contributions from gluons and angular momentum are not yet constrained and are essential to understanding the spin structure of the proton.

1.5 Gluon Spin Contribution

The gluon helicity distribution function $\Delta g(x)$ of the proton characterizes the inner structure of the nucleon. It's integral

$$\Delta G \equiv \int_0^1 \Delta g(x) dx \quad (1.13)$$

over all gluon momentum fraction x gives the gluon spin contribution to the proton. The longitudinal double spin asymmetry A_{LL} is measured to extract $\Delta g(x)$. The A_{LL} is written as:

$$A_{LL} = \frac{\sigma_{++} + \sigma_{--} - (\sigma_{+-} + \sigma_{-+})}{\sigma_{++} + \sigma_{--} + \sigma_{+-} + \sigma_{-+}} \quad (1.14)$$

where " + (-)" is the proton having positive (negative) helicity.⁴ It can be factorized for the process $a + b \rightarrow c + X$ as [23]:

$$A_{LL} = \frac{\sum_{abc} \Delta f_a \otimes \Delta f_b \otimes d\hat{\sigma}^{f_a f_b \rightarrow f_c X} \hat{a}_{LL}^{f_a f_b \rightarrow f_c X} \otimes D_{f_c}^h}{\sum_{abc} f_a \otimes f_b \otimes d\hat{\sigma}^{f_a f_b \rightarrow f_c X} \otimes D_{f_c}^h} \quad (1.15)$$

where $\hat{\sigma}$ and \hat{a}_{LL} are the hard partonic cross section and partonic double helicity asymmetry, which are both calculable in perturbative QCD (pQCD). The $D_{f_c}^h$ term is the probability of a parton c to fragment into a hadron h . $f_{a,b}$ is the unpolarized parton distribution

⁴Positive (negative) helicity means the spin is in the same (opposite) as the direction of momentum.

and $\Delta f_{a,b}$ is the polarized parton distribution function. In scattering involving gluons, Δf becomes Δg . Thus, the asymmetry allows access to the gluon contribution to proton spin.

Jets in pp are contributed by $2 \rightarrow 2$ hard scattering from quark-quark (qq), quark-gluon (qg), and gluon-gluon (gg) processes. At the kinematic ranges of RHIC, it is calculated that the qg and gg processes dominate[46][51]. This means that the jets measured will be sensitive to the gluon polarization. RHIC has already provided measurements on asymmetry for jets and π^0 . PHENIX and STAR are detectors in the RHIC ring which have provided asymmetry measurements for eta, pion, and jets, respectively[21][3][4]. The jet asymmetry measurement from STAR are the leading drivers in the Δg measurement. The various measured asymmetry are fit using DSSV method to extract the Δg [27]. Through fitting all the various data, the large asymmetry shown by the jets are the drivers of the gluon spin contribution, as shown in Figure 1.5[28]. The large positive Δg is driven by data from 2009 STAR jets asymmetry. Figure 1.6 shows the current uncertainty in the measurement of gluon spin contribution in different kinematic x ranges. The RHIC data set regime has smaller uncertainty and the gluon contribution as:

$$\int_{0.05}^1 \Delta g dx \sim 0.2 \quad (1.16)$$

This analysis will be the first PHENIX jet asymmetry analysis. STAR has calculated jet asymmetry from $\sqrt{s} = 510 GeV$ and $\sqrt{s} = 200 GeV$, as shown in Figure 1.7. The goal of this analysis is to provide more data points which will help improve the constraint on Δg by shrinking the uncertainty in DSSV fits, as shown in Figure 1.6

1.6 Jets

A jet is a QCD observable which is a collimated streams of hadrons from the end stage of a parton shower. There is no absolute definition of a jet since a jet is just associating the shower of an original hard parton which undergoes hadronization. Jets are the dominant final state objects in hadronic collisions, so the development of a jet reconstruction procedure

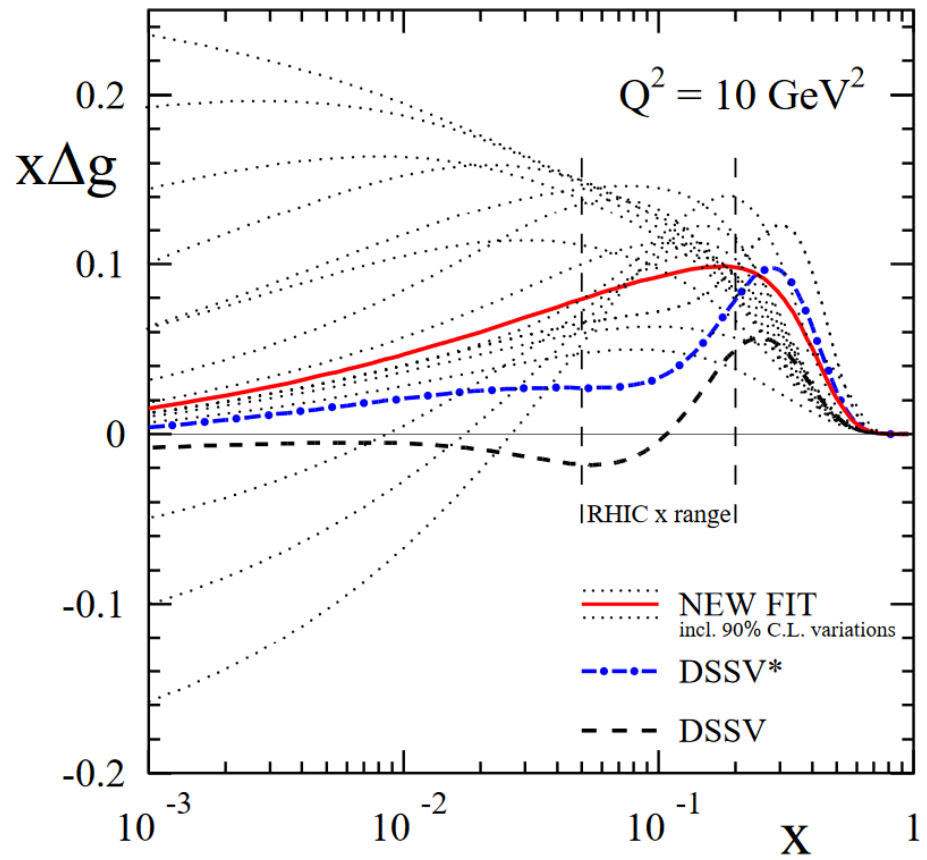


Figure 1.5: Gluon helicity distribution for $Q^2 = 10 \text{ GeV}^2$. The red line shows the DSSV analysis fit for all PHENIX and STAR data until 2009. The blue and black lines using older data (as described in [28]). The dotted lines show 90% confidence interval. The vertical dashed lines show the PHENIX x range $0.05 \leq x \leq 0.2$.

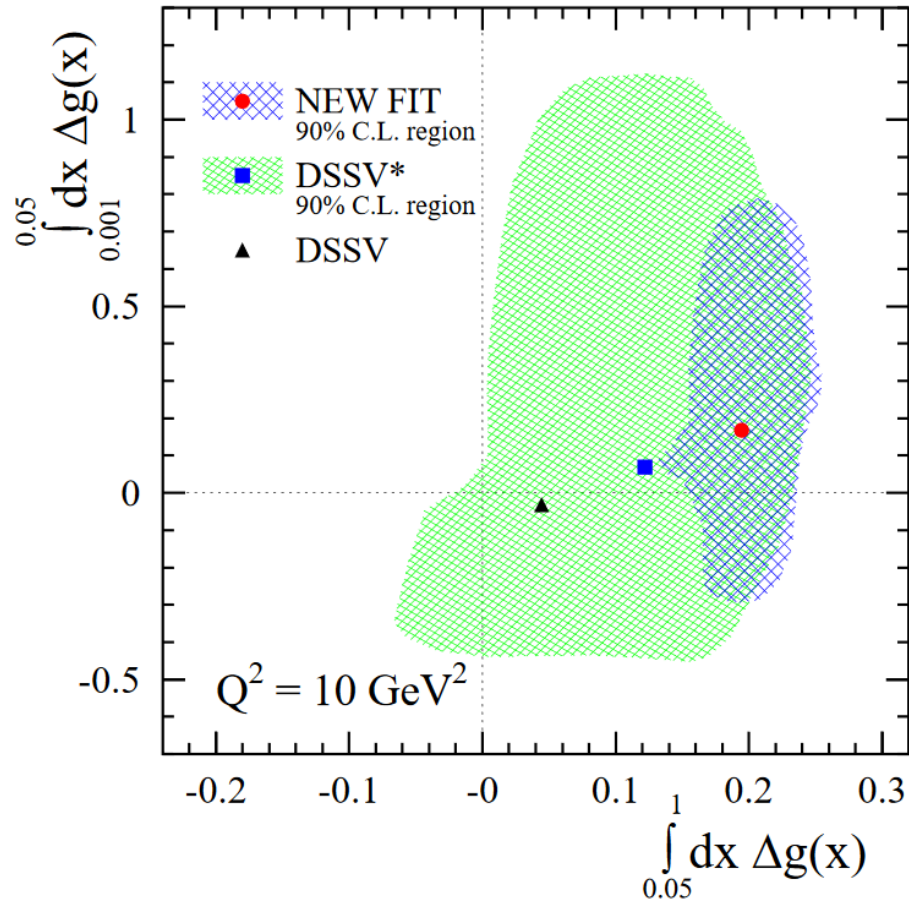


Figure 1.6: The integral of Δg over different x ranges. The different points correspond to different data sets as described by [28] and in Figure 1.5. Horizontal axis shows the range where the RHIC data sets help contribute to the calculation, and thus has smaller uncertainty.

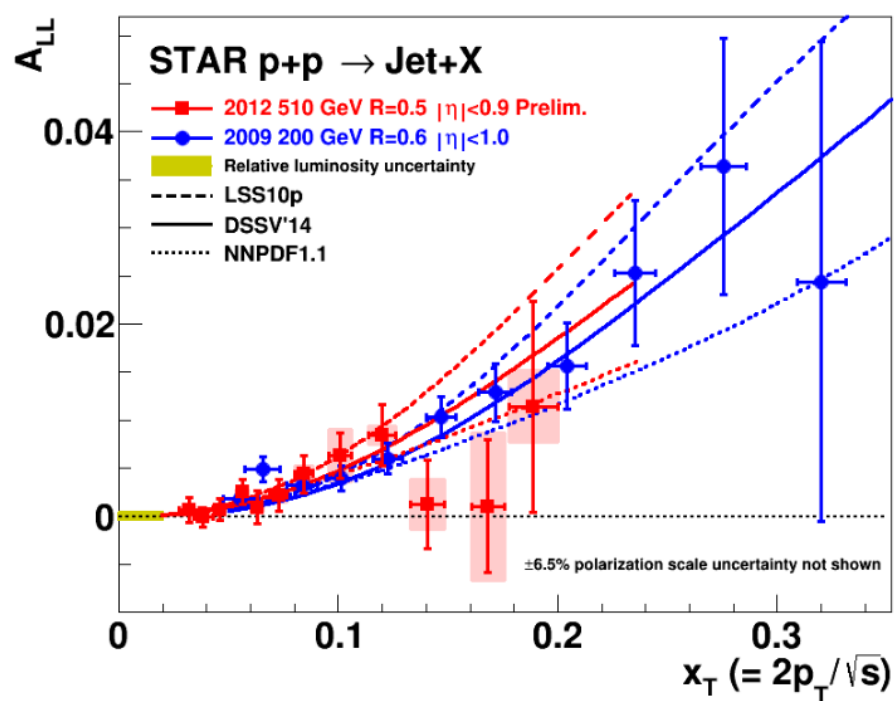


Figure 1.7: Blue points are from $\sqrt{s} = 200\text{GeV}$ and red points are $\sqrt{s} = 510\text{GeV}$ measured by STAR.

is of much importance and interest. Jet reconstruction is a procedure to combine the momenta of the fragments of the original parton, i.e. undoing the fragmentation process. There is no direct correspondence between short distance physics and final hadronization, so it is not possible to unambiguously separate the final state hadrons which come from the original parton and those from another process.

There was an effort to standardize jet definition in 1990 during the Snowmass accords[43]. There are five properties which jet definitions must meet:

1. Simple to implement in an experimental analysis;
2. Simple to implement in theoretical calculations;
3. Defined at any order of perturbation theory;
4. Yields finite cross-section at any order of perturbation theory;
5. Yields a cross-section that is relatively insensitive to hadronization.

Requiring finite cross-section at any order of perturbation theory makes the jet infrared and collinear (IRC) safe. The insensitivity to hadronization means that the jet should be insensitive to the underlying event. The jet algorithm needs to work in both experimental analyses (particle level) and theoretical calculations (parton level), so it can be difficult to satisfy all five requirements.

IRC safety means that neither soft emissions nor collinear splitting in an event should change the jet collimation which is found in that event. This is a key guiding principle in jet reconstruction algorithms. A hard parton can undergo collinear splitting through non-perturbative dynamics or during fragmentation and perturbative and non-perturbative effects can lead to emission of soft particles. An example of an IRC unsafe algorithm is detailed in Figure 1.8. In Figure 1.8(a), an event with just two hard partons are reconstructed as two separate jets. In Figure 1.8(b), an extra soft gluon has been emitted and an IRC unsafe algorithm can end up reconstructing it all as one jet. Different set of jets are reconstructed in

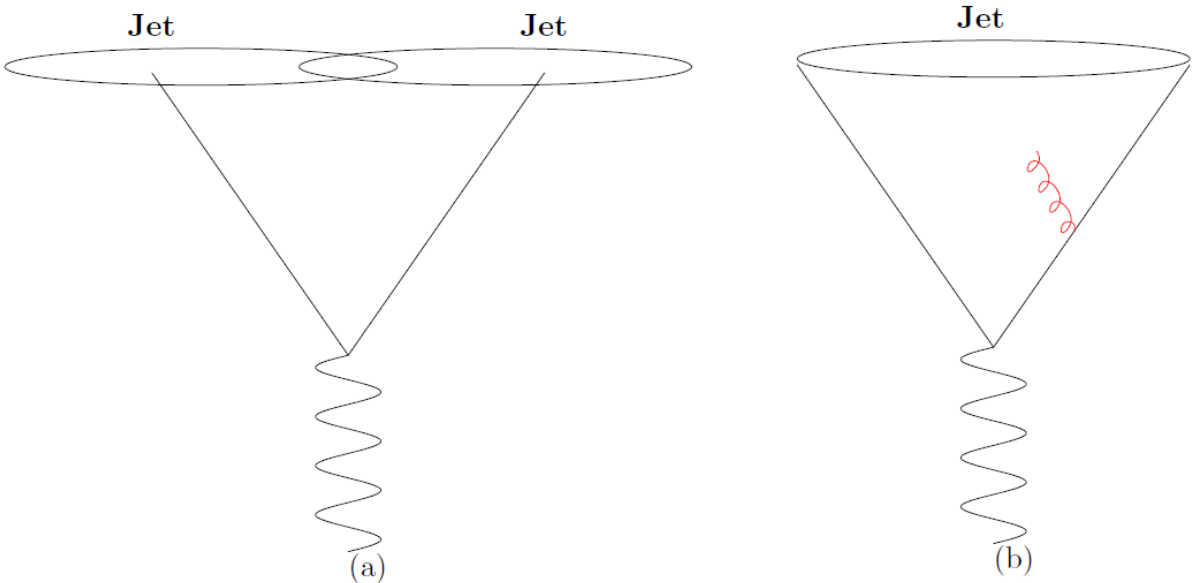


Figure 1.8: Part (a) shows an event with two hard partons reconstructed as two jets. Part (b) shows an event with one of the partons emitting a soft gluon, causing an IRC unsafe algorithm to reconstruct all the particles as one jet.

presence of soft gluon with IRC unsafe algorithms which can result in infinite cross sections in perturbative QCD calculations and thus violate point four of the Snowmass accords.

1.6.1 Jet Reconstruction Algorithms

There are many jet reconstruction algorithms and most can be divided into two categories: cone and sequential recombination algorithms[56]. Cone algorithms try to find stable regions of energy assuming that the jet structure is circular. Cone algorithms like mid-point and iterative cone algorithms were found to be infrared unsafe and thus not used[55]. Sequential recombination algorithms assume that final state particles are collinear and try to find clusters of particles which are close in momentum space. This analysis uses the Anti- k_t [24] algorithm, which is implemented using the FastJet[25] package.

1.6.1.1 Anti- k_t Algorithm

The anti- k_t algorithm is a sequential recombination algorithm which is infrared safe. It takes the four-momenta of input particles then iteratively combines them until the procedure terminates, and returns one or more jet four-momenta. The iterative process is as follows:

1. Choose an R -parameter for reconstruction At every iteration,
2. Define the anti- k_t distance d_{ij} between each pair of particles i and j :

$$d_{ij} = \min\left(\frac{1}{k_{T,i}^2}, \frac{1}{k_{T,j}^2}\right) \frac{\Delta\phi_{ij}^2 + \Delta\eta_{ij}^2}{R^2} \quad (1.17)$$

3. Distance between any particle i and the beam is defined as:

$$d_{ib} = \frac{1}{k_{T,i}^2} \quad (1.18)$$

4. Find the minimum d_{min} of all the d_{ij} and d_{ib} . Since p_T is in the denominator, the smallest d_{ij} will involve the highest p_T particle in the event.
5. If d_{min} is a d_{ij} , merge the particles i and j into a single particle and sum their four-momenta
6. Repeat processes 1-4:
 - Compute distances d_{ij} and d_{ib}
 - Find the minimum d_{min}
 - If d_{min} is a d_{ij} , then merge particles i and j into a single particle
7. When there is nothing within a distance $< R$, d_{ib} will be the smallest anti- k_t distance. The particle i is removed from the list and called a jet.

The anti- k_t algorithm is collinear and infrared safe and is easily adaptable to PHENIX, which has a limited η and ϕ acceptance. Since the algorithm begins by combining the leading particles of the jet, cases where the leading particles are near the edges of the PHENIX acceptance, the jet energy is less likely to be mis-reconstructed.

1.7 Kinematics

1.7.1 Variables

This section will describe the different variables used throughout the analysis. It follows the natural unit convention where $c = 1$ and $\hbar = 1$.

The momentum four-vector (also known as four-momentum) is defined as the energy E and three-momentum \vec{p} :

$$p^\mu = (E, p_x, p_y, p_z). \quad (1.19)$$

This is the typical four-momentum which transforms under a Lorentz transformation. The magnitude of the four-momentum is frame independent (i.e. invariant under Lorentz transformation) and is called the invariant mass m_{inv} :

$$m_{inv}^2 = p^2 = p^\mu p_\mu = E^2 - \vec{p} \cdot \vec{p} \quad (1.20)$$

In the rest frame of the particle, this converts to the famous relation $E = mc^2$. The sum of the four-momenta of two particles in a collision is a Mandelstam variable,

$$s = (p_1 + p_2)^2, \quad (1.21)$$

where p_1 and p_2 are the four-momenta of the colliding particles. The \sqrt{s} is known as the center of mass energy of the collision.

The coordinate system in this analysis is shown in Figure 1.9. The z-axis is the beam direction, ϕ is the azimuthal scattering angle, and θ is the center-of-mass scattering angle.

The transverse and longitudinal momentum component, p_T and p_L respectively, are defined as:

$$p_T = |\vec{p}| \sin(\theta), \quad (1.22)$$

$$p_L = |\vec{p}| \cos(\theta). \quad (1.23)$$

The transverse momentum p_T is invariant under Lorentz transformation in z-axis (beam direction), while p_L is not. The rapidity y is defined as:

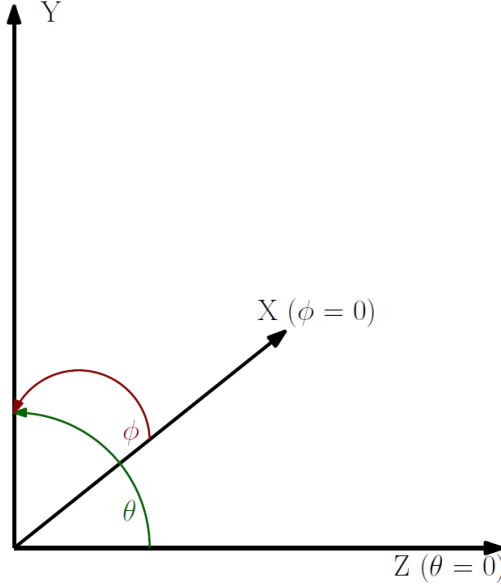


Figure 1.9: The coordinate system used in the analysis.

$$y = \frac{1}{2} \ln \left(\frac{E + p_L}{E - p_L} \right) \quad (1.24)$$

Rapidity can be difficult to measure in since the total energy and momentum are needed. An easier quantity to measure, pseudorapidity η , is used. In the regime of $E \gg m_0$, where the energy of the particle is much larger than rest mass, the pseudorapidity is:

$$\eta = \frac{1}{2} \ln \left(\frac{p + p_L}{p - p_L} \right), \quad (1.25)$$

$$\eta = -\ln \left(\tan \left(\frac{\theta}{2} \right) \right) \quad (1.26)$$

Pseudorapidity can be determined directly from the scattering angle θ making it more useful for experiments. It can also be used to define kinematic variables such as energy and longitudinal momentum as:

$$E = p_T \cosh(\eta), \quad (1.27)$$

$$p_L = p_T \sinh(\eta) \quad (1.28)$$

1.7.2 Jet Variables

Since a jet contains many constituents, it's properties are tied to them. Several jet-level variables are defined and used in this analysis to reject jets reconstructed from the combinatoric particles and remove contamination from high p_T background.

1.7.2.1 Number of Constituents

The number of constituents $n.c.$ of an anti- k_t jet is defined as:

$$n.c. = \sum_{Particles} 1 \times \Theta \left(R_{anti-k_t} - \sqrt{\Delta_{jet,particle}^2 + \phi_{jet,particle}^2} \right) \quad (1.29)$$

If the constituent is within the 'cone' defined by R , then it will be assigned a weight of 1. This analysis requires $n.c \geq 3$ in a reconstructed jet to help reject jets reconstructed from combinatory particles.

1.7.2.2 Charged Fraction of Jet p_T

The charged fraction $c.f.$ is the fraction of jet p_T carried by charged tracks. The charged fraction is defined as:

$$c.f. = \frac{1}{p_T^{jet}} \sum_i p_T^i, i = \text{charged constituents} \quad (1.30)$$

1.7.2.3 Discriminant

The discriminant is used to identify and reject fake jets on a jet-by-jet basis. It is defined as:

$$Discriminant = \sum_{Particle} p_{T,Particle}^2 \exp \left(\frac{-(\Delta\eta_{jet,particle}^2 + \phi\eta_{jet,particle}^2)}{2R_{dis}^2} \right) \quad (1.31)$$

Choosing $R_{dis} = 0.1$ will give large values of the discriminant to jets with tight core of particles. The p_T^2 weighting will give large value of the discriminant to jets with harder fragmentation kinematics.

CHAPTER 2. THE EXPERIMENT

The data analyzed in this dissertation is from polarized p+p collisions at $\sqrt{s} = 510$ GeV collected at RHIC using the PHENIX detector at Brookhaven National Laboratory (BNL) in year 2013. This chapter will describe the RHIC ring and details of the PHENIX detector.

2.1 RHIC

The Relativistic Heavy Ion Collider (RHIC) is located in Brookhaven National Laboratory (BNL) and is the only spin-polarized proton collider in operation. The RHIC accelerator is 3.8 km in circumference and composed of two separate rings of superconducting magnets shown in Figure 2.1. RHIC is capable of colliding heavy ions, such as deuterium, Cu, Au, and Al at various center of mass energies. The goals of RHIC and it's detectors are to study the Quark-Gluon Plasma (QGP) and to measure the gluon spin contribution, Δg , to the total proton spin. The detectors operating in 2013 were PHENIX and STAR, which are two places where collisions occurred (interaction points). The blue and yellow rings are capable of containing 120 bunches, but nine bunches are kept empty for the abort gap, which a time to allow for detectors to reset. The blue ring protons rotate clockwise and the yellow ring protons rotate counterclockwise. The full RHIC rings and booster rings can be seen in Figure 2.1.

2.2 Polarization

The polarized protons begin with the Optically Pumped Polarized Ion Source (OPPIS)[59][62]. An Atomic Hydrogen injector provides an ionized atomic hydrogen beam from a helium gas

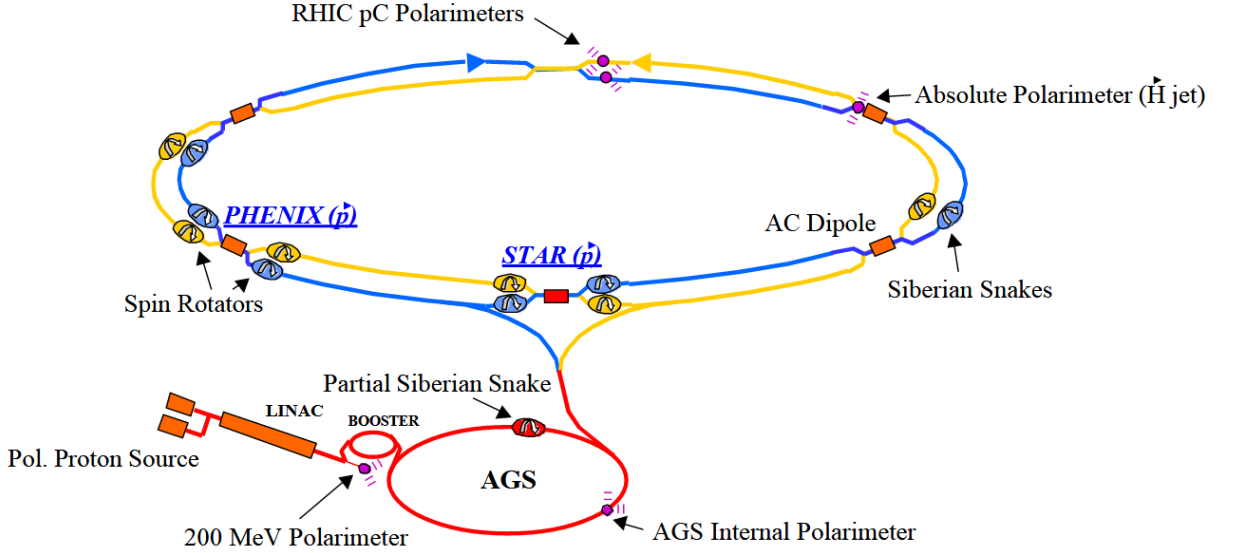


Figure 2.1: The RHIC compound and its components.

ionizer cell. These unpolarized protons (H^+) pass through excited (optically pumped) Rubidium gas in a 4 Tesla magnetic field to produce electron-spin polarized H^0 . The polarization is transferred to the nucleus through a Sona transition[48]. The polarized hydrogen is then passed through a Na-jet vapor cell to produce H^- , and thus allowing further acceleration of the beam. These are passed onto the Radio Frequency Cavity (RFQ), which accelerates the beam to 750 KeV. Then beam is injected into the LINAC, which accelerates the beam to 200 MeV and injects them into a low energy booster. The booster provides acceleration to 2.3 GeV and continues them on to the Alternating Gradient Synchrotron (AGS). The AGS further accelerates the protons to higher energy of 24.3 GeV and the beam is then finally transferred to the RHIC ring. The RHIC ring accelerates the protons to their final center of mass energies. The acceleration process can be seen in Figure 2.1. Once in the ring, the protons need to keep their polarization to provide the polarized collisions and a special device is needed to keep their polarization.

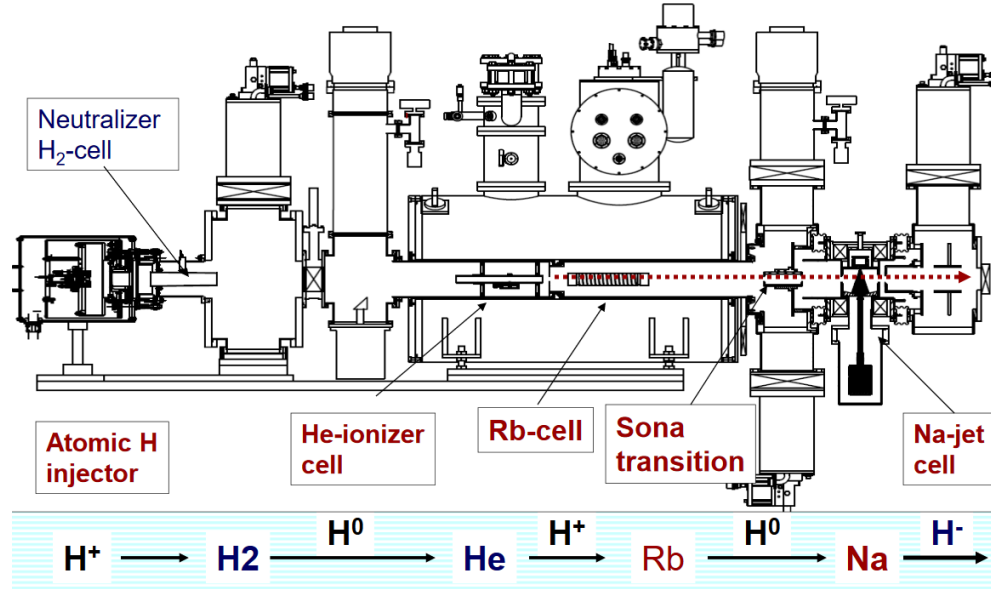


Figure 2.2: Procedure to produce the polarized Hydrogen beam[61].

2.2.1 Siberian Snakes

A proton beam loses polarization as it is accelerated along the RHIC ring due to the spin interaction with the magnetic and electric fields which accelerate the polarized protons. Oscillating electric fields are used to accelerate the particles and to keep them horizontally bunched. The spin vector in the presence of a magnetic field is given by the Thomas-BMT equation[17, 26].

$$\frac{d\vec{S}}{dt} = \frac{-e}{\gamma m} [(1 + G\gamma)\vec{B}_\perp + (1 + G)\vec{B}_\parallel] \times \vec{S} \quad (2.1)$$

The $\vec{B}_{\perp(\parallel)}$ are the perpendicular (parallel) component of the magnetic field and $G = 1.7928$ is the anomalous g-factor for the proton. γ is the Lorentz factor, m is mass, and e is the charge. The factor $G\gamma$ is called the spin tune and gives the precession frequency in one orbital revolution. The spin depolarization occurs when there is a coherent build-up of perturbations to spin vector from the magnetic fields of the acceleration magnets. The two main ways this occurs is from imperfection resonances and intrinsic resonances.

Imperfection resonances occur due to magnet errors and misalignment and are characterized by $G\gamma = k$, where k is an integer. Intrinsic resonances are due to the intrinsic

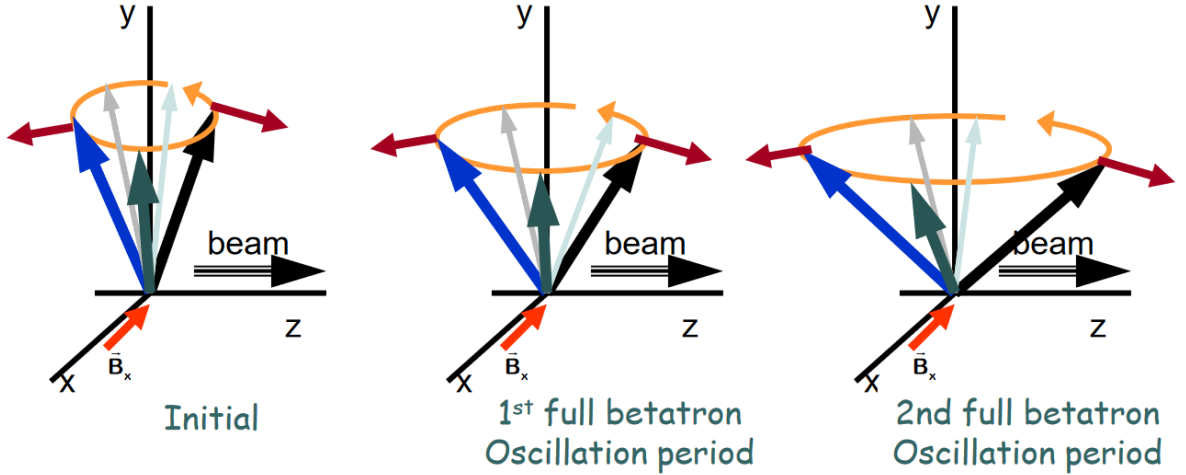


Figure 2.3: The spin vector should precess in the y -direction, but will gradually increase in radius with successive orbits without the Siberian snakes.

betatron oscillation and characterized by $G\gamma = kP \pm Q_y$, where k is an integer, P is the superperiodicity and Q_y is the vertical betatron tune. Both resonances increase in strength with higher energy[16].

The Siberian Snakes[29] flip the spin vector by 180° during each circular orbit to prevent the coherent build-up of the spin perturbations. Figure 2.3 illustrates this process. The Siberian Snakes are groups of dipole magnets which rotate the spin vector and a 'snakelike' pattern, as seen in Figure 2.4[58]. There are two Siberian Snakes in RHIC, as seen in Figure 2.1, for each ring. The spin perturbations due to the resonances should cancel out in two revolutions and thus ensuring a polarized beam. The beam polarization needs to be measured periodically and will be detailed in the next section.

2.2.2 Polarimetry

RHIC has two polarimeters to measure the polarization of the beams. These are the proton-Carbon (pC) and the hydrogen jet (\vec{H}) polarimeter.

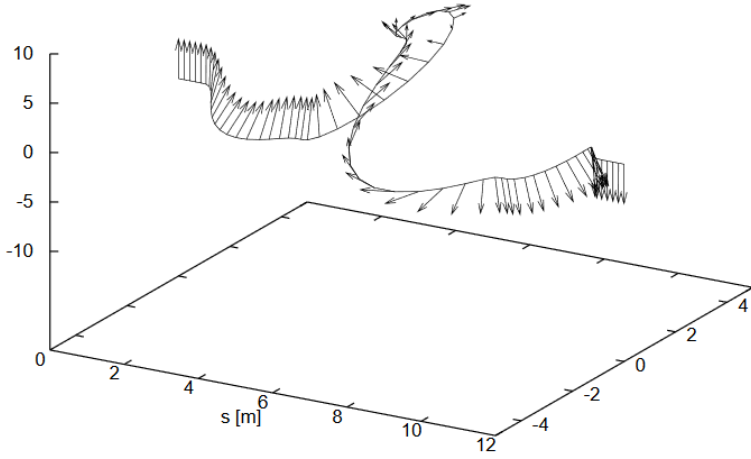


Figure 2.4: The orbit and spin vector of the particle as it passes through the Siberian Snake. The spin vector is rotated 180° .

2.2.2.1 pC Polarimeters

The pC polarimeters in RHIC are based on proton scattering from Carbon and measuring the left-right asymmetry in recoil Carbon nuclei[18, 42, 41]. There is a thin ribbon of Carbon inserted into the beamline and the asymmetry is measured using six Silicon strip detectors, seen in Figure 2.5. This is measured at the beginning of the fill, during, and before the end of a fill.¹ This pC polarimeter gives the change in the polarization, but not the absolute polarization. That is done by the hydrogen jet polarimeter.

2.2.2.2 Hydrogen jet Polarimeters

The \vec{H} polarimeter is similar to the pC, but a jet of polarized hydrogen is used instead[63]. A beam of polarized ionized hydrogen gas is injected into the beam region and the scatter is measured using Silicon strip detectors. The target (hydrogen jet) polarization is measured by a Breit-Rabi polarimeter. The asymmetry of both the beam and the Hydrogen jet must be the same (elastic scatter), giving equation 2.2.

¹A 'fill' is (usually) 8 hour long collisions.

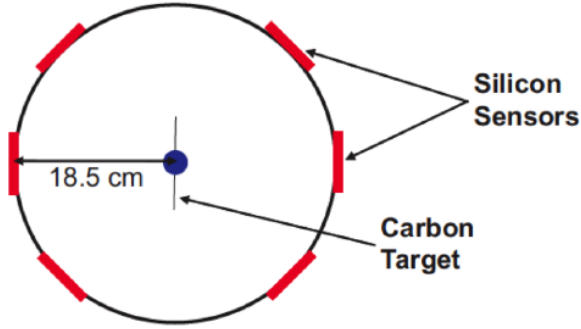


Figure 2.5: The beamline view of the pC polarimeter with the Carbon target in the center. The recoil Carbon atoms are measured by the six Silicon detectors.

$$A_N = \frac{\epsilon_{N,target}(measured)}{P_{target}(known)} = \frac{\epsilon_{N,beam}(measured)}{P_{beam}(unknown)} \quad (2.2)$$

From this measurement, the polarization of the beam can be calculated. This is a low rate process due to the dilute target and done once per fill, so many fills are required to provide lower uncertainties in measurement. The \vec{H} measurement is used to normalize the pC polarimeter.

2.2.2.3 PHENIX Local Polarimeter

The polarization of the beam is monitored by each experiment as well. In PHENIX, there are two Zero Degree Calorimeters (ZDC)[8] which are used to check the polarization. The ZDCs are hadronic calorimeters located past the PHENIX bending magnets. This means the ZDC will sample neutral particles, i.e. neutrons and photons. The asymmetry measured by the ZDC is then used to check the local polarization at PHENIX[47]. A schematic of the ZDC can be seen in Figure 2.6.

2.2.2.4 Spin Rotators

The stable polarization in the RHIC ring is vertical (up towards the sky or down towards the ground), so the polarization needs to be rotated to a horizontal orientation for the A_{LL}

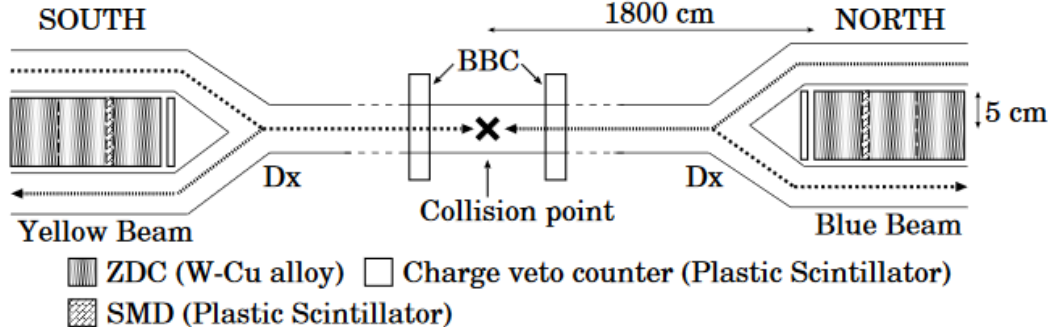


Figure 2.6: Experimental setup of ZDC at PHENIX (not to scale)[5].

measurement. The spin rotators are located before and after the interaction point, seen in Figure 2.1. Each rotator consists of four superconducting helical dipole magnets, similar to the Siberian Snake, but they rotate the spin to align in the same or opposite direction as the velocity of the beam[50]. After the interaction region, the rotators flip the spin polarization back into the stable vertical direction.

2.2.2.5 Spin Pattern

Each beam can have a positive or negative helicity, i.e. spin orientation with respect to the velocity. The total polarization from each collision will be: $(++, +-, -+, --)$, where the $+$ or $-$ are the polarization of each beam. An illustrated example is shown in Figure 2.7. The spin pattern is the arrangement of the spin orientation of the proton bunch. There are several spin patterns used to ensure no systematic bias from one pattern. The different patterns for Run 13 (data set for this analysis) is shown in 2.8.

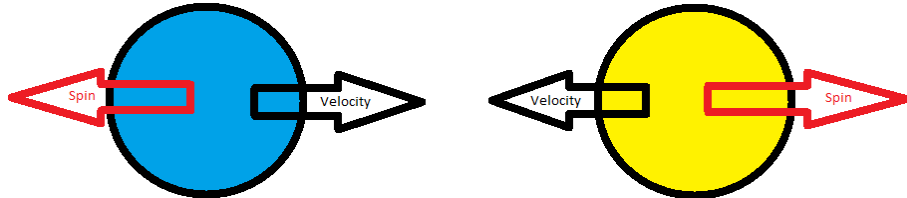


Figure 2.7: This shows an example of the blue and yellow beams having spin vectors in the opposite direction of velocity, hence a $(--)$ configuration.

Spin Pattern	Beam	Patterns Helicity
P21	BLUE	+ + - - + + - - + +
	YELLOW	- - + + + + - - -
P22	BLUE	+ + - - + + - - + +
	YELLOW	+ + - - - + + + +
P23	BLUE	- - + + - - + + - -
	YELLOW	- - + + + + - - -
P24	BLUE	- - + + - - + + - -
	YELLOW	+ + - - - + + + +
P25	BLUE	- - + + + + - - -
	YELLOW	+ + - - + + - - + +
P26	BLUE	- - + + + + - - -
	YELLOW	- - + + - - + + - -
P27	BLUE	+ + - - - + + + +
	YELLOW	+ + - - + + - - + +
P28	BLUE	+ + - - - + + + +
	YELLOW	- - + + - - + + - -

Figure 2.8: This table shows the different spin patterns in Run 13 data set.

2.3 PHENIX

The PHENIX² detector is composed of many different sub-detectors which combine to form the overall detector[7]. As seen in Figure 2.9, it is composed of two central arms and detectors in the forward and backward region. This analysis will use the central arm detectors (Drift Chamber, Pad Chambers, Electromagnetic Calorimeters) and the Beam Beam Counters, which will be detailed in the following sections.

2.3.1 BBC

The Beam Beam Counters (BBC) are located on both sides of nominal collision point at ± 144 cm in the z-direction (along beam line) and cover $3.1 < |\eta| < 3.9$ in pseudorapidity and 2π azimuthal[11]. Each BBC has 64 elements composed of one inch meshed dynode photomultiplier tube (PMT) mounted on three inch quartz Cherenkov radiator, seen in

²Pioneering High Energy Nuclear Interaction eXperiment

Figure 2.10.

The BBC are key in determining whether or not a collision occurred, determining the z-vertex of the collision, and also the initial time of the collision. The two BBCs are used for each event to determine those quantities, as shown by Figure 2.11 and equations 2.32.4.

$$Z_{Vertex} = \frac{T_S - T_N}{2} \times c \quad (2.3)$$

$$T_0 = \frac{T_S + T_N - 2L/c}{2} \quad (2.4)$$

Where $T_{S(N)}$ are the average hit time, c is velocity of light, and $L = 144$ cm (distance from nominal center to BBC).

2.3.2 Drift Chamber

The Drift Chamber (DC) is used to track charged particles in the PHENIX central arms[6]. The face is located 2 m above the beam line and therefore in a region of minimal magnetic field, so the particles move without bending through the DC. The DC acceptance range is ± 0.35 in η (pseudorapidity), ± 1.25 m in Z (beam axis), and 90° in ϕ (azimuthal). The DC is a wire chamber with 20 keystones, each of which contain modules with 6 radial layers of wires: X1, U1, V1, X2, U2, V2. Figure 2.12 shows the keystone and the wire setup. The wires are suspended in a gas mixture of 50% Argon and 50% Ethane (C_2H_6) to provide uniform drift velocity, high gain, and are low diffusion gasses to reduce outgassing. The U and V wires are placed at 6° with respect to the X wires and provide a Z-coordinate of the charged particle. Each wire provides an $r - \phi$ resolution of $165 \mu\text{m}$ and 2 mm spatial resolution in z -axis (along beamline).

2.3.3 Pad Chambers

The PHENIX Pad Chambers (labelled PC1, PC2, and PC3 in Figure 2.9) are multi-wire proportional chambers which can determine the Z-axis (beam line) location of charged tracks with fine resolution[32]. The PCs are composed of two cathode planes and a wire

anode plane. One of the cathode layers is composed of finely segmented pads which contain 3 pixels each, seen in Figure 2.13. The PCs require all 3 pixel signals for a valid hit, and the PCs yield a z-position resolution of ± 1.7 mm. Only the PC1 and PC3 are used in this analysis.

2.3.4 Electromagnetic Calorimeter

The PHENIX Electromagnetic Calorimeter (EMCal) is used to reconstruct electromagnetic showers[12]. There are two types of EMCal: Lead Scintillator (PbSc) and Lead Glass (PbGl), seen on Figure 2.9. The EMCal is covers acceptance of ± 0.35 in η , ± 1.25 m in Z (beam axis), and 90° in ϕ (azimuthal), same as the DC. The EMCal has eight sectors, 6 PbSc and 2 PbGl, located on each central arm just behind the PC3, and measures the energy, position, and time of flight. There are a total of 24,768 detector readout channels, which give the fine spatial resolution of the clusters. The general principle of the EMCal is to produce Bremsstrahlung ($e^- \rightarrow e^-\gamma$) and pair-production ($\gamma \rightarrow e^+e^-$) to generate an electromagnetic shower (scintillation), which is then amplified by a semiconductor Avalanche Photo-Diode (APD) or Photo-Multiplier Tube (PMT), and read out by electronics. The two types of EMCal are described in the next sections.

2.3.4.1 PbSc

The PbSc is a sampling calorimeter made of layers of Lead and scintillator with 15,552 towers. The Lead generates the electromagnetic shower and the scintillator produces the light that will be collected by the PMT. Figure 2.14 shows the process and the layout of a module, which is just 4 towers combined. Each tower is still read out individually and is 18 radiation lengths long with a nominal energy resolution of

$$\frac{\sigma_E^{PbSc}}{E} = \frac{8\%}{\sqrt{E(GeV)}} \oplus 2.1\%. \quad (2.5)$$

2.3.4.2 PbGl

The PbGl is a homogeneous calorimeter using only PbGl as a Cherenkov radiator. It is located on the lower half of the east arm EMCal (seen as PbGl in Figure 2.9). The particle entering the PbGl generates Cherenkov³ radiated photons which are collected by the PMT. There are 9,216 of such towers, which are grouped into 24 to form a super module, shown in Figure 2.15. Each PbGl tower face is $4 \times 4 \text{ cm}^2$ and 40 cm long with radiation length of 14.4 and a nominal energy resolution of

$$\frac{\sigma_E^{PbGl}}{E} = \frac{5.9\%}{\sqrt{E(\text{GeV})}} \oplus 0.8\%. \quad (2.6)$$

2.4 Ring-Imaging Cherenkov Detector

The Ring-Imaging Cherenkov (RICH)[10] detector is the primary identifier of electrons and is located in the central arms. The RICH contains 48 composite mirror panels which form two spherical surfaces with total reflecting area of 20 m^2 . The spherical mirrors focus the Cherenkov light into two arrays of 1280 PMTs located on both sides of the RICH entrance window. The entrance window of the RICH has an area of 8.9 m^2 , an exit window area of 21.6 m^2 , and a volume of 40 m^3 . A diagram is shown in Figure 2.16.

The RICH is filled with carbon dioxide (CO_2) gas at 1 atm, which is the most suitable radiator gas. CO_2 gas has a Cherenkov threshold of 18 MeV/c for electrons and 4.65 GeV/c for pions, and produces 12 photons per ring for $\beta = 1$ particle for a path length of 1.2 m. Searching for PMTs within the nominal radius of a charged track distinguishes the electron from hadrons below $\approx 4.65 \text{ GeV}/c$.

2.5 Data Acquisition and Triggers

The PHENIX Data Acquisition (DAQ) system can collect data at an event rate of $\sim 6 - 7 \text{ kHz}$ at optimal running. Figure 2.17 shows the different steps of the data collection. The

³Cherenkov radiation occurs when a particle is moving faster than the speed of light in a medium

data collection begins with a Granular Timing Module (GTM) sending a trigger signal to the Front End Module (FEM) of each detector in the interaction region. The FEM digitizes and sends the detector's signals via a fiber optic cable to Data Collection Module (DCM), located outside of the interaction region (and hence accessible during/between runs). The DCM packages the data accordingly and sends it to the Sub Event Buffers (SEBs), which then pass the data to the Assembly and Trigger Processors (ATPs). The ATPs assemble the event fragments from different subsystems into a full event containing the data from each detector and pass this full data into a buffer box for archiving.

The BBC firing rates are typically in the MHz range and so must be scaled down since the DAQ can only record up to ~ 7 kHz. The Local Level 1 (LL1) triggers from the Global Level 1 (GL1) by a scaledown factor. A scaledown factor of 1 means that every other event will be recorded, hence one event is skipped. This factor is changed accordingly to allow to let the DAQ record events at the maximum rate. The two triggers of interest in this analysis are the Minimum Bias and the EMCAL/RICH trigger (ERT).

2.5.1 Minimum Bias Trigger

The BBC detectors are main detectors used to determine if an event occurred. If at least one tube is fired in both the north and south BBCs, then the collision vertex can be determined. There are three types of Minimum Bias triggers used by PHENIX:

- A trigger which accepts events which have $z_{vertex} = \pm 30$ cm from the nominal collision point.
- A narrow vertex trigger which accepts events which have $z_{vertex} = \pm 10$ cm from the nominal collision point.
- A no vertex cut trigger which accepts any coincidence between the BBCs.

2.5.2 EMCAL/RICH Trigger

The EMCAL/RICH trigger (ERT) selects events with high- p_T electromagnetic probes or the presence of heavy flavor decays. The ERT trigger measures the energy in 2x2 tiles of the calorimeter towers and in sliding 4x4 windows of four adjacent 2x2 tiles. Figure 2.18 shows a diagram of the procedure for ERT trigger signal.

An ASIC chip sums the 2x2 tower energies and one FEM reads out 6x6 ASIC chips (12x12 towers). There are 36 sums of 2x2 and 4x4 tower energy per FEM. The 4x4 sum is used to eliminate inefficiency of a particle hitting the border of a 2x2 tower block. The energy sum of each 4x4 and 2x2 is compared to certain energy thresholds to form a trigger. The 4x4 triggers in increasing energy threshold are: ERT_4x4c, ERT_4x4a, ERT_4x4b. The ERT_2x2 only uses the energy of the 2x2 tower sum, while the ERT_Electron trigger uses the 2x2 tower sum and also the minimum number of photoelectron in the RICH.

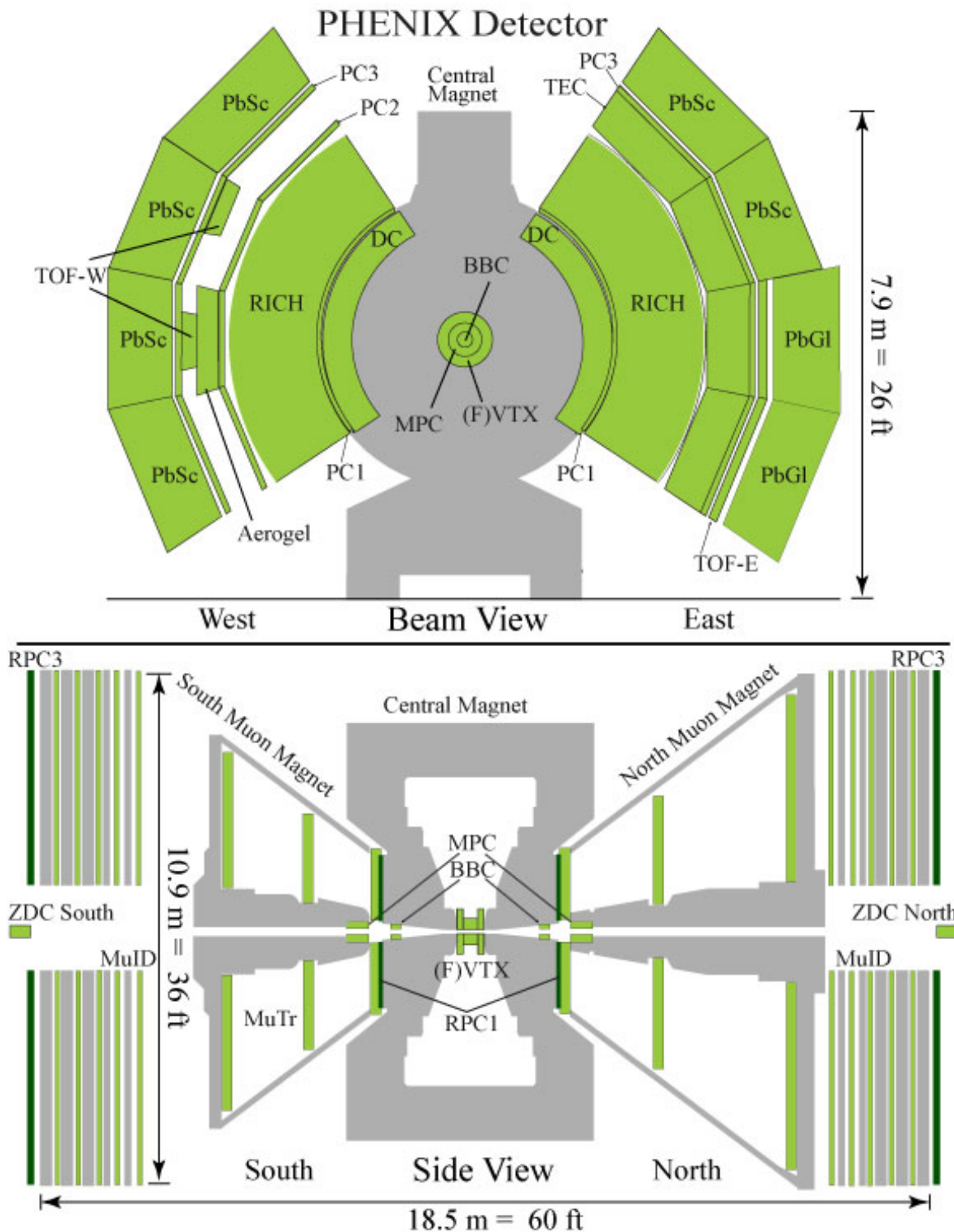


Figure 2.9: Top is the view along the beamline and bottom is perpendicular to the beamline.

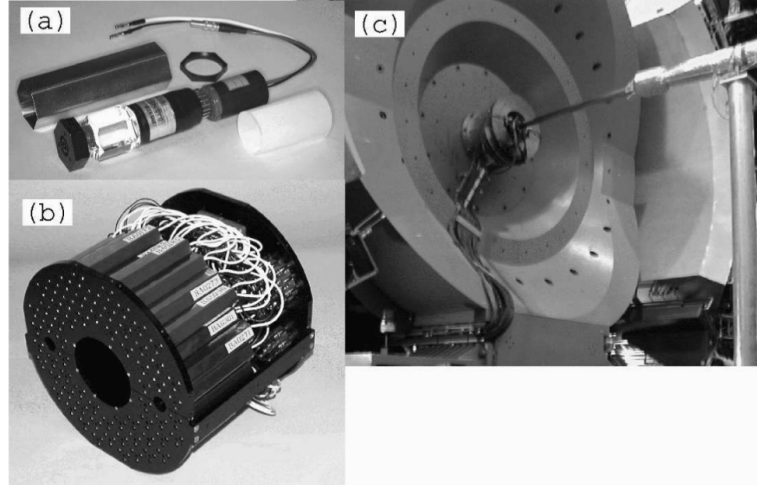


Figure 2.10: (a) Single BBC element. (b) Array of 64 elements. (c) BBC mounted in PHENIX, encircling the beam pipe[11].

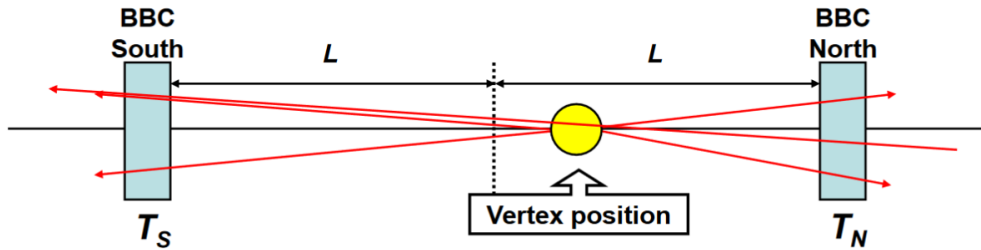


Figure 2.11: Cartoon for a collision seen by BBC[52].

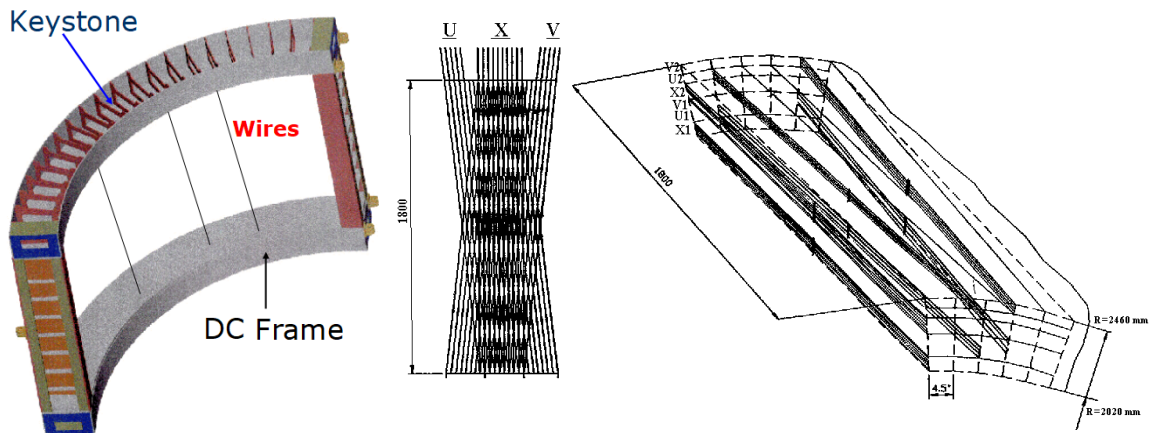


Figure 2.12: Left: The DC frame and keystones with wire direction. Middle: X, U, V wire orientations. Right: The different wire layers on keystones[6].

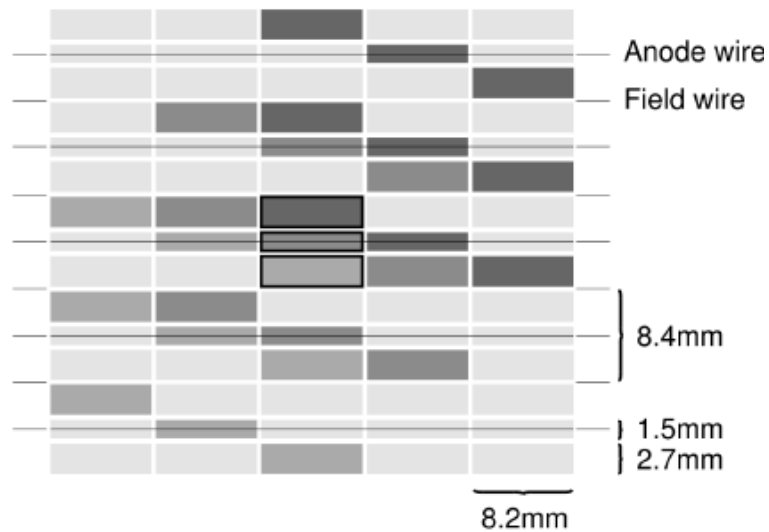


Figure 2.13: Cross section of a pad chamber. The anode wires are in front of the pad detectors[6].

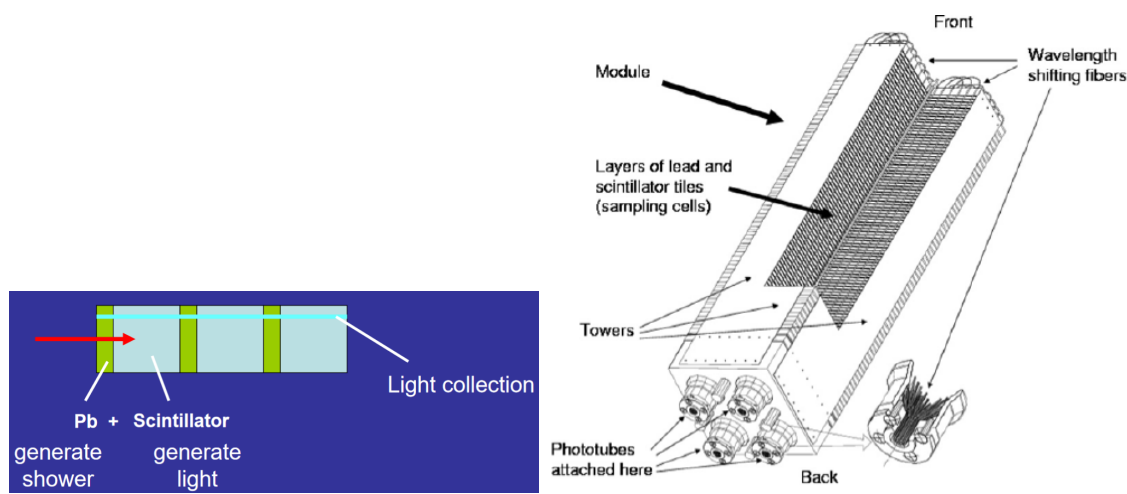


Figure 2.14: Left: Process of PbSc as a photon or electron enters detector. Right: A PbSc module consisting of 4 towers[12].

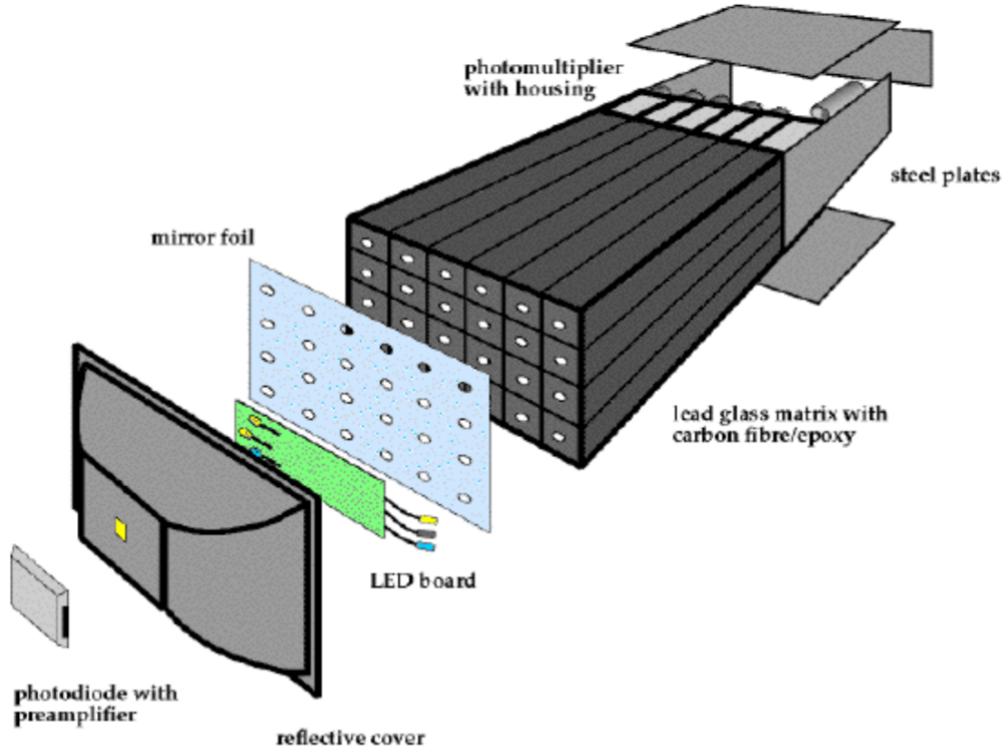


Figure 2.15: Overview of a PbGl supermodule[12].

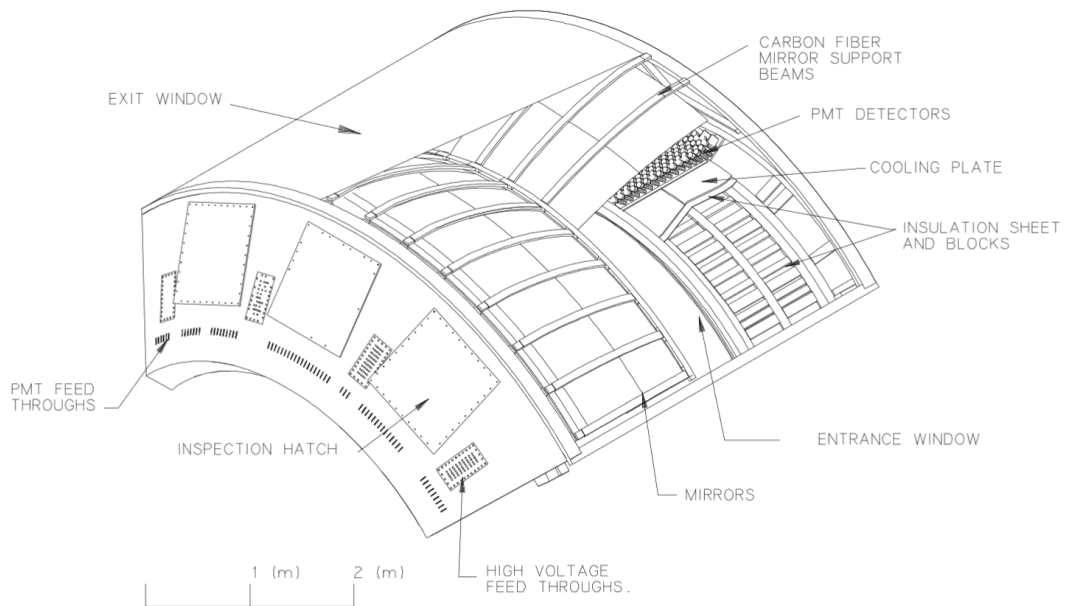


Figure 2.16: Cutaway view of an arm of the PHENIX RICH detector[10].

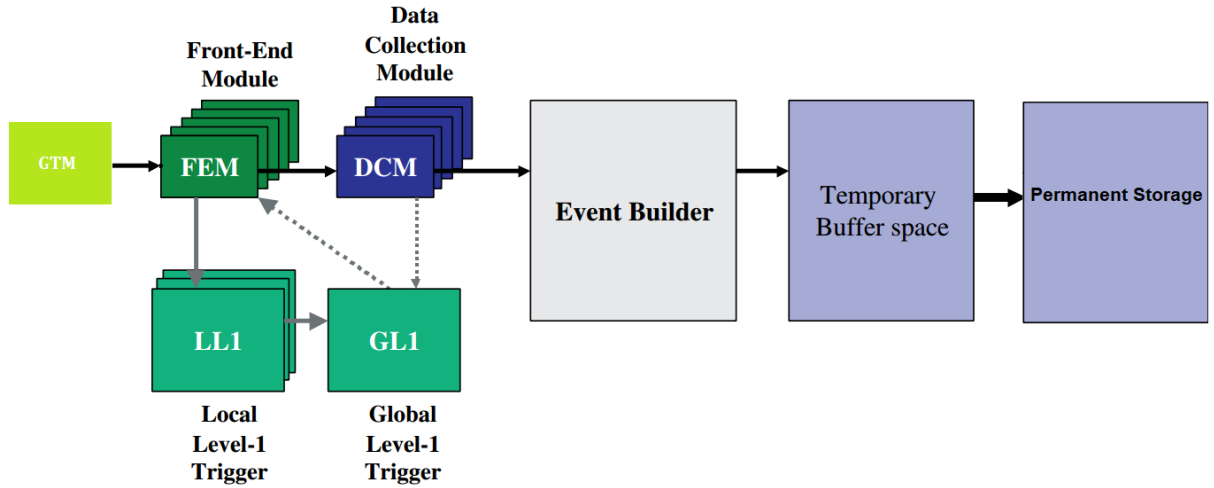


Figure 2.17: Schematic of the data collection flow in PHENIX.

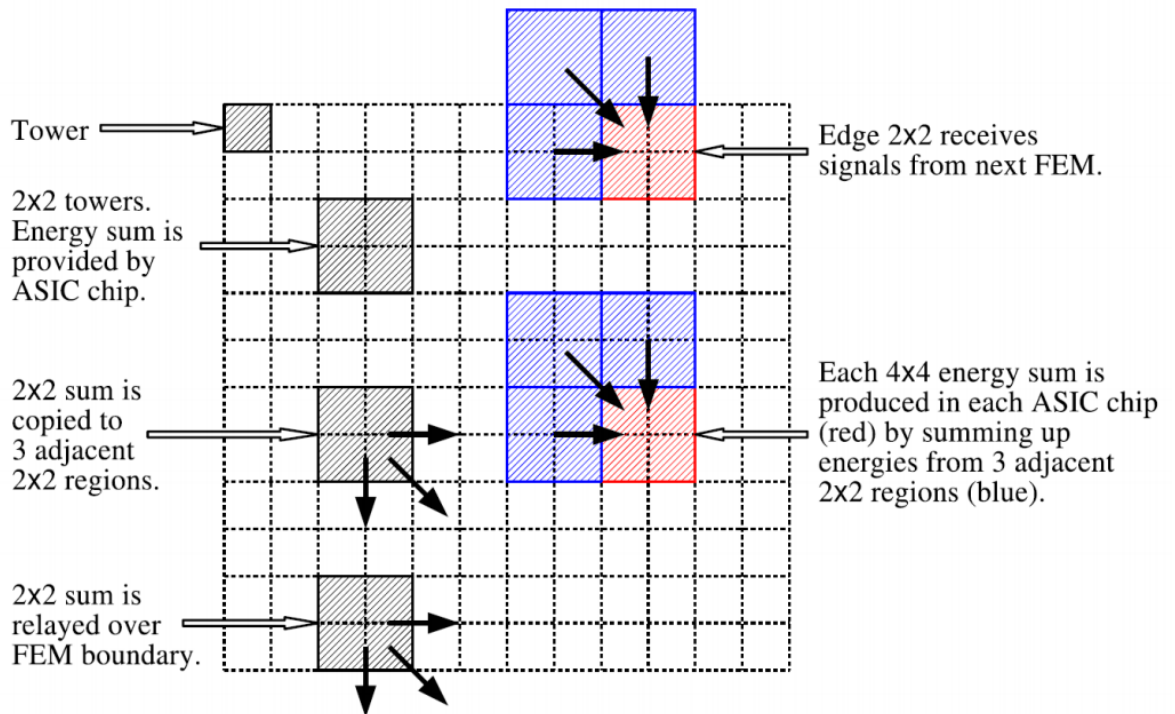


Figure 2.18: Diagram of the procedure for the ERT trigger[60].

CHAPTER 3. DATA ANALYSIS

The $p+p$ data analyzed was taken with the PHENIX detector at RHIC between February 17, 2013 to June 10, 2013 (called Run 13 data). The triggers used in this analysis are:

- Minimum Bias: BBCLL1(> 0 tubes) narrowvtx
- ERT: ERT_4x4b

The Minimum Bias (MB) will be used for the trigger efficiency study and to calculate the effective number of events for the ERT dataset. The ERT has multiple bits (a, b, and c) for the signal threshold and 4x4b is the largest threshold. The ERT trigger is used for the jet finding and cross section calculation. This is will be further discussed in the following chapters.

3.1 Run Quality Assurance

Each data taking run must pass a few cuts to be considered a good run. Having a list of good runs is important to ensure that data analyzed from each run is consistent and that there are no errors in the data from the data-taking conditions. The injected polarized $p + p$ beam fill (or store) usually lasts for about 8 hours. The PHENIX Data Acquisition (DAQ) can take data runs of a maximum length of 1.5 hours. There are hundreds of data taking runs taken at PHENIX during the collision period and runs with bad conditions are not used. This ensures that the data which is analyzed has proper detector conditions regardless of when it was taken during the entire months long data taking period. There

was already a $\pi^0 A_{LL}$ analysis done on Run 13 data set, and so the good run list from that analysis was used. The criteria for a good run are described in the following sections.

3.1.1 DAQ Condition

The DAQ data taking can be stopped early due to a number of problems, and so a minimum run time of 10 minutes is required. This ensures there was adequate data taking condition for large amount of time. The live-time of the BBCLL1, ERT_4x4a, ERT_4x4b, ERT_4x4c larger than 50% were required. This ensures that there was not any issue with the triggers that are used in the analysis.

3.1.2 Spin Database and Polarization

The PHENIX spin database contains the spin pattern and polarization information for each run. If there the run did not have a clear crossing shift, strange spin pattern, or problem with scalar values, then it is discarded for use.

A minimum beam polarization of 10% was required for good runs. The typical beam polarization is 55%.

3.2 Event Selection

When analyzing each good run, cuts on each event are made to select the good events. The first is the trigger requirement that the ERT_4x4b fired, which means that an EMCal cluster was found. The trigger selects clusters above a minimum threshold energy. For the minimum bias data set, the BBCLL1(> 0 tubes) narrowvtx trigger is used. Then a z-vertex cut of $\pm 30\text{cm}$ is used to ensure the event is occurring from the collision point.

3.3 Track Selection

3.3.1 Modified Quality Cut

The Drift Chamber (DC) dead areas can be caused by faulty DC wires which are used to track charged particles. A modified quality selection for tracks in DC is done to yield a more uniform acceptance. Pad Chamber 1 (PC1) hits and DC wire X1, X2, and UV are used for a standard PHENIX track reconstruction, using the bits shown in Table 3.1.

Table 3.1: Bits used by each DC wire and PC1 hit.

X1 used: 1	UV Found: 4	PC1 Found: 16
X2 used: 2	UV Unique: 8	PC1 Unique: 32

The best case track reconstruction is quality = 63, which is when there is a X1 used bit, X2 used bit, UV unique bit, and a PC1 unique bit. The second best is quality = 31 when the PC1 is found, but ambiguous[37]. For most analyses, the quality cut of (63||31) is enough to for the DC track. For this analysis a 'modified quality' was needed because a uniform acceptance is crucial for jets. The modified quality works by loosening the quality requirement in the areas of broken wires, then creating a quality mask for each DC sector. The quality mask is created by plotting 'alpha¹ vs board', which gives the hit map in terms of the DC geometry. The board² is defined for each arm as:

$$Board_{EastArm} = \frac{3.72402 - \phi_{DC} + 0.008047 \times \cos(\phi_{DC} + 0.87851)}{0.01963496} \quad (3.1)$$

$$Board_{WestArm} = \frac{0.573231 - \phi_{DC} - 0.0046 \times \cos(\phi_{DC} + 0.05721)}{0.01963496} \quad (3.2)$$

A plot of alpha vs board is shown for tracks with the X2 used bit used in Figure 3.1, which shows the broken or inefficient areas of the X2 bit. The regions are recorded for each wire, X1, X2, and UV, and then are used to create the modified quality cut. Figure 3.2 shows the bad regions that were cut out of the X2 bit used plot.

¹Alpha (α) is proportional to $\frac{1}{p_T}$.

²Board is used since it related to hardware, rather than the azimuthal angle ϕ .

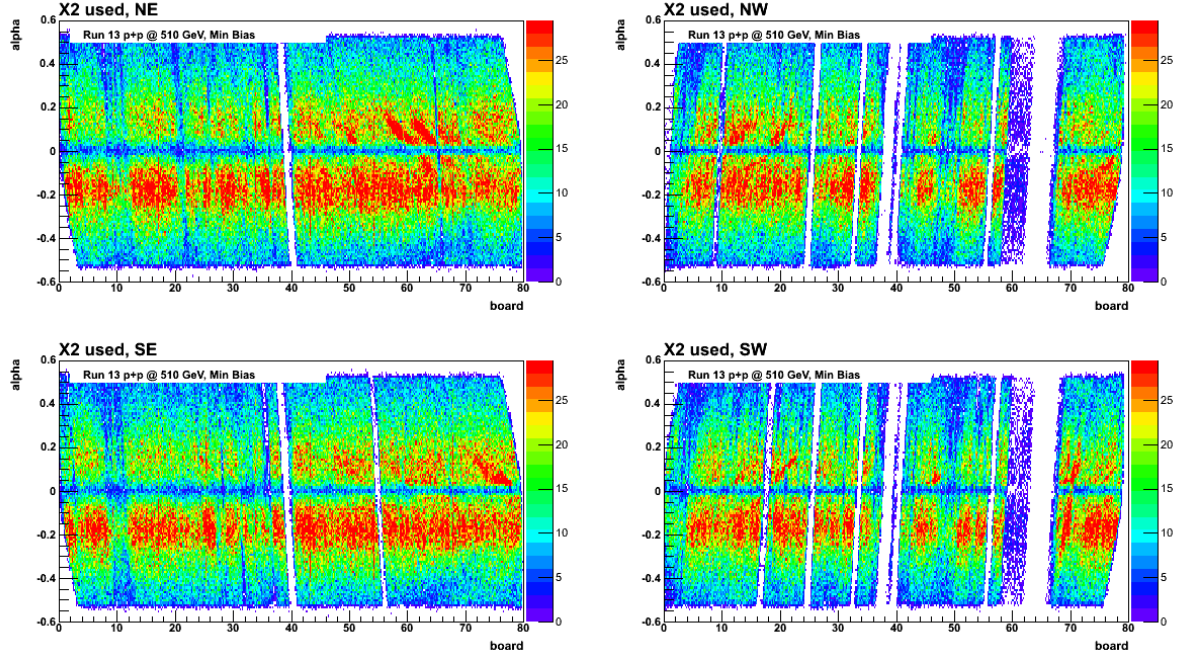


Figure 3.1: Shows the α vs. board for the X2 bit used. East (E) or west (W) is the arm, north (N) or south (S) is positive or negative z along beam axis.

Using the recorded bad areas, the modified quality cut is then developed. The track is rejected if it does not satisfy any of the following conditions:

- no (X1 used bit) and no (X2 used bit),
- no (X1 used bit) and not (in region of bad X1 acceptance),
- no (X2 used bit) and not (in region of bad X2 acceptance),
- no (UV unique bit) and not (in region of bad UV acceptance),
- no (PC1 found bit), i.e. $((\text{quality} \& 16) == 0)$,
- no (PC1 unique bit) and no (UV unique bit)

The stark difference in acceptance can be seen from Figure 3.3 and Figure 3.4. The modified quality gives a much more uniform acceptance that is desired for this analysis.

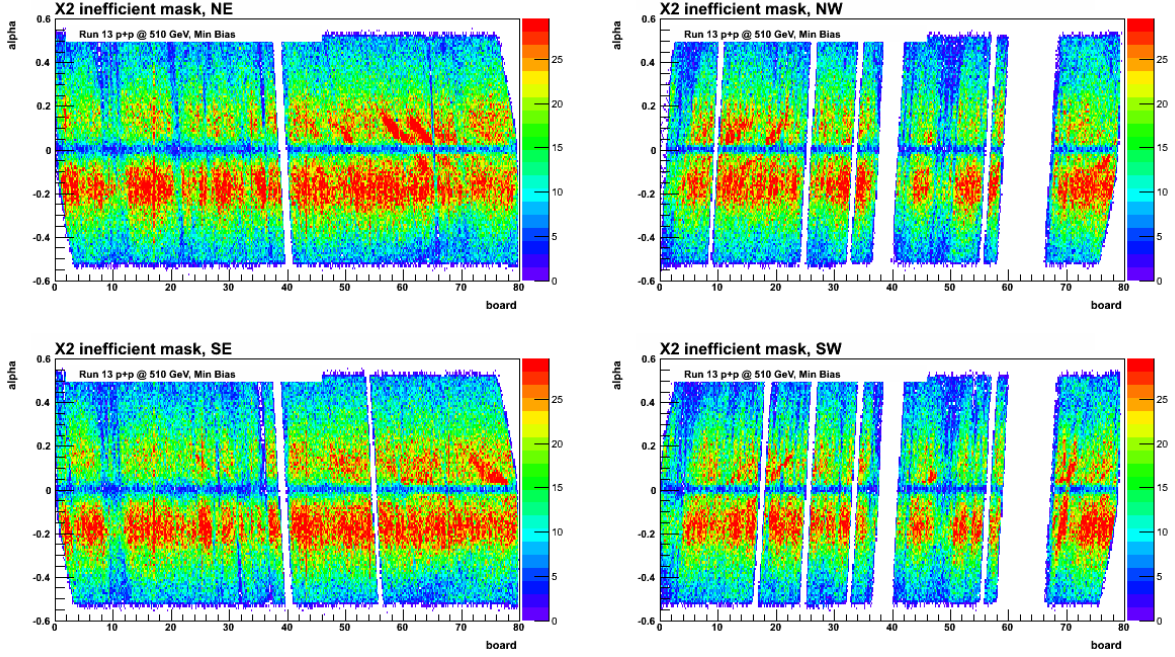


Figure 3.2: Similar to figure 3.1, but X2 bad or inefficient areas have been cut out and recorded for use for the modified quality cut.

3.3.2 Pair Cut

Track pairs close in the $\phi_{DC} - Z_{DC}$ space can be a result of ghosting phenomena. Ghosting is when a single track is reconstructed as two different tracks extremely close in $\phi_{DC} - Z_{DC}$ space. Ghost cut is used for same charge pairs and a conversion cut for different charge track pairs. The ghost cut for same charge pair:

- if $|\Delta\phi| < 0.024\text{rad}$ and $|\Delta Z| < 0.105\text{cm}$
 - if asymmetry < 0.3 , reject one track, else reject both tracks
 - where: $asymmetry = \frac{p_T^{track1} - p_T^{track2}}{p_T^{track1} + p_T^{track2}}$

Photon conversion occurring at the face of the DC will cause opposite charge track pairs close in $\phi_{DC} - Z_{DC}$. The conversion cut for opposite charged pairs,

- if $|\Delta\phi| < 0.07\text{rad}$ and $|\Delta Z| < 0.105\text{cm}$, reject both tracks.

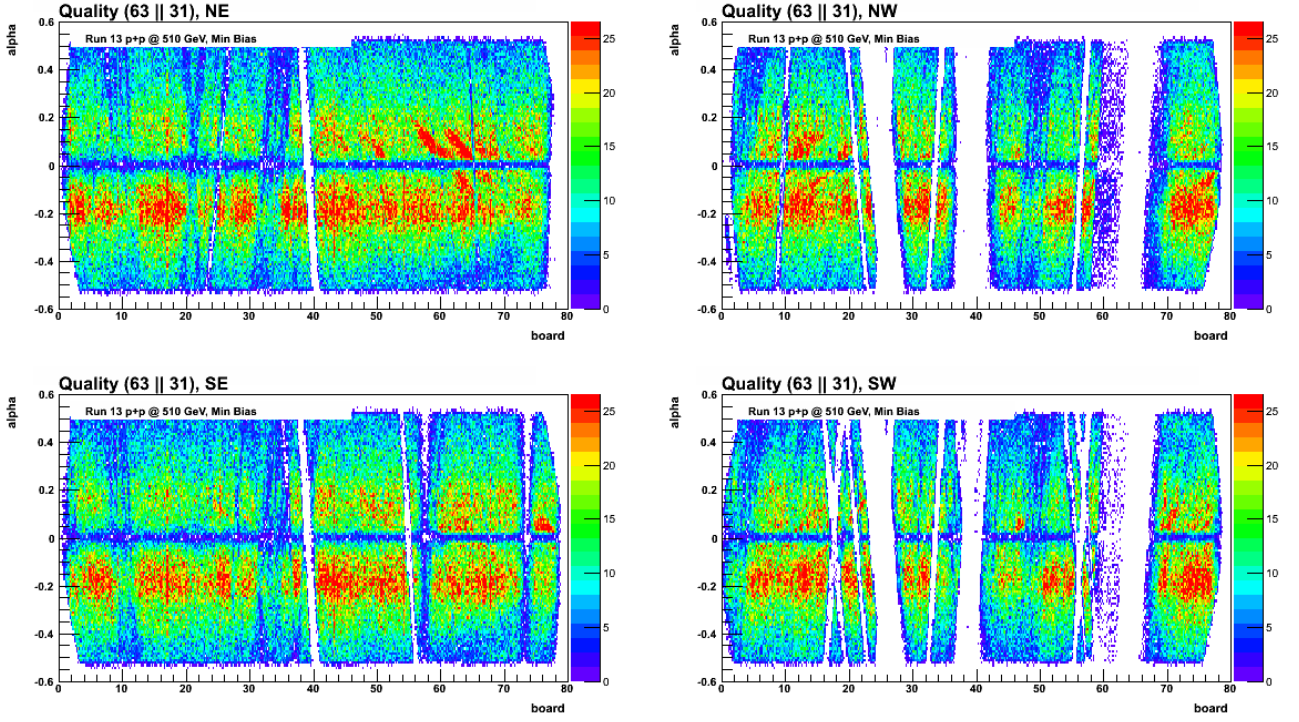


Figure 3.3: This shows the α vs. board using the quality (63||31) condition.

3.3.3 EMCAL and PC3 Matching

In this analysis, charged tracks are required to match to a hit in either the EMCAL or PC3. This will reduce the conversion electron³ tracks and hadronic backgrounds. Fake tracks from combinatoric are also reduced, e.g. three random hits or noise in DC lining up can be misconstrued as a track. The matching cut is enforced by computing the difference between the DC track model projections and actual hit in the EMCAL or PC3. The difference in ϕ and Z calculated and recorded as $d\phi$ and dZ . A small value of this difference distance (where $\text{distance} = \sqrt{dZ^2 + d\phi^2}$) means that the DC track is likely associated with the hit in the PC3 or EMCAL . The EMCAL (PC3) difference is written as $\text{emcd}\phi(\text{pc3}d\phi)$ and $\text{emcd}Z(\text{pc3}dZ)$. These distributions are expected to have Normal Gaussian distribution (mean of zero and sigma of one), but in reality do not. These variables must be calibrated

³Conversion pair cut in section 3.3.2 was for conversions occurring at face of DC only

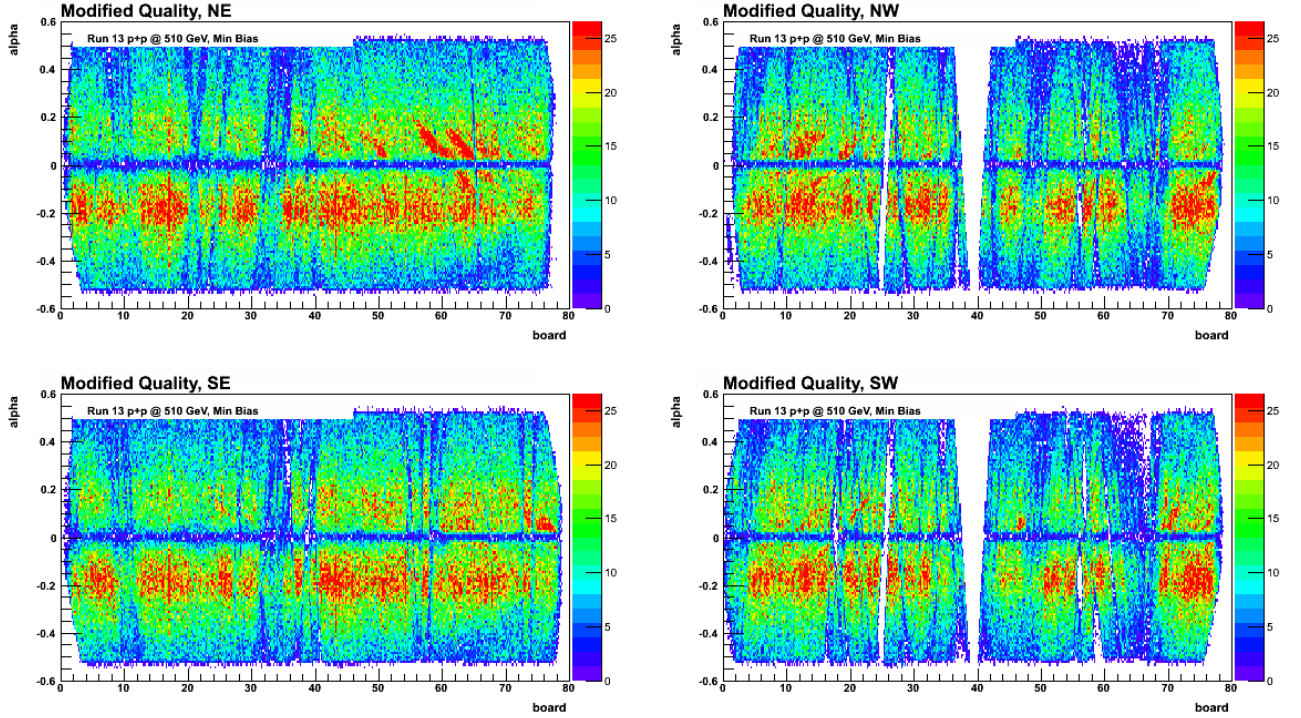


Figure 3.4: This shows the alpha vs. board using the modified quality condition.

to a normal distribution so that a single matching cut can be used for different track charge values, p_T , ϕ , η , and both PHENIX arms. A cut of $|\sqrt{dZ^2 + d\phi^2}| < 3.0(3\sigma)$ is used for the EMCal and PC3 matching. A resulting calibration mean and sigma are shown for a specific case in Figure 3.5. A detailed procedure on this calibration can be found in PHENIX analysis note an1105.

3.3.4 Secondary Track Cuts

The secondary track cuts are to specifically reject conversion electrons and were studied in Monte Carlo simulation by Arbin Timilsina[60]. The simulations are using the Run 13 setup with:

- Two π^0 with flat p_T from 1 to 11 GeV per event.
- Excluded Dalitz decays in events

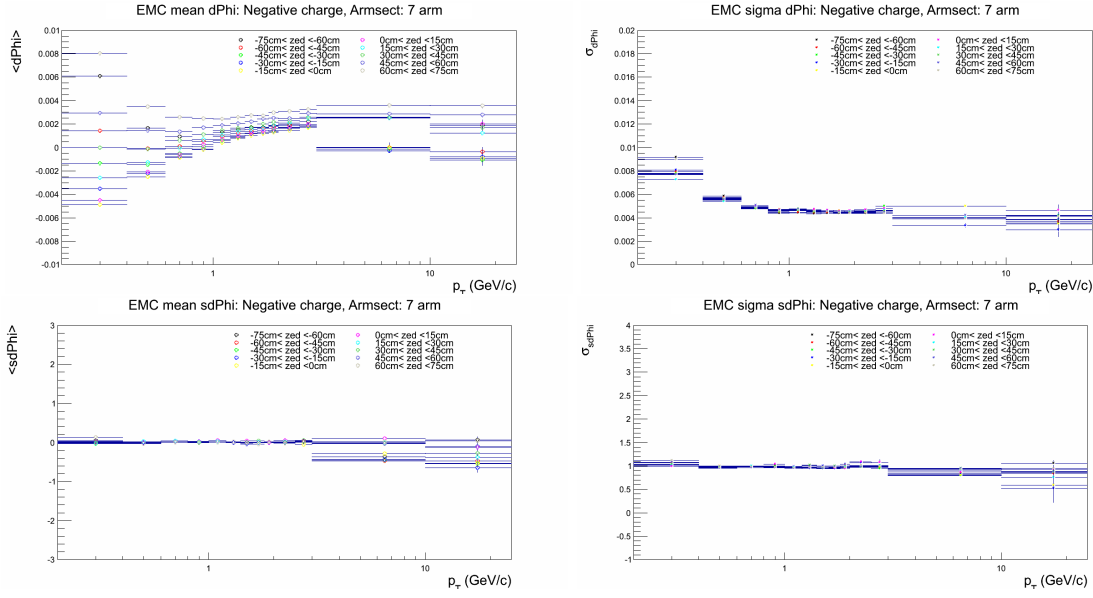


Figure 3.5: Top row shows the mean and sigma vs p_T for the EMCAL $d\phi$, while the bottom row shows the signalized mean and sigma vs p_T for EMCAL $d\phi$ calibration. The calibration brings the mean to ~ 0 and the sigma ~ 1 for all the p_T bins.

3.3.4.1 Central Arm Edges

The low- p_T ($p_{T, True} < 0.1$ GeV and $p_{T, Reco} > 4.0$ GeV) and conversion tracks get reconstructed as high- p_T tracks in the edges of the central arm, seen in Figure 3.6. The edge region is cut out by cutting on the ϕ of the track:

- $(\phi > -0.65 \text{ and } \phi < -0.49) \text{ or}$
- $(\phi > 0.89 \text{ and } \phi < 1.05) \text{ or}$
- $(\phi > 2.10 \text{ and } \phi < 2.26) \text{ or}$
- $(\phi > 3.62 \text{ and } \phi < 3.78)$

3.3.4.2 Electrons and Ecore

The low- p_T conversions that get reconstructed as high- p_T tracks do not deposit much energy into the EMCAL, and thus a minimum cluster energy cut can remove these tracks.

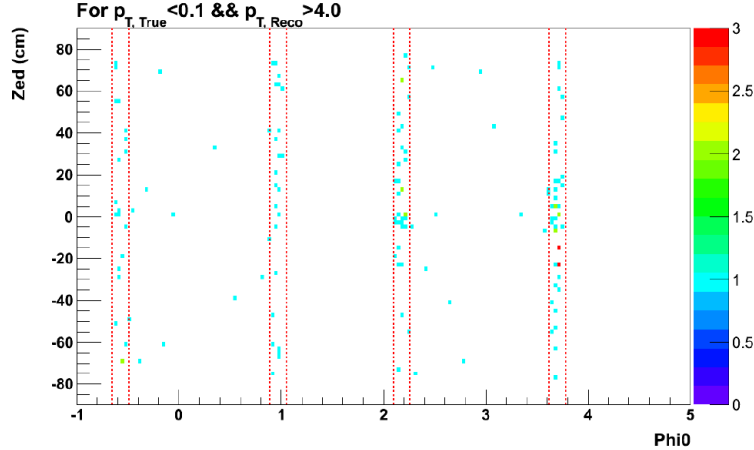


Figure 3.6: Red lines show the cut for the edge regions.

The cut is:

- EMC matching and minimum cluster energy, i.e.
- $\sqrt{sd\phi_{emc}^2 + sdZ_{emc}^2} < 3.0$ and ecore < 200 MeV

Electrons can be identified by using the n_0 ⁴ and track p_T . Figure 3.7 shows the ratio of the energy to momentum. Cut used to remove electron tracks:

- $p_T < 4.5$ GeV and $n_0 \geq 2$ and (ecore/momentum) < 0.6.

3.4 Cluster Selection

Clusters in the EMCal are formed by photons, π^0 decays, and neutral hadrons. The following sections describe the cuts used to select good clusters.

3.4.1 EMCal Hot/Dead Map

The EMCal Hot/Dead map was completed by Arbin Timilsina and Minghui Zhao following a standard EMCal calibration procedure. The hit distribution for each tower if fitted

⁴ n_0 is number of RICH phototubes fired in ring area

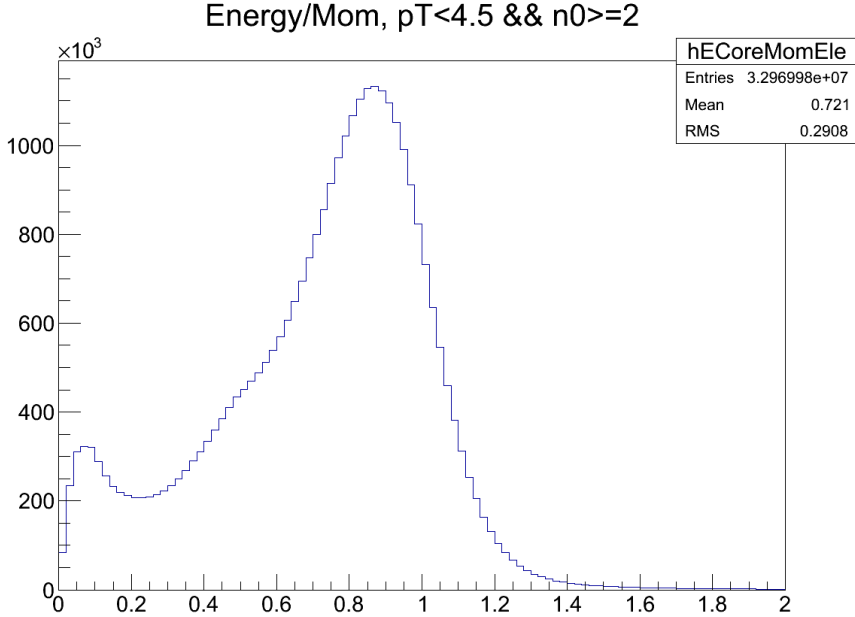


Figure 3.7: Ratio of Energy/Momentum of the electron candidates.

to a signal+background Gaussian function. A tower is considered 'hot ('dead')' if the total hits for that tower are above (below) the average for that sector by 3.5σ . The amount of hot/dead channels is a typical amount seen in other analyses. Figure 3.8 shows the map and the statistics on the hot/dead towers are:

- 143 out of 24768 are uncalibrated
- 1676 are dead (81 are dead&& uncalibrated)
- 1286 are hot (17 are hot && uncalibrated)
- 12.5% are hot, dead, or uncalibrated

3.4.2 Cluster Cuts

The hot and dead channels cannot be used for the cluster reconstruction and so the cuts to avoid those towers must be used. The cuts on clusters are as follows:

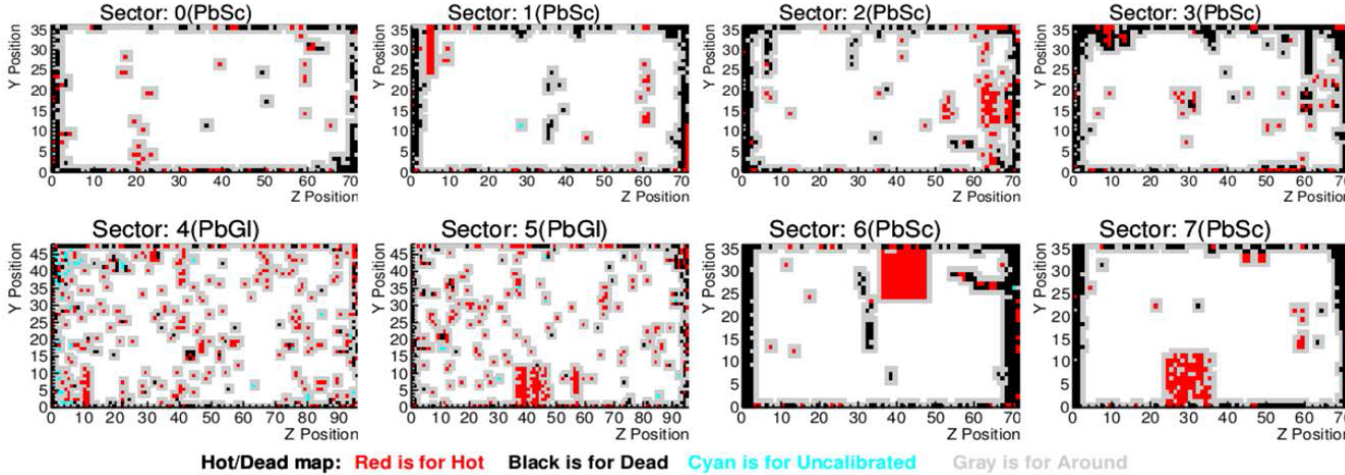


Figure 3.8: Hot/Dead for each EMCal sector.

- Energy > 500 MeV (minimum energy cut)
- Central tower of a cluster cannot be
 - hot or dead or uncalibrated tower
 - next to hot or dead or uncalibrated tower

3.4.3 Time of Flight

A time of flight (ToF) cut was used to ensure that clusters were from the collision vertex and not from some secondary source. The cut of ± 15 was used this analysis. The ToF distribution can be seen in Figure 3.9.

3.4.4 Cluster-track Matching

Charged tracks from electrons and hadrons deposit energy into the EMCal as well. Good clusters (pass the cluster cuts from section 3.4.2) which match well with these tracks are discarded. The matching conditions required by the track are:

- $p_T > 500$ MeV

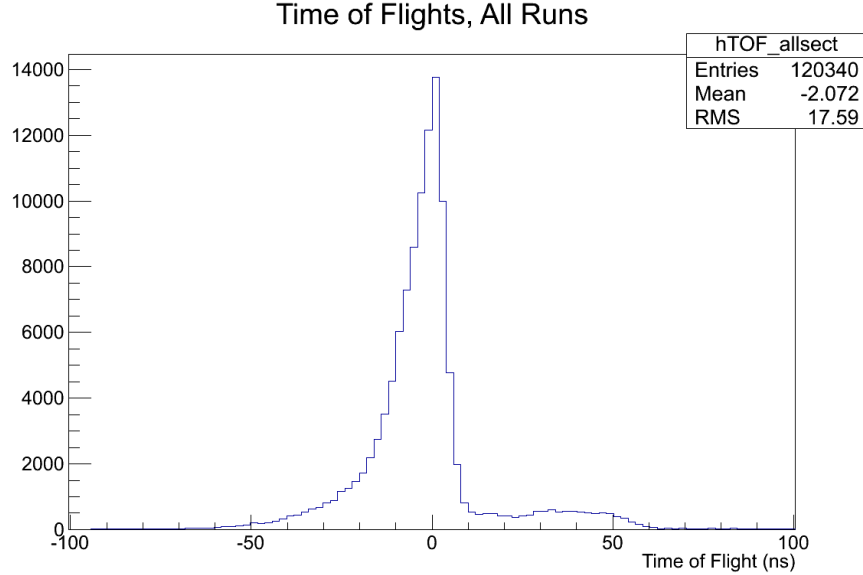


Figure 3.9: The Time of Flight distribution for EMCAL clusters.

- Pass DC modified quality cut
- $\sqrt{sd\phi_{emc}^2 + sdZ_{emc}^2} < 3.0$

3.5 Jet Reconstruction

Once there is a list of good tracks and clusters which pass the cuts described in previous sections, the Anti- K_T jet algorithm is used for jet finding. There are then cuts on the found jets which are described in the following sections.

3.5.1 Jet Level Cuts

The number of constituents (n.c) of jet greater than three is required. This cut helps reject jets that were reconstructed from combinatorial particles. A minimum jet p_T cut of $p_T > 6.0$ is made to remove the low p_T background. The charged fraction of an anti- k_T jet is the fraction of the jet p_T carried by charged tracks. Given by equation 3.3:

$$c.f. = \frac{1}{p_T^{jet}} \sum p_T^{tracks} \quad (3.3)$$

The charged fraction distribution and cut range of $0.2 < c.f. < 0.7$ for $n.c. \geq 3$ and $jetp_T > 6.0$ is shown in Figure 3.10. Charge fraction of 0 indicates that there were no charged tracks in the jet, and hence only EMCAL clusters. Charged fraction of 1 indicates that all the jet constituents are charged tracks. The kept region has a linear slope (on log scale) and is comprised of tracks and clusters.

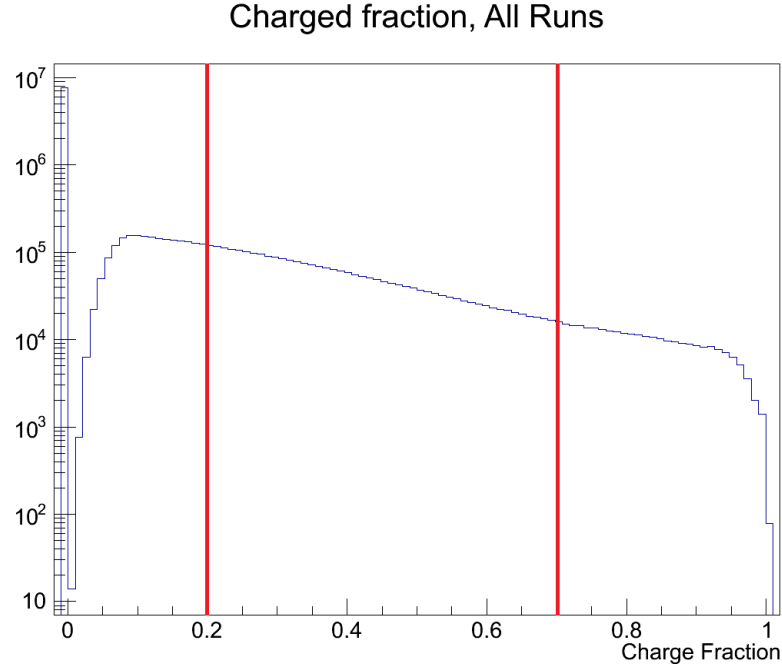


Figure 3.10: The area between the red lines is the good region which is kept.

3.6 Fake Jets Subtraction

Random uncorrelated particles can be misconstrued as fake jets which are jets not from the hard scattering, and so must be subtracted out. The method used to find the fake jets is described below:

1. When there is an event with **no** jets reconstructed, the (η, ϕ) position of the tracks and (η, ϕ) position of the clusters are randomly shuffled. The tracks (η, ϕ) and clusters (η, ϕ) are shuffled independently. The dead areas in the central arm detectors are accounted for in the shuffling. The shuffling is done for east and west arm separately.
2. The jet finding anti- k_T is done on the shuffled tracks and clusters. The jet level cuts are applied to the shuffled reconstructed jets.
3. Jets which pass the cuts are the "fake" jets.

Figure 3.11 shows the jet distribution, the fake jet distribution, and the fake jet subtracted distribution. The bottom half shows the ratio of the fake jets to the jets found. The majority of the fake jets are found at low p_T .

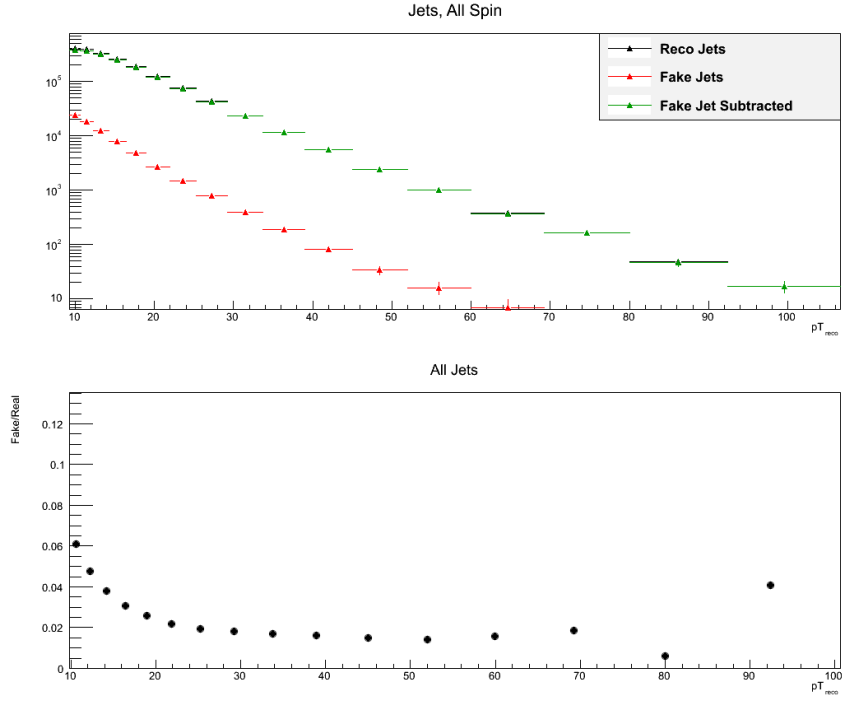


Figure 3.11: The top is the total jets found in black points, the fake jets in red, and the subtracted distribution in green. The bottom shows the ratio of fake jets divided by the total jets.

3.7 Spin Sorting

The jets which are found must be sorted by the proton spins for the A_{LL} measurement. The information about the spin for each run is stored in a PHENIX spin database. The information about the spin of the blue and yellow beam bunch, as well as the polarization of each bunch is stored in this database. The database stores values recorded at the RHIC interaction region, called 'IP12'. The data analyzed using PHENIX is at a different interaction region, and so a crossing shift needs to be accounted for to get the proper bunch identification number (ID). The crossing shift is also stored in the database, and so the proper bunch ID at PHENIX can be calculated using formula 3.4.

$$BunchID_{IP12} = (BunchID_{PHENIX} + crossingShift) \% 120 \quad (3.4)$$

The proper calculation can be checked by plotting the $BunchID_{IP12}$ vs Run Number for each event, which can be seen in Figure 3.12. The last nine bunches should be empty due to the abort gap, which is used for detector reset, etc. With this, the proper spin pattern for each bunch in PHENIX data is gotten.

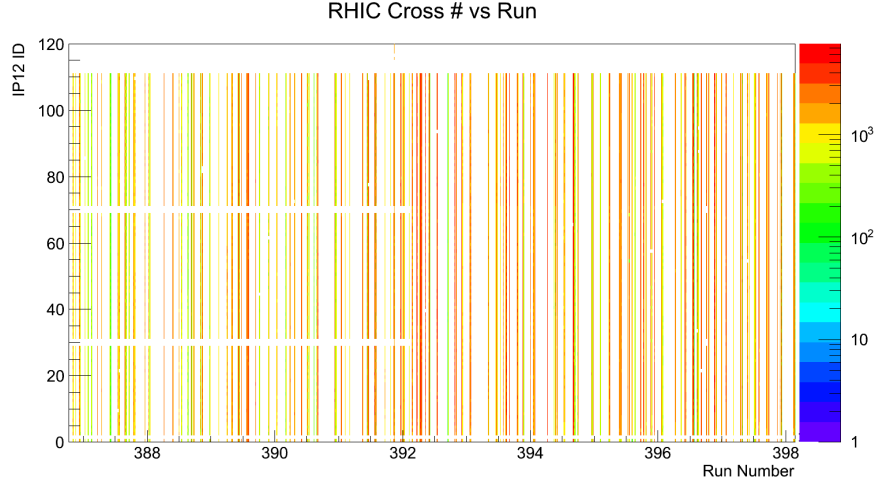


Figure 3.12: The empty region in the last 9 bins in the y-axis are the abort gap. This means that no collisions occurred and hence no events in that crossing ID.

3.7.1 Spin Pattern

The PHENIX spin database must be used to group jets according to spin pattern. The spin database gives +1 for positive spin and -1 for negative spin of the proton with respect to proton momentum (helicity) for each beam. Figure 3.13 explains this with a diagram. The spin pattern is described in Table 3.2.

Table 3.2: Spin Pattern Grouping

Spin Pattern	Blue Spin	Yellow Spin
0	+	+
1	-	+
2	+	-
3	-	-

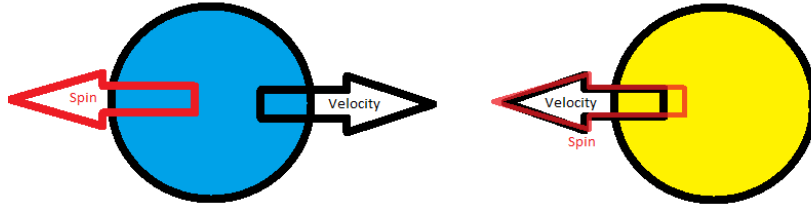


Figure 3.13: The left side shows blue helicity of -1 , which is when the spin is in the opposite direction of the velocity. The right side shows yellow helicity of $+1$, i.e. spin in same direction as velocity. This event would be spin pattern 1, according to Table 3.2

The jets are spin sorted according to the spin pattern. Notice that spin patterns 0 and 4 are when both protons have the same helicity, while the spin patterns 2 and 3 are when both have opposite helicities.

3.7.2 Relative Luminosity

The relative luminosity is the ratio of the number of collisions of each spin pattern. It was calculated using spin pattern 0 as the base. The number of jets found in spin patterns 1, 2, and 3 were individually divided by spin pattern 0. This was then multiplied by the number of raw BBC events for that run. This was to done to get a weighted average of

the relative luminosity for each spin pattern which was used in calculating the A_{LL} . The relative luminosity of the spin patterns are given in Table 3.3.

Table 3.3: Weighted Relative Luminosity

Spin Pattern	Relative Luminosity
1	0.998517
2	1.007
3	1.00431

The relative luminosity are close to 1 indicating that no spin pattern was favored over the others.

3.7.3 Beam Polarization

The average polarization of the beam was calculated similarly to the relative luminosity. The beam polarization gives the percent of protons which have spin in the same direction. This information is also gotten from the PHENIX database for both the yellow and blue beams for each run. The average polarization for blue and yellow are used in A_{LL} calculation and are given in Table 3.4.

Table 3.4: Average Polarization

Beam Line	Polarization
Blue	0.546029
Yellow	0.558057

3.7.4 Fake Jet Subtraction for Spin Pattern

The fake jets are found using method described in section 3.6 for each spin pattern. The jet distribution is subtracted by the fake jets and the resulting distribution is then used. The different fake jet subtracted distributions can be found in Figure 3.14, 3.15.

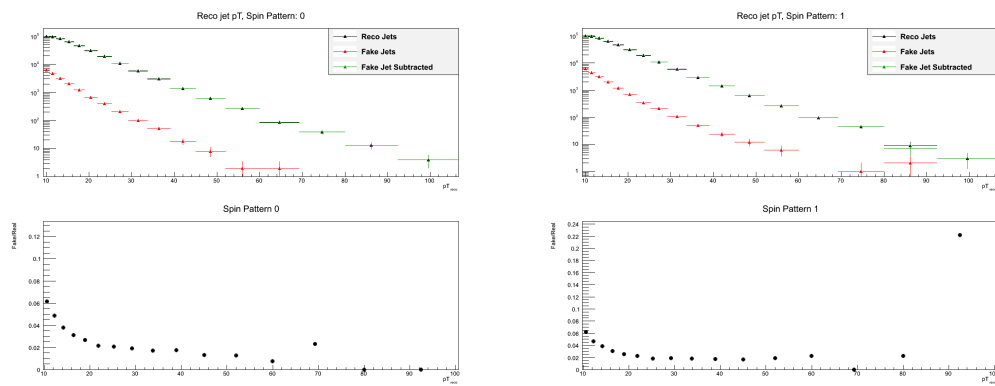


Figure 3.14: Left plot is spin pattern 0, right is spin pattern 1.

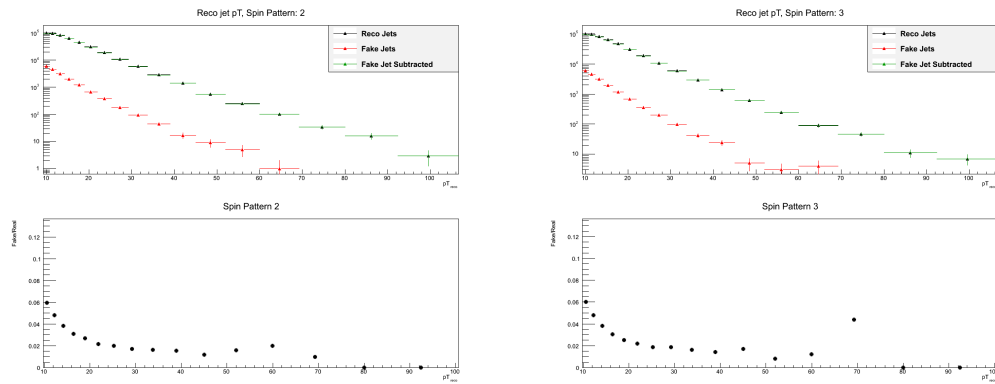


Figure 3.15: Left plot is spin pattern 2, right is spin pattern 3. Top plots are the total jets in black, fake jets found in red, and the subtracted in green. The bottom plots are the ratio of fake jets found to the total jets found for each bin.

CHAPTER 4. SIMULATIONS

The reconstructed jet distribution is in terms of $p_{T,Reco}$, not the true $p_{T,True}$ of the jet. The detector inefficiencies result in the misconstruction of energy and momentum and thus need to be corrected. Simulations are needed to determine how to properly change and correlate from $p_{T,Reco}$ to $p_{T,True}$. This is referred to as unfolding, i.e. unfolding the jet spectra from $p_{T,Reco}$ to $p_{T,True}$. Pythia is a Monte-Carlo simulation package which collides protons and produces list of resulting particles. PISA is a GEANT3 based simulation package which takes the particles produced from Pythia and propagates them through a realistic simulated construction of PHENIX. These were used to provide the response matrix and will be described in the following sections.

4.1 Pythia

Pythia can be configured to any setting the user wishes, and for this analysis the $\sqrt{s} = 510$ GeV for $p + p$ collisions was used. Pythia has different configurable 'tunes' which set various parameters to better match experimental observations. For this analysis, tune A was used since it gives best approximation of collisions seen at PHENIX[34][33]. Pythia also allows for the configuration of scattering processes and the energies of the processes. The Pythia settings for the tree level 2-2 QCD processes were used, described below.

- MSEL (11) : $q_i q_j \rightarrow q_i q_j$
- MSEL (12) : $q_i \bar{q}_i \rightarrow q_k \bar{q}_k$
- MSEL (13) : $q_i q_i \rightarrow gg$

- MSEL (28) : $q_i g \rightarrow q_i g$
- MSEL (53) : $g g \rightarrow q_k \bar{q}_k$
- MSEL (68) : $g g \rightarrow g g$

The kinematic range of the hard processes can also be set using CKIN(3) setting. The CKIN(3) sets the lower bound on the hard scattering p_T . The baseline simulations were done with CKIN(3) = 5 GeV setting, but additional simulations with higher CKIN(3) values were done and will be described in later sections.

4.2 PISA

PISA¹ is a GEANT3 package based software which provides a simulated version of the PHENIX detector. The particles generated in Pythia can be passed through PISA, which performs interactions between the particle and the simulated PHENIX detector and materials. A pisa.kumac file sets the detector configuration and any of the PHENIX detectors can be turned ON or OFF. In this analysis, the central arm detectors were turned ON and used. The detector dead areas were also configured in the simulations using the same hot/dead map of the EMCAL and the modified quality of the drift chamber as the experimental data. PISA outputs a data summary tape (DST) file, which is in the format of the real DST which are produced from PHENIX for analysis. From the simulations, the true and detector reconstructed energy and momentum are known and can be used.

4.3 Jet p_T Binning

The p_T dependence of the jet spectra is binned in an exponentially growing bin size. The sizes are different for the $p_{T, True}$ and $p_{T, Reco}$ and detailed below.

- Reco binning: Binned from 8.0 to 140 GeV with the ratio of adjacent bins being 1.15 times larger. E.g. First bin is from 8.0 to $8.0 * 1.15 (= 9.2)$ GeV, etc.

¹PHENIX Integrated Simulation Application

- Truth binning: Binned from 5.0 to 290 GeV with ratio of adjacent bins being 1.2 time larger. E.g. First bin is from 5.0 to $5.0 \times 1.2 (= 6.0)$ GeV, etc.

4.4 Simulation Acceptance

The simulations must match the detector setup of the data for accurate comparison. Thus the detector acceptance in the simulations must be checked and compared to the data acceptance. The modified quality cut for the drift chambers and the hot/dead map of the EMCal were checked. The modified quality comparison between the data and simulation hits can be seen in Figures 4.1, 4.2. The hot/dead channels of the EMCal in the simulations and data are shown in Figures 4.3, 4.4.

4.5 Cuts on True Jets

The pythia true jets are reconstructed from the truth information from pythia, and have a few cuts:

- The jet reconstruction on the true jets was done with the anti- k_T R = 0.3.
- The minimum $p_{T, True}$ on the jets, $p_{T, True} > 5.0$ GeV.
- The jet axis is required to be within $|\eta_{True}| < 0.35$

Notice there are no cuts on the charged fraction or number of constituents as with the reconstructed jets.

4.6 Different Kinematic Simulations

Pythia allows setting the minimum parton p_T of the hard scattering described in section 4.1. The CKIN(3) setting for majority of the simulations was CKIN(3) = 5 GeV. Larger settings were necessary to fill out the response matrix used for the unfolding with entries at higher p_T . In particular, simulations were run at values of CKIN(3) = 40, 50, 80, 100, 120,

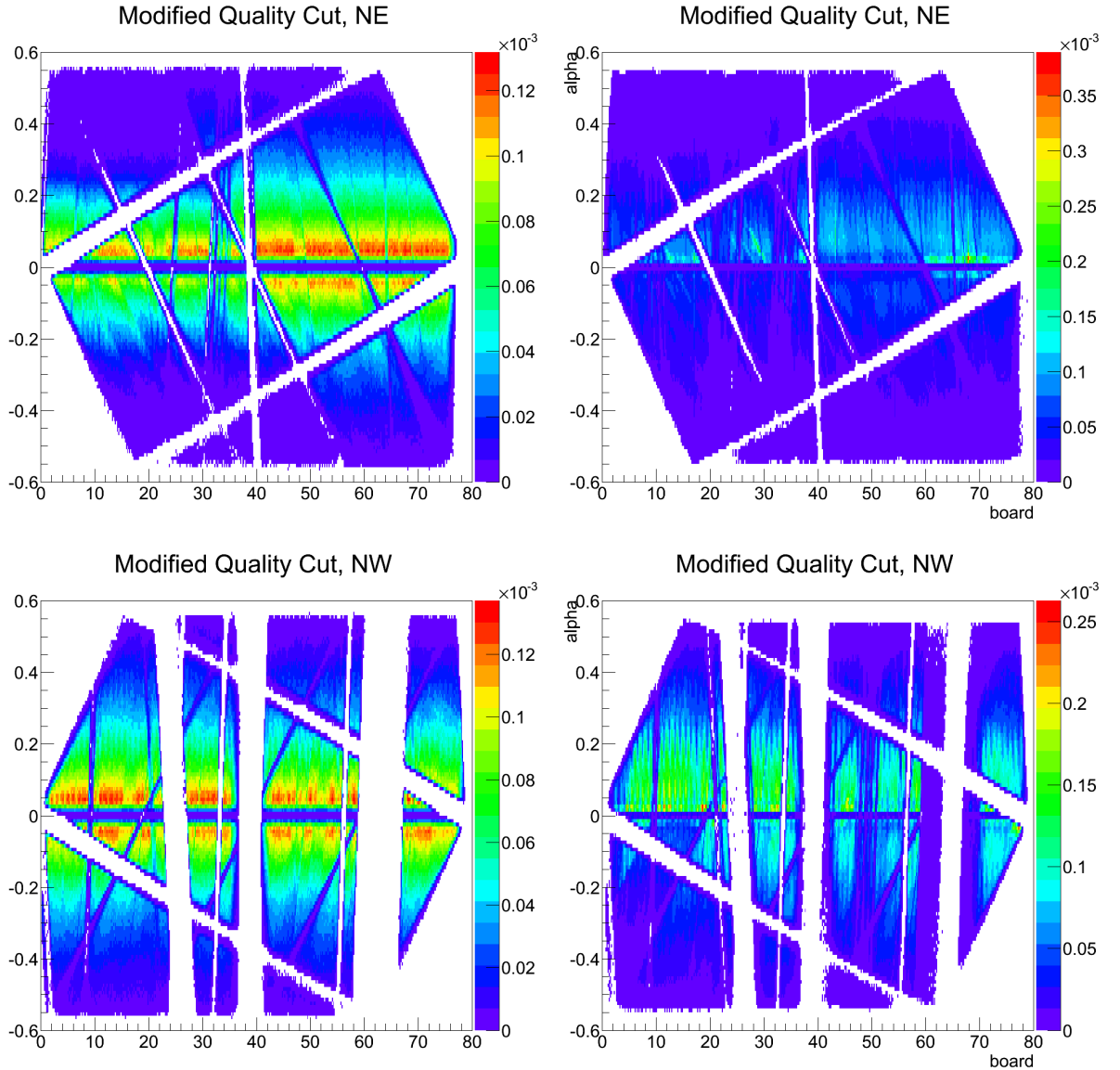


Figure 4.1: This shows the normalized histograms of the hits in the data on the left and the simulation hits on the right. The empty regions are the bad regions of the Drift Chamber and are similar in the simulations and data. Top plots are the NE and NW sections of the DC. SE and SW are shown below in Figure 4.2. E and W denote the different arms while N and S are north or south of the collision point in z-axis (along beam line).

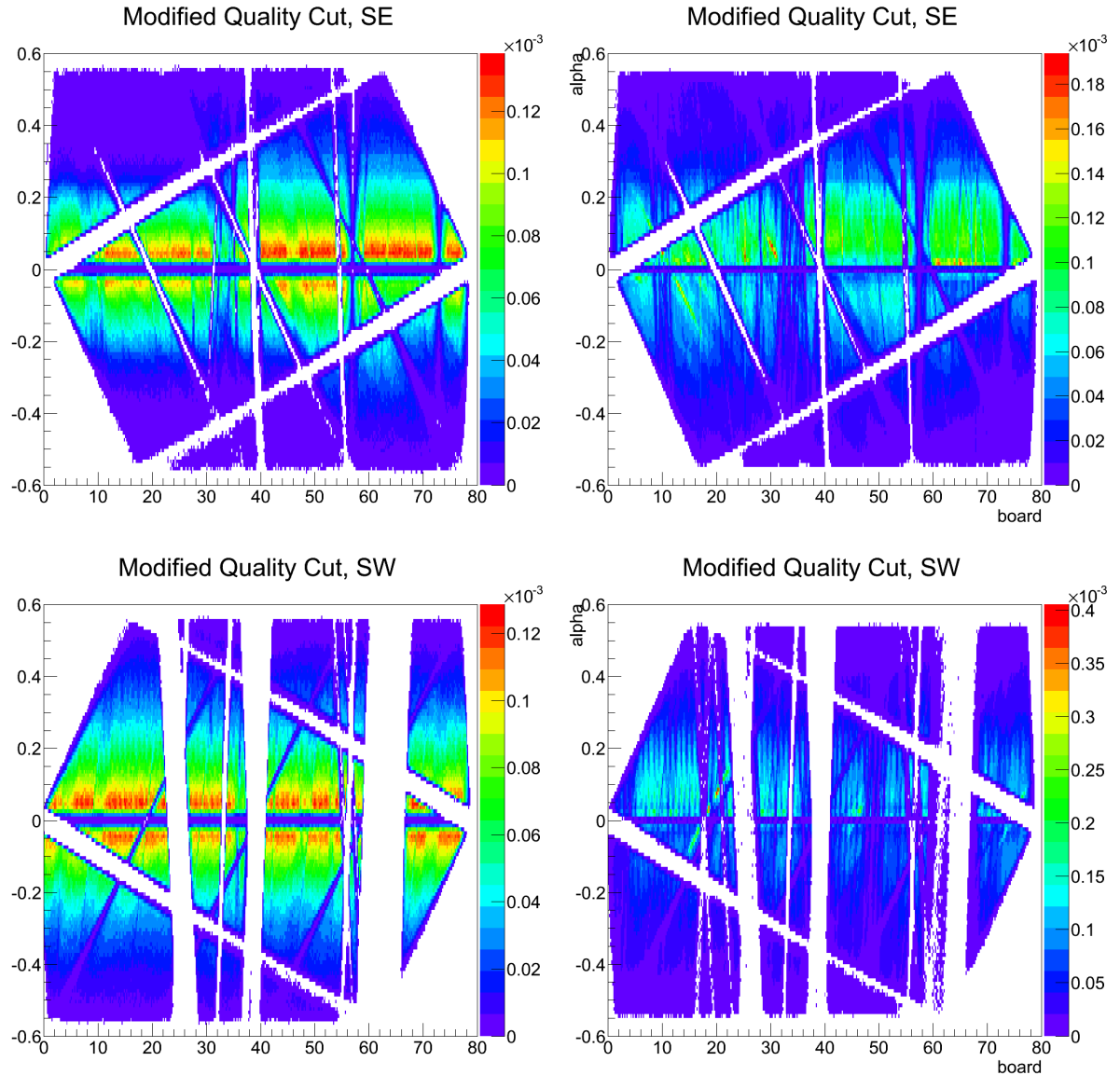


Figure 4.2: The SE and SW sections of the DC modified quality cut. The left is from data and right is from simulations.

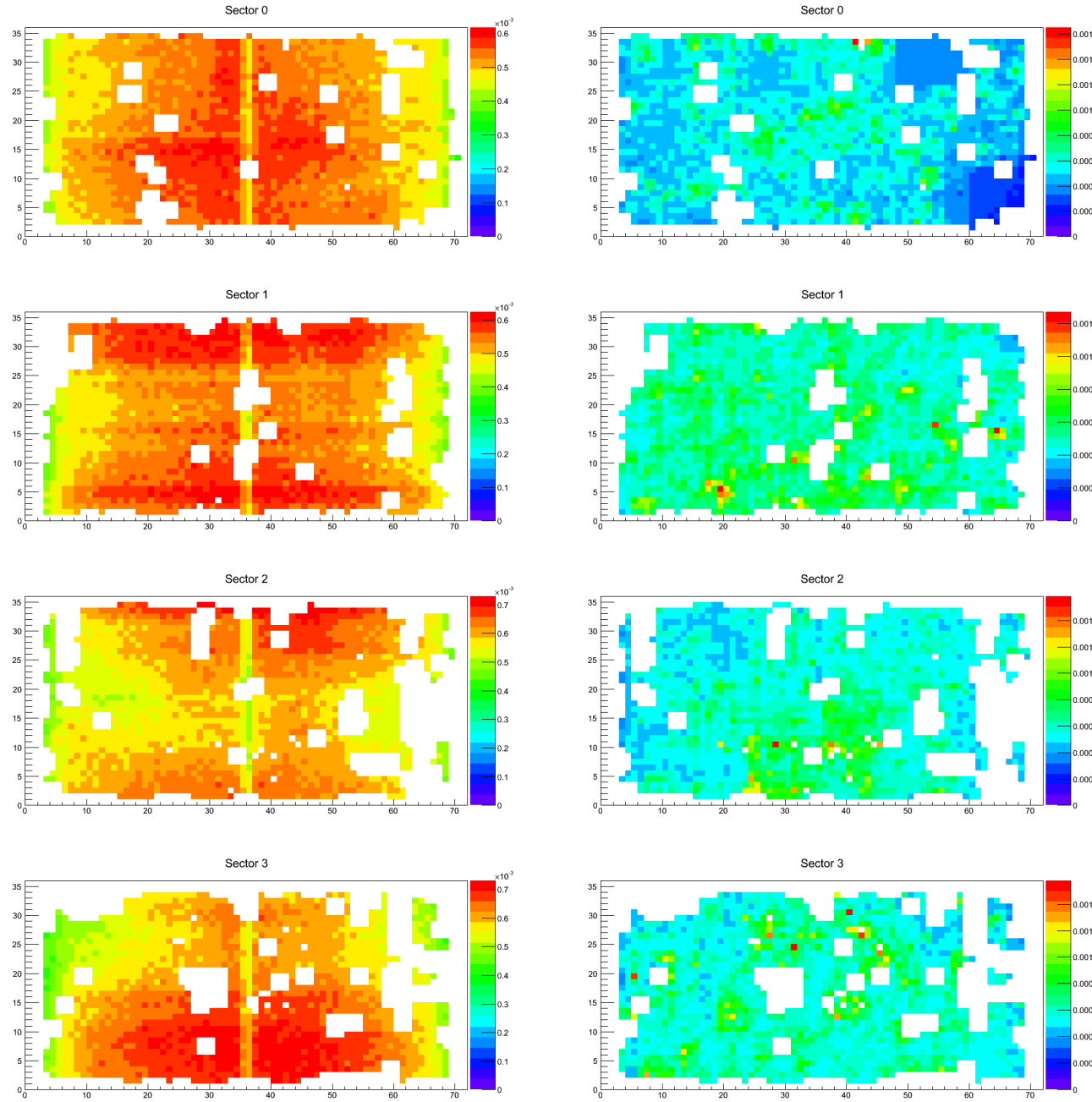


Figure 4.3: This is the 4 EMCal sectors of the west arm. The left plot is clusters in data while the right plot shows the clusters in the simulations.

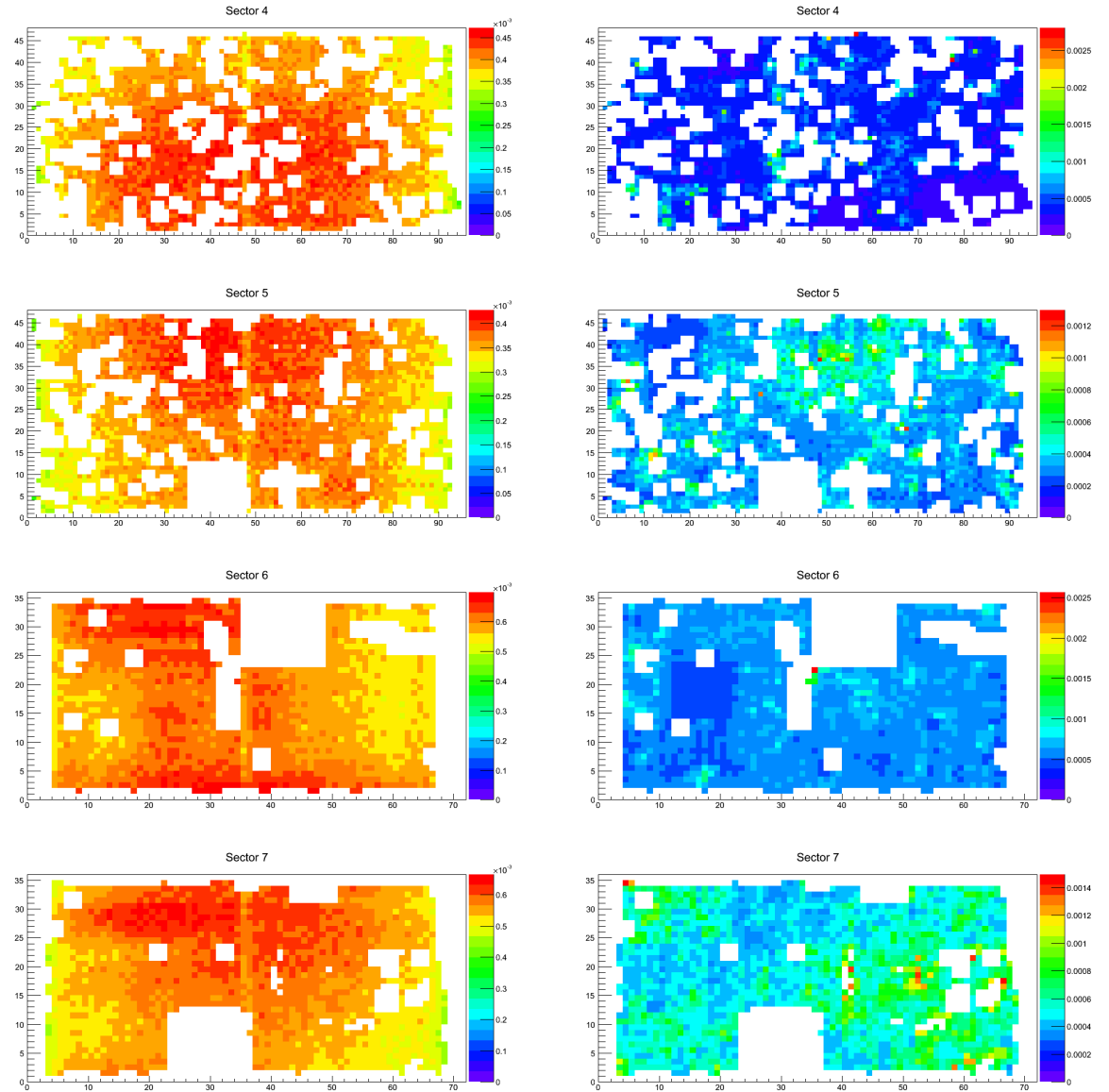


Figure 4.4: This is the 4 EMCal sectors of the east arm. Sectors 4 and 5 are the two PbGl sectors. The left plot is clusters in data and the right plot is clusters in simulation, as in Figure 4.3 for the west arm.

150 GeV. The response matrix combination from the different CKIN(3) will be detailed in later sections.

CHAPTER 5. PATH TO FINAL RESULTS

5.1 Combining Different Response Matrices

5.1.1 Ladder Method

There were pythia simulations ran at different $\text{ckin}(3)$ value ranges to properly fill out the response matrix at higher p_T bins. The $\text{ckin}(3)$ controls the minimum p_T value of the hard scattering processes, hence a higher $\text{ckin}(3)$ values results in jets found at larger p_T . The different $\text{ckin}(3)$ response matrices need to be properly scaled and combined into a total response matrix which can be used to unfold the reconstructed jets. The combination is done through an iterative 'ladder method':

- Get the scaling factor between the two different $\text{ckin}(3)$,
- Scale the larger $\text{ckin}(3)$ simulation histograms,
- Then take the weighted average to get a resulting combined histogram.

This ladder method takes two different $\text{ckin}(3)$ histograms, combines them together, then takes the resulting histogram and combines in a higher $\text{ckin}(3)$ histogram. This is applied until a final resulting histogram from all the $\text{ckin}(3)$. The $\text{ckin}(3) = 5 \text{ GeV}$ is used as a base which the larger $\text{ckin}(3)$ are scaled to at the beginning. The ladder starts with combining $\text{ckin}(3) = 5 \text{ GeV}$ and $\text{ckin}(3) = 60 \text{ GeV}$. First, the integral of the matched true p_T jets histograms (the y-axis of response matrix) of the different $\text{ckin}(3)$ are divided to find the scaling factor between them. The higher $\text{ckin}(3)$ is scaled down to match the matched

true p_T distributions. The lower ckin(3) and the scaled down higher ckin(3) histograms are added bin by bin using the weighted sum:

$$WeightedSum = \frac{\sum_i BinContent_i * BinWeight_i}{\sum_i BinWeight_i},$$

where i is the different ckin(3) histograms, (5.1)

$$\text{and } BinWeight_i = \frac{1}{BinContent_i}$$

The error is also calculated using proportion of errors:

$$\delta R = \sqrt{\sum_i \left(\frac{\partial R}{\partial X_i} \delta X_i\right)^2},$$
(5.2)

where R is the equation of weighted sum in equation 5.1. The method can be more clearly seen in Figure 5.1, which describes a one cycle of adding two different ckin(3) before the next iteration. The response matrices are combined in this fashion until a final resulting histogram which is used for unfolding.

5.1.2 Cross Section Scaling

Another way to combine histograms is to directly add the higher ckin histogram by scaling them with the cross section ratios. The cross section of each ckin is found from the simulation output files, directly from Pythia. The ratio is calculated as:

$$Ratio = \frac{\frac{C_{ckinHigher}}{N_{ckinHigher}}}{\frac{C_{ckin5}}{N_{ckin5}}},$$

$$Ratio = \frac{C_{ckinHigher}}{C_{ckin5}} \frac{N_{ckin5}}{N_{ckinHigher}},$$
(5.3)

where $C_{ckin5(Higher)}$ is the cross section of ckin 5 (Higher), and $N_{ckin5(Higher)}$ is the number of events in ckin 5 (Higher). The histograms can be added directly using that scaling. E.g ckin 40 is scaled by the appropriate ratio and add to ckin 5, then ckin 50 is scaled by the appropriate ratio and added to that histogram, etc. This method does not have any cutoff bins, and thus the full histograms are added which result in smoother distributions.

Ladder Method

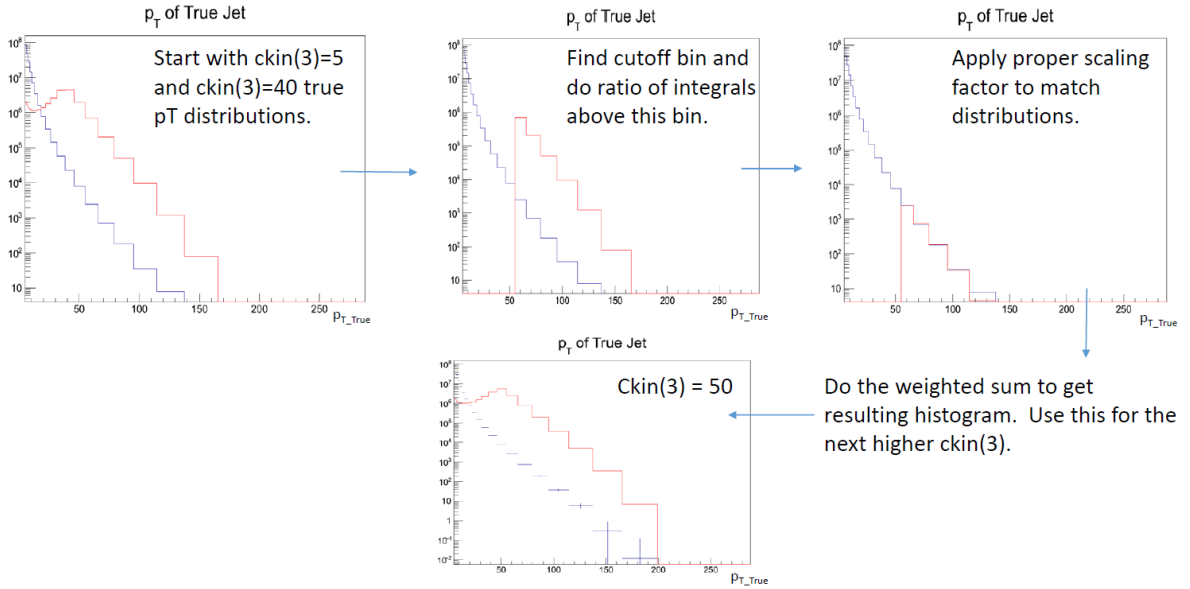


Figure 5.1: Top left starts with the $c_{kin}(3) = 5$ and $c_{kin}(3) = 40$ unscaled matched true p_T histograms. The higher $c_{kin}(3)$ histogram is integrated above the bin where the distribution starts to fall. The higher $c_{kin}(3)$ histogram is scaled using the ratio of integrals (of the histograms) then added using the weighted sum. The resulting histogram is then used to combine the next higher value $c_{kin}(3)$. Like taking steps up a ladder.

The response matrix is scaled up by its lowest value. The bin with lowest non-zero value in the response matrix is found and the histogram is scaled appropriately. The true jets distribution are also scaled with this value to ensure proper normalization when unfolding.

5.2 Unfolding

The A_{LL} requires the reconstructed jet spectra be in terms of the true p_T of the jets. The unfolding corrects for the energy resolution caused by the underlying event fluctuations and detector effects. A response matrix R_{ij} is formed in simulations using the matched jets pair of $(p_{T,Reco}, p_{T,True})$ and gives the probability of a generated event in true bin j to be found in the reco bin i , such that:

$$b_i^{ini} = \sum_j R_{ij} x_j^{ini}, \quad (5.4)$$

where b_i^{ini} is the histogram of Monte Carlo measured values and x_j^{ini} is the histogram of Monte Carlo true values.

The unfolding provides a meaningful way to solve the system of equations and determine the $p_{T,True}$ distribution x from a measured distribution b , such that:

$$b = Rx. \quad (5.5)$$

The inverted response matrix R can estimate x using:

$$x = R^{-1}b. \quad (5.6)$$

Even with an invertible response matrix, solving 5.6 directly usually leads to rapidly oscillating futile solutions. The singular value decomposition[40] (SVD) method is used in this analysis for unfolding. This was implemented by using software package called RooUnfold[9].

5.2.1 Singular Value Decomposition

The full description of SVD method can be found in [40]. The singular value decomposition of a $m \times n$ matrix A is its factorization of the form

$$A = USV^T, \quad (5.7)$$

where

- U is an $m \times m$ orthogonal, unitary matrix, i.e. $UU^T = U^TU = 1$
- S is a $m \times n$ diagonal matrix with non-negative real numbers on the diagonal, i.e. $S_{ij} = 0$ for $i \neq j$ and $S_{ii} = s_i \geq 0$
- V is an $m \times n$ orthogonal, unitary matrix, i.e. $VV^T = V^TV = 1$. V^T is the conjugate transpose of V.

The s_i are the singular values of matrix A and the columns of U and V are the left and right singular vectors. Using 5.7, the linear system of equations for the unfolding in 5.5 becomes:

$$Rx = b \Rightarrow USV^T x = b \quad (5.8)$$

This can be diagonalized using rotated vectors z and d :

$$z \equiv V^T x, \quad d \equiv U^T b \quad (5.9)$$

$$Sz = d \Rightarrow z = S^{-1}d \quad (5.10)$$

Since S is a diagonal matrix, only the diagonal $z_i = d_i/s_i$ will be calculated. The true distribution that is being solved for can be written as $x = Vz$. U and V are orthogonal, unitary matrices and are well behaved. SVD unfolding method reduces the problem down to calculation of $z_i = d_i/s_i$, which can be complex due to:

- Small values of s_i can cause the poorly known coefficients to have a much larger contribution.

- Some d_i can be insignificant due to errors from b (the reconstructed jets), since $d \equiv U^T b$

Small singular values can cause any statistical fluctuations in the reconstructed data to be magnified and cause some deformation in the unfolded distribution. The binning in the reconstructed data therefore must try to minimize statistical fluctuations. The reco and true binning is described in 4.3.

SVD method resolves the issue of solving for z_i by rescaling variables and equations by a scaling factor. The new regularized parameter is $z_i^{(\tau)}$:

$$z_i^{(\tau)} = \frac{d_i}{s_i} \frac{s_i^2}{s_i^2 + \tau} \quad (5.11)$$

For large values of $s_i \gg \tau$, $s_i^2/(s_i^2 + \tau)$ term will be close to 1. For small s_i , this will act as a low pass filter. As mentioned, small s_i or non-significant d_i (from errors in measured data) can cause issues with the unfolding. So one should choose $\tau \sim s_k^2$, where k is the index of the last significant d . The optimal way to choose the regularization (k) value is to plot $\log|d_i|$ vs i . This plot should have some distinct features which help with the selecting the regularization. For small values of i , the values of d_i are statistically significant and should fall exponentially. Near and after the critical value at $i = k$, the d_i should stabilize around $\log|d_i| = 1$. The regularization parameter k should be chosen near the value of i where this change in behavior occurs.

The parameter must be chosen appropriately since it can have a large effect on the unfolding at different parameters. Figure 5.2 shows the $\log|d_i|$ vs i of unfolding the total reconstructed jets. Choosing different k parameters has larger effects at higher p_T , and can be seen in Figure 5.3. Once the proper unfolding is done, there are a few corrections which need to be made.

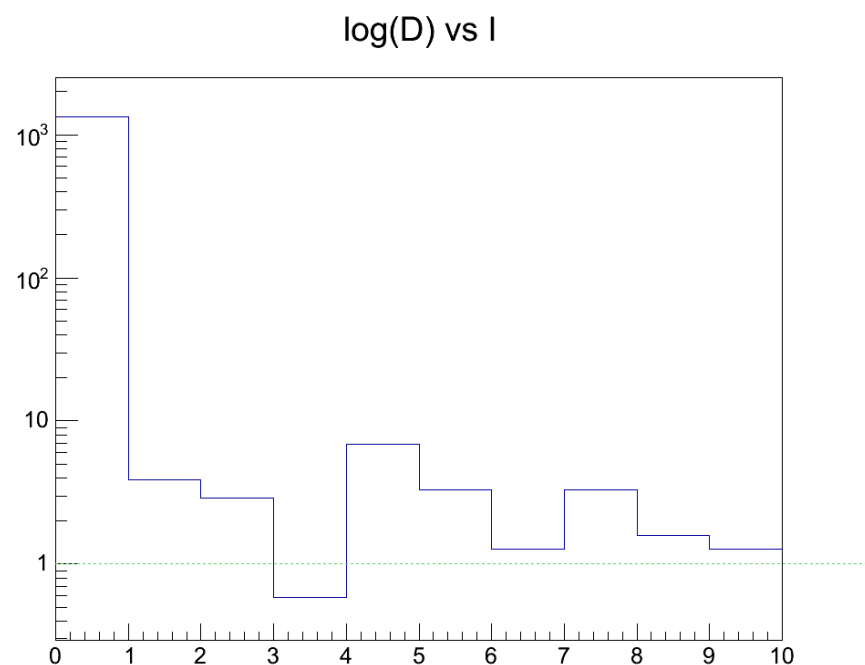


Figure 5.2: The $\log|d_i|$ vs i for unfolding the total reconstructed jets shows the behaviour of exponential drop until leveling out ~ 1 .

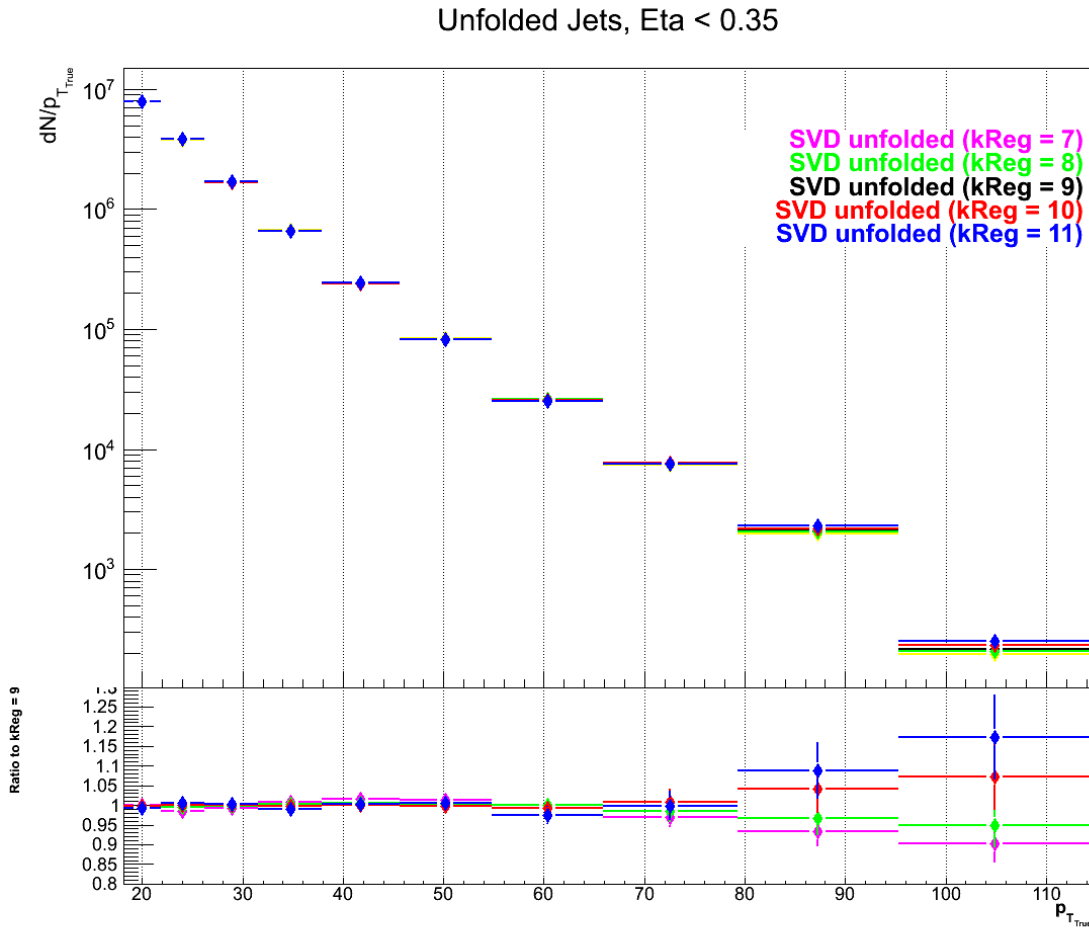


Figure 5.3: The top plot is unfolding using different k regularization values. The bottom shows the ratio of the different k regularization to chosen value of $k = 9$. There is a clear difference at the high p_T with different k .

5.3 Iterating Input

Iterating to match the input true jets spectrum to the unfolded jets is done to reduce sensitivity to the input spectra. The iterative procedure is as follows:

1. Unfold using proper regularization parameter.
2. Take the ratio between the unfolded and the true jet input spectra.
3. Use this ratio histogram to weight the response matrix and the true jet spectra.
4. Iterate until ratio smooth to 1.

The ratio of the unfolded to true can be seen in Figure 5.4. The response matrix and true jets are weighted by the appropriate ratio at each iteration.

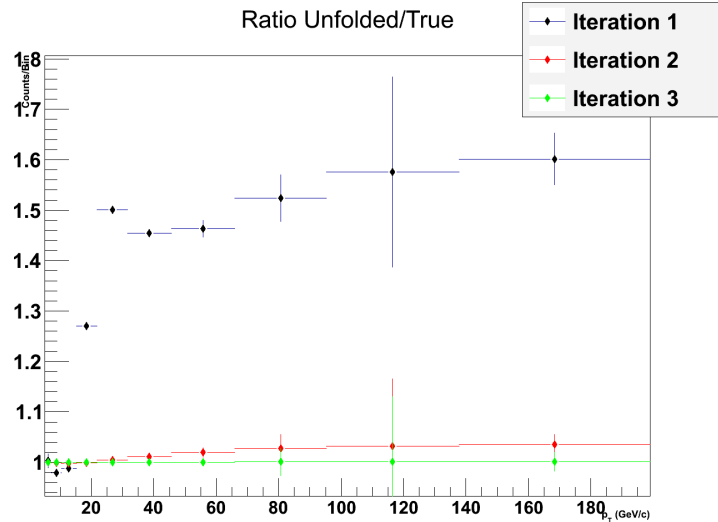


Figure 5.4: The ratio of the unfolded/true for the standard cuts for each iteration.

5.4 Different Cuts

Once the iterations are completed, the unfolded cross section can be obtained. There were different cuts applied to study the effects on the cross section and A_{LL} . The cuts were

primarily on the tracks to cut down on high p_T contamination. The different cuts are as follows:

- Standard cuts.
- 2.5σ on PC3 and EMC sdphi/sdz matching. See 3.3.3 for details on matching cut.
- 1.5σ on PC3 and EMC sdphi/sdz matching.
- Tighter DC conversion cuts: $|dPhi| < 0.018(0.04)$, $|dZed| < 0.07(0.07)$ of the DC for same (opposite) charge. See 3.3.2 for standard cut.
- Tighter CF cut: $(0.2, 0.7) \rightarrow (0.3, 0.6)$. CF defined in 3.5.1.
- Combination of cuts: 2.5σ , CF cut, and conversion cut.

In the 2.5σ trial, *only* the matching cut is different from the standard cuts. There are six different trials and thus six different reconstructed jet spectra and response matrices. The reconstructed jet spectra for each cut is shown in Figure 5.5.

The response matrices are shown in Figure 5.6.

5.5 Cross Section

The appropriate response matrix, true jets, and reconstructed jets were used to do the unfolding. The total reconstructed jets were unfolded and the unfolded jets were scaled using 32.5 mb luminosity factor for the BBC cross section. The total scaled value is the luminosity/number of events, which comes to: $32.5\text{E}9/6.95806\text{E}12$. This cross section can then be compared to the theory calculated. Figure 5.7 shows the unfolded cross section for the different cuts which were studied. Table 5.1 lists the average $p_{T, True}$ and the cross section for that bin.

The cross sections in Figure 5.7 are all within 10% of the standard cuts cross section. The bottom plot, which shows the ratio of the different cuts to the standard cuts, illustrates

Reco jet pT

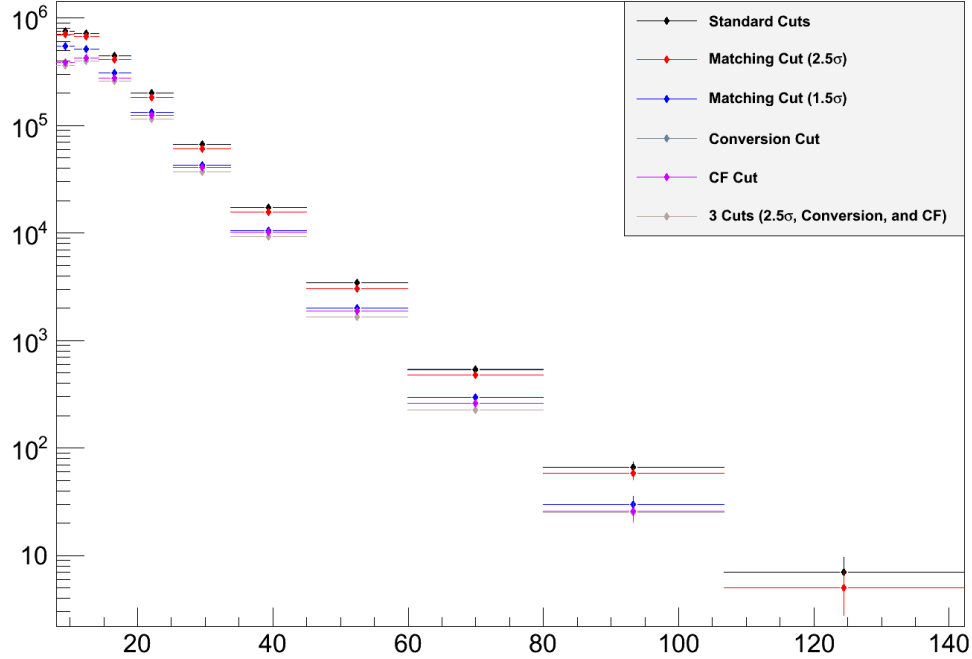


Figure 5.5: The raw jet distribution for the six different cuts described. These are not ERT trigger efficiency corrected.

this. The unfolded cross section is higher than the theory prediction, especially at high p_T . The cuts on track matching and conversion were done to reduce the high p_T tracks, however those cuts do not show a noticeable decrease in the cross section. The response matrix must correct for these cuts and bring the cross section similar to the standard cuts cross section.

5.6 A_{LL}

The spin sorted jets are unfolded using the same method described for the total jets used for the cross section. The spin sorting is described in Section 3.7. The A_{LL} is calculated as:

$$A_{LL} = \frac{1}{P_B P_Y} \frac{N_{++} + R_{--} N_{--} - R_{+-} N_{+-} - R_{-+} N_{-+}}{N_{++} + R_{--} N_{--} + R_{+-} N_{+-} + R_{-+} N_{-+}} \quad (5.12)$$

where the 'R' is the relative luminosity with respect to the (++) configuration. The

Table 5.1: Table of cross section and average $p_{T,True}$ for each bin. Note: Only bins 4-9 are shown in Figure 5.7.

Average $p_{T,True}$	Cross Section
6.1136	2.19707e+07
8.47282	6.66337e+06
12.1062	1.43579e+06
17.5237	326695
25.1574	62324.5
35.9814	8827.13
51.8159	1135.09
74.0517	104.593
104.82	4.3467
168.382	0.0125754

same (++, -) and opposite (+-, -+) configuration are combined to give two distributions.

These are then unfolded and the A_{LL} is calculated as:

$$A_{LL} = \frac{1}{P_B P_Y} \frac{N_{Same} - N_{Opposite}}{N_{Same} + N_{Opposite}} \quad (5.13)$$

The errors on the A_{LL} are calculated using the propagation of errors formula:

$$\delta A_{LL} = \sqrt{\left(\frac{\partial A_{LL}}{\partial N_{Same}} \delta N_{Same} \right)^2 + \left(\frac{\partial A_{LL}}{\partial N_{Opposite}} \delta N_{Opposite} \right)^2} \quad (5.14)$$

5.6.1 Bunch Shuffle

Bunch shuffling is done to ensure the A_{LL} result is statistically significant. The spin pattern of each beam (yellow and blue) is randomized for each event and the jets found in that event are then grouped accordingly, i.e (++, +-, etc.). This shuffling is done 5000 times and the $\frac{A_{LL}}{\text{Error}_{A_{LL}}}$ is calculated for each shuffle. The $\frac{A_{LL}}{\text{Error}_{A_{LL}}}$ for each bin are plotted and fit to a Gaussian. This distribution should a normal distribution and thus ensuring the A_{LL} is peaked at 0 with random spin sorting. Figure 5.8 shows the distribution of A_{LL} for each bin. Figures 5.9, 5.10 show the mean and sigma of each bin. The signalization in higher p_T bins is due to low statistics.

5.6.2 Unfolding Systematic

The A_{LL} was calculated for the different sigma cuts, as shown in Figure 5.11. This was used to calculate the systematic uncertainty of the unfolding. The 2.5σ trial was taken as the base, and the 1.5σ and the standard cut of 3.0σ were subtracted. The average of the two differences was used as the unfolding systematic.

5.6.3 Fakejet Systematic

The data was rerun with conditions:

- cluster energy $> 2.0GeV$
- track $p_T > 2.0GeV$

where the default is cluster energy $> 0.5GeV$ and track $p_T > 0.5GeV$. The larger energy cut data is not fakejet subtracted like the default, but is scaled up to match the distributions at high p_T , as seen in Figure 5.12. The larger energy cut jets are unfolded using the response matrix from the default conditions. This is in effect replacing the default jets with the larger energy cuts to see how this . The comparison between the default cut and fakejet systematic unfolded can be seen in Figure 5.13. There is $\sim 10\%$ difference between the two and the absolute difference between the two are used to set the systematic uncertainty.

5.6.4 Result

The A_{LL} was calculated as mentioned in the previous sections, and the result is shows in Figure 5.14. Figure 5.14 shows the A_{LL} from the unfolded and from the raw reconstructed jets, as well as previous measurements from STAR, and the theory predictions from Kang, et al. The points shown are the below the cutoff bin of statistics, as mentioned in the previous section. This can be seen in the plot where the black points from raw A_{LL} start to show significantly larger error bars. A larger range of the unfolded is shown in Figure 5.15.

The raw A_{LL} are in terms of the reconstructed $p_{T,Reco}$ and are converted to $p_{T,True}$ using the response matrix. The projection of $p_{T,True}$ for each bin in $p_{T,Reco}$ is taken, then the mean of that projected $p_{T,True}$ used for that data point. This $p_{T,True}$ is then converted to $x_{T,True}$.

Table of values for the unfolded A_{LL} is shown in Table 5.2. Table of values for the raw A_{LL} is shown in Table 5.3.

X_T	A_{LL}
0.0196078	0.00226718
0.028342	0.00278002
0.0409667	0.00376339
0.0592149	0.00500248
0.0855914	0.00618616
0.123717	0.00718348
0.178825	0.00797408
0.258482	0.00856835
0.37362	0.00896504
0.540045	0.00916351

Table 5.2: Table of A_{LL} values for each x_T . Note: the last two bins were not show in Figure 5.14

X_T	A_{LL}
0.052736	0.00364217
0.0683941	0.00715294
0.0887292	0.00250003
0.114322	0.0116475
0.147597	0.0151769
0.18754	-0.0390849
0.239557	0.00790291
0.290402	0.170774
0.408779	0.00364185

Table 5.3: Table of raw A_{LL} values for each x_T . Note: the last four bins were not show in Figure 5.14

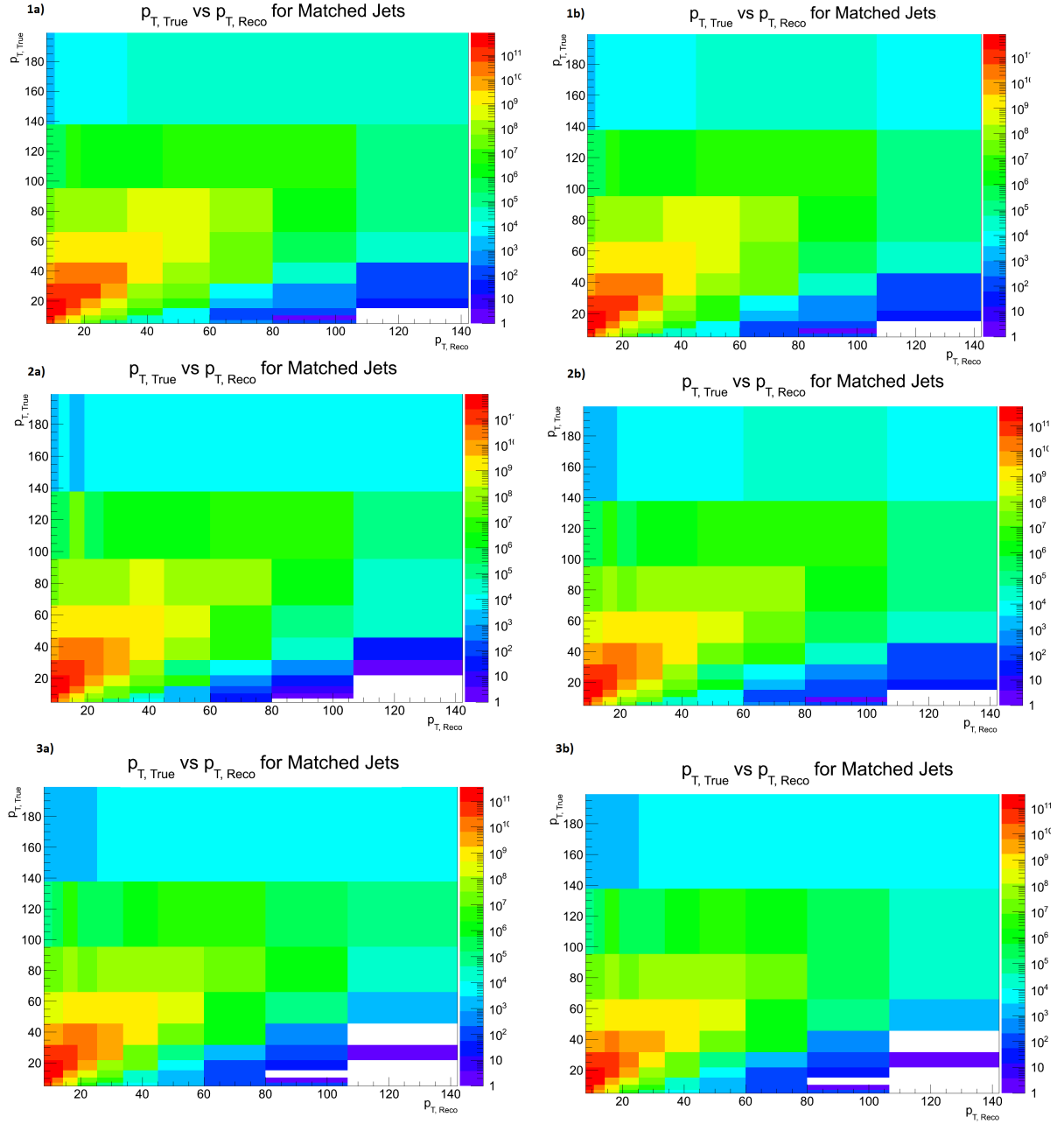


Figure 5.6: The response matrix 1a) is for standard cuts, 1b) for the 2.5 σ cut, 2a) for the 1.5 σ cut, 2b) for the DC conversion cuts, 3a) for the tighter CF cut, and 3b) for the combination of 3 cuts.

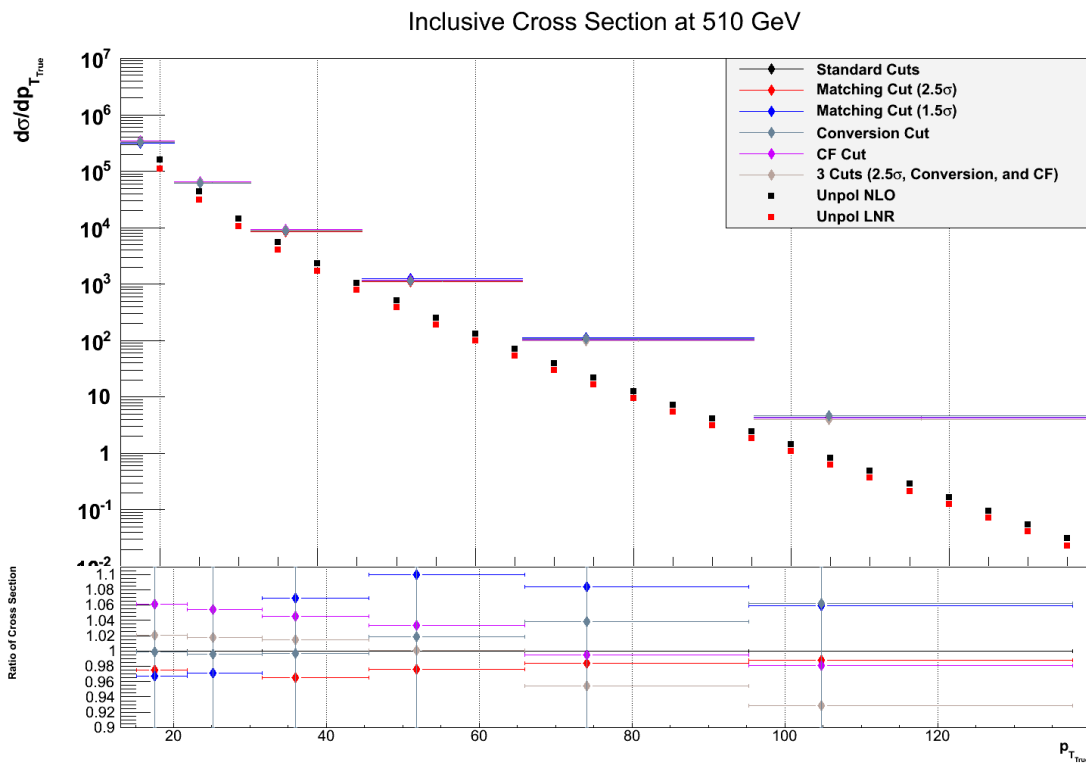


Figure 5.7: The top plot is showing the unfolded cross section with the different cuts as well as the theory predictions. The bottom plot is showing the ratio of the standard cut to the different cuts. The cross section points are plotted at the p_T weighted mean.

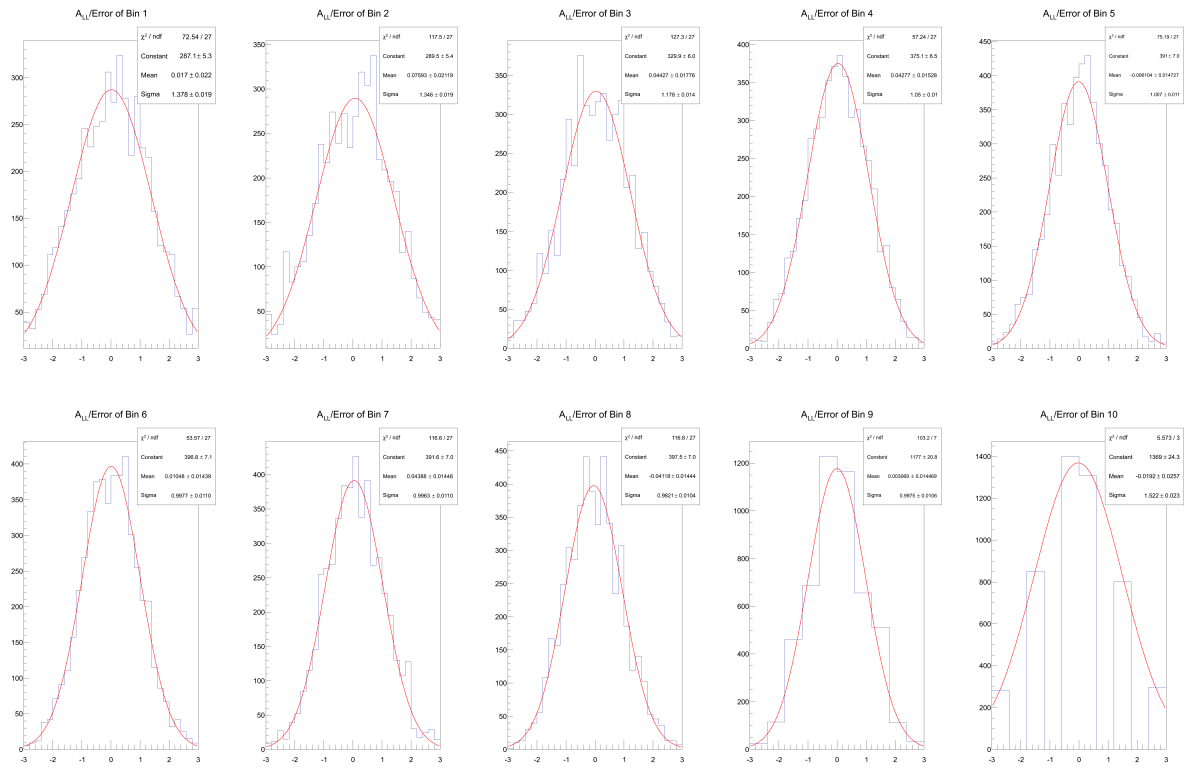


Figure 5.8: $\frac{A_{LL}}{\text{Error}_{A_{LL}}}$ for each p_T bin.

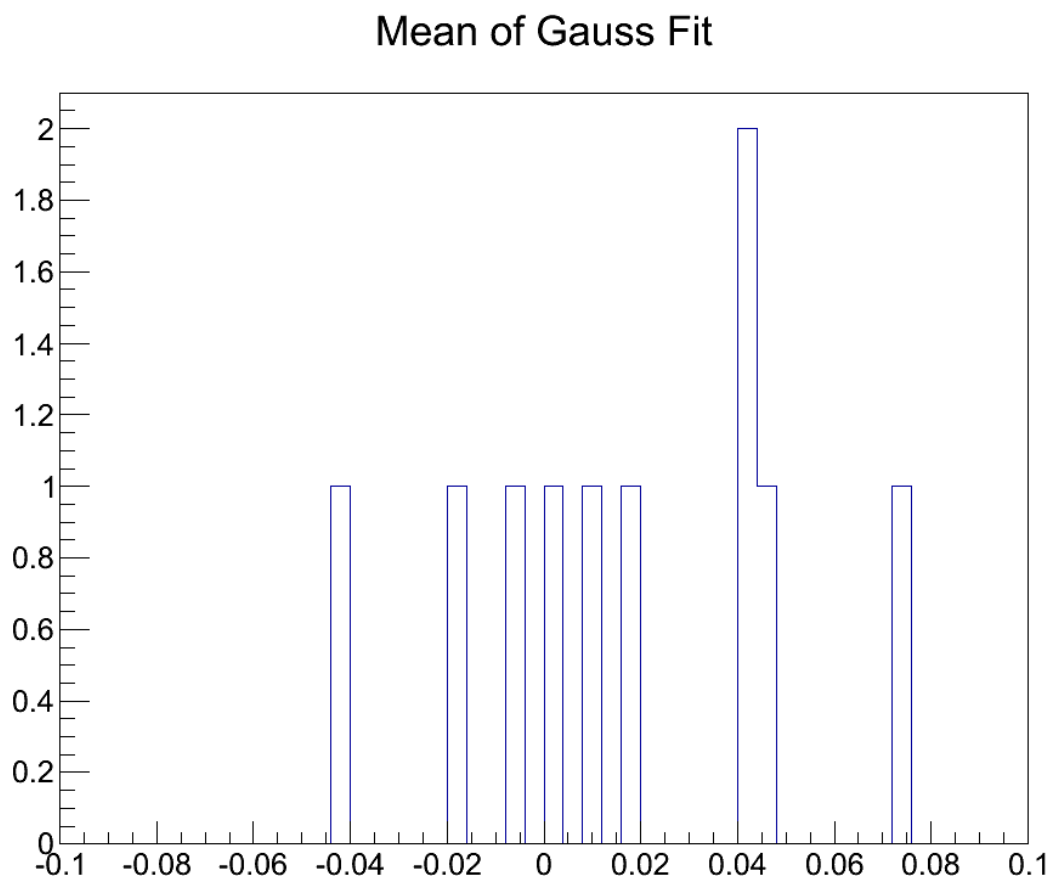


Figure 5.9: Means of Gaussian fit (shown in Figure 5.8 for each bin).

Sigma of Gauss Fit

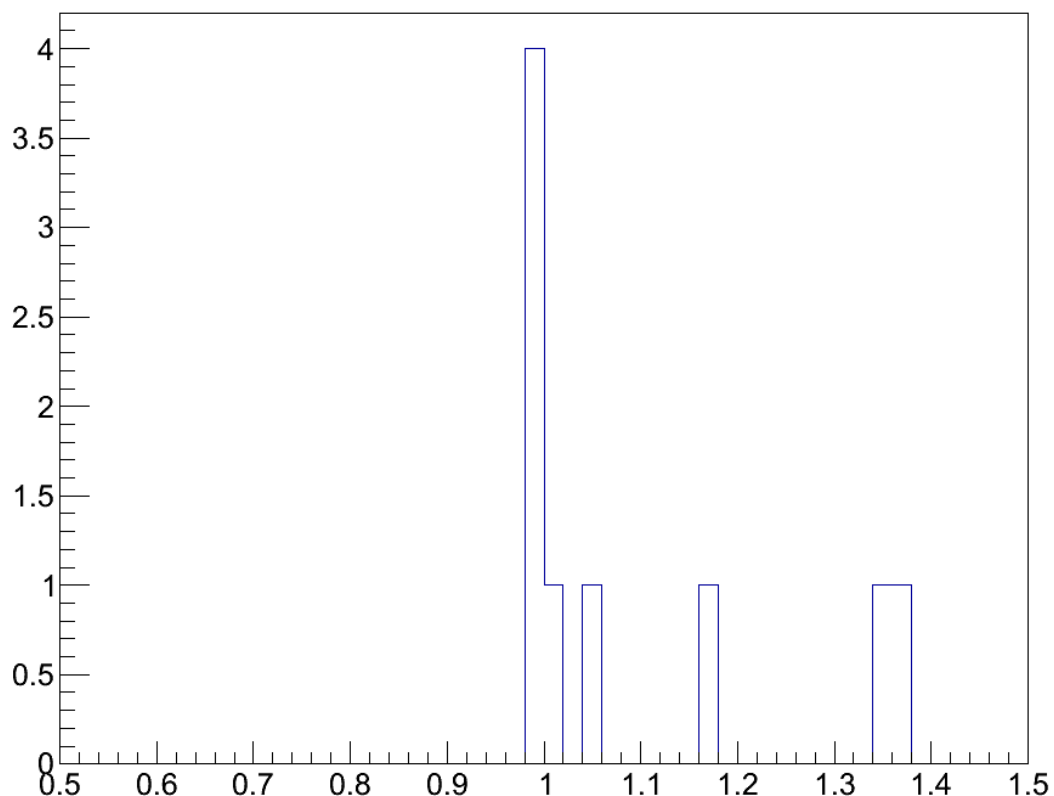


Figure 5.10: Sigmas of Gaussian fit (shown in Figure 5.8 for each bin).

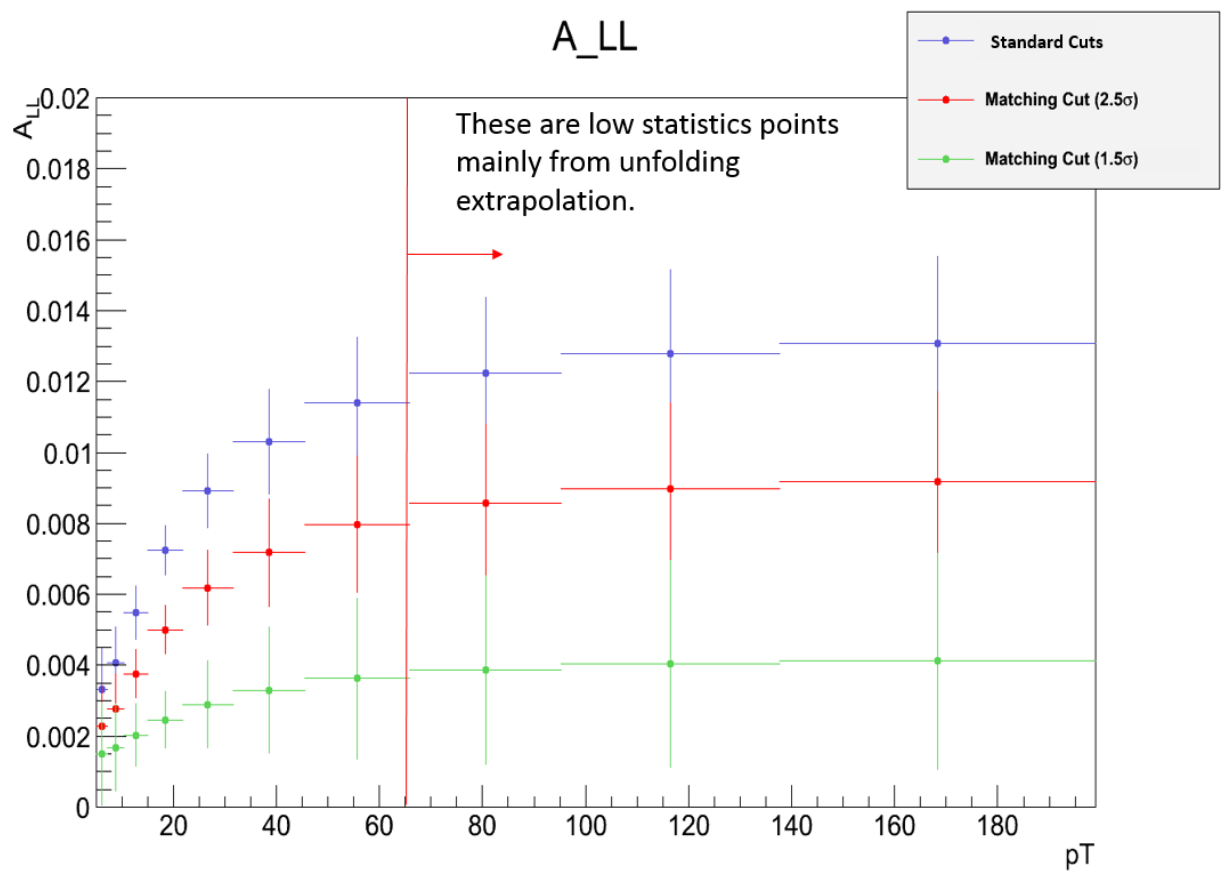


Figure 5.11: This shows the unfolded A_{LL} for the different sigma cuts. The high p_T points are driven more by the unfolding than data and the red line shows the bin boundary.

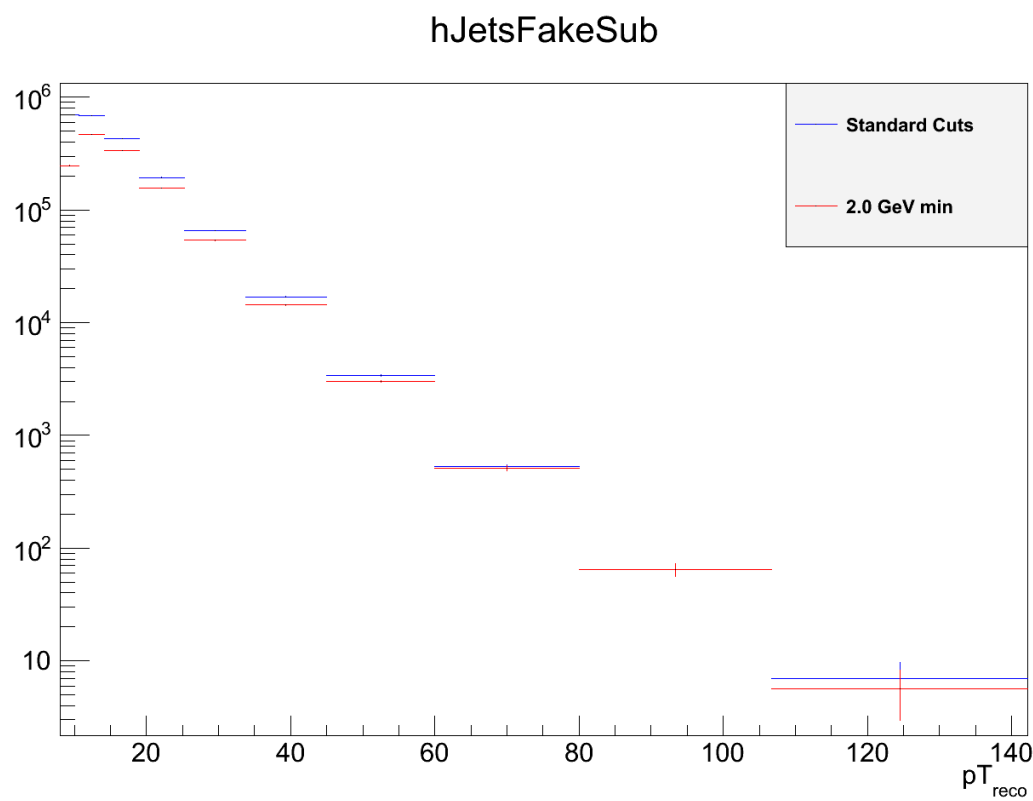


Figure 5.12: The unfolded with higher energy cuts (in red) is scaled up to match the default (blue) at high p_T .

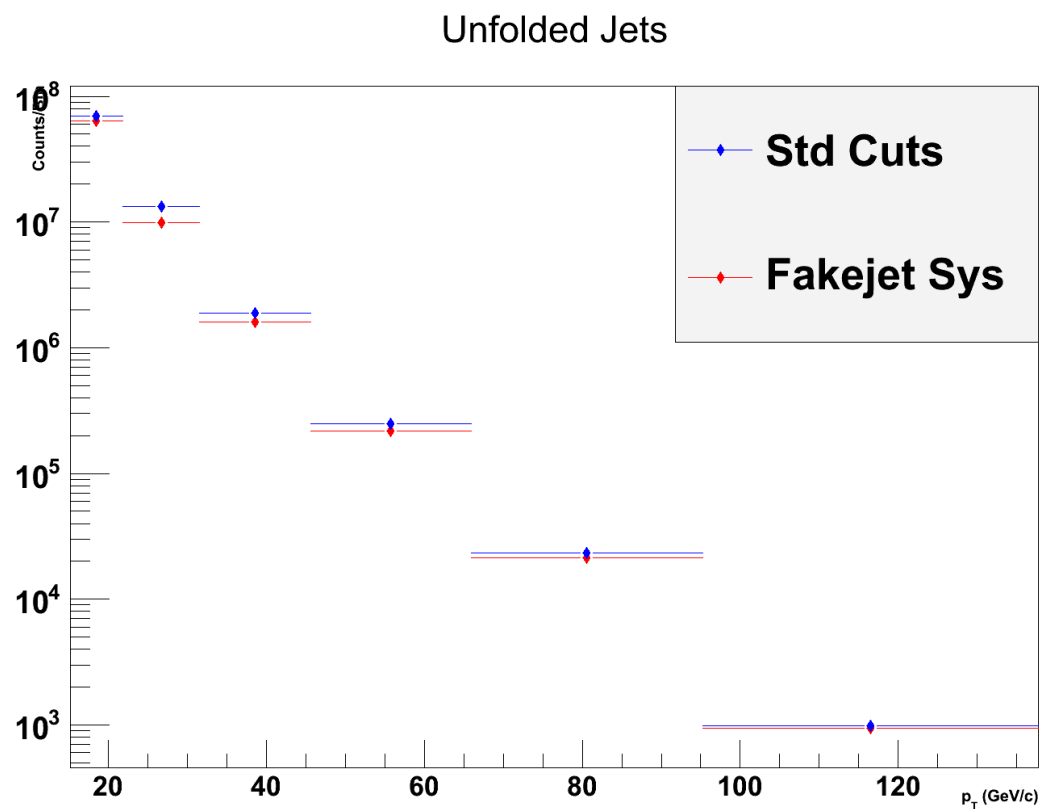


Figure 5.13: The unfolded with higher energy cuts (in red) compared to the default (blue).

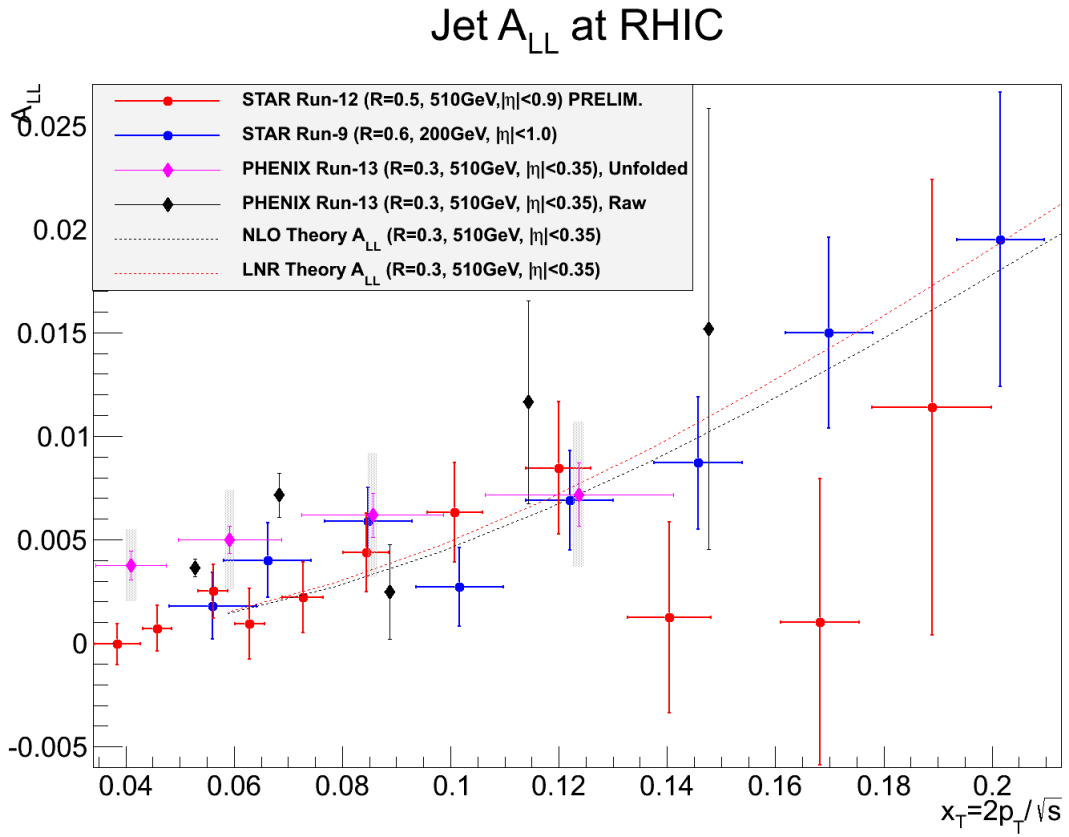


Figure 5.14: The STAR points, theory curves, and the raw and unfolded points are shown in this figure. The blue and red points are the previous STAR measurements, the dashed lines are from theory curves. The pink points are from the unfolded points. The grey band on the pink points is the unfolded systematic, discussed in Section 5.5. The range shown is within the range of high statistics.

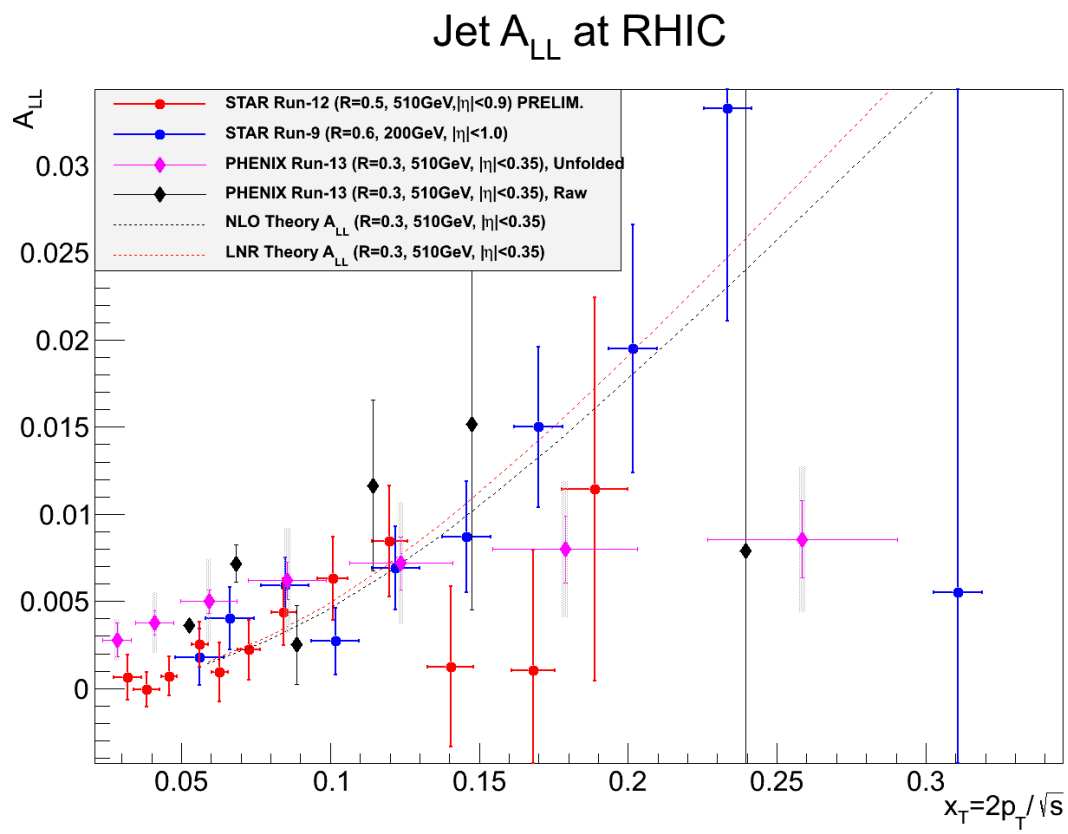


Figure 5.15: This shows the points of the larger $x_{T, True}$ range of Figure 5.14

BIBLIOGRAPHY

- [1] Aad, G. et al. (2012). Observation of a new particle in the search for the Standard Model Higgs boson with the ATLAS detector at the LHC. *Phys. Lett.*, B716:1–29.
- [2] Abe, F. et al. (1995). Observation of top quark production in $\bar{p}p$ collisions. *Phys. Rev. Lett.*, 74:2626–2631.
- [3] Adamczyk, L. et al. (2015). Precision Measurement of the Longitudinal Double-spin Asymmetry for Inclusive Jet Production in Polarized Proton Collisions at $\sqrt{s} = 200$ GeV. *Phys. Rev. Lett.*, 115(9):092002.
- [4] Adare, A. et al. (2011). Cross section and double helicity asymmetry for η mesons and their comparison to neutral pion production in p+p collisions at $\sqrt{s} = 200\text{GeV}$. *Phys. Rev.*, D83:032001.
- [5] Adare, A. e. a. (2013). Inclusive cross section and single transverse spin asymmetry for very forward neutron production in polarized $p+p$ collisions at $\sqrt{s}=200$ GeV. *Phys. Rev. D*, 88:032006.
- [6] Adcox, K. et al. (2003a). PHENIX central arm tracking detectors. *Nucl. Instrum. Meth.*, A499:489–507.
- [7] Adcox, K. et al. (2003b). PHENIX detector overview. *Nucl. Instrum. Meth.*, A499:469–479.
- [8] Adler, C., Denisov, A., Garcia, E., Murray, M. J., Strobele, H., and White, S. N. (2001). The RHIC zero degree calorimeter. *Nucl. Instrum. Meth.*, A470:488–499.

- [9] Adye, T. (2011). Unfolding algorithms and tests using RooUnfold. In *Proceedings, PHYSTAT 2011 Workshop on Statistical Issues Related to Discovery Claims in Search Experiments and Unfolding, CERN, Geneva, Switzerland 17-20 January 2011*, pages 313–318, Geneva. CERN, CERN.
- [10] Aizawa, M. et al. (2003). PHENIX central arm particle ID detectors. *Nucl. Instrum. Meth.*, A499:508–520.
- [11] Allen, M. et al. (2003). PHENIX inner detectors. *Nucl. Instrum. Meth.*, A499:549–559.
- [12] Aphecetche, L. et al. (2003). PHENIX calorimeter. *Nucl. Instrum. Meth.*, A499:521–536.
- [13] Ashman, J. et al. (1988). A Measurement of the Spin Asymmetry and Determination of the Structure Function $g(1)$ in Deep Inelastic Muon-Proton Scattering. *Phys. Lett.*, B206:364.
- [14] Aubert, J. J. et al. (1974). Experimental Observation of a Heavy Particle *J. Phys. Rev. Lett.*, 33:1404–1406.
- [15] Augustin, J. E. et al. (1974). Discovery of a Narrow Resonance in e^+e^- Annihilation. *Phys. Rev. Lett.*, 33:1406–1408. [Adv. Exp. Phys. 5, 141 (1976)].
- [16] Bai, M. (2010). Polarized Protons and Siberian Snakes. University of Virginia Nuclear Physics Seminar.
- [17] Bargmann, V., Michel, L., and Telegdi, V. L. (1959). Precession of the polarization of particles moving in a homogeneous electromagnetic field. *Phys. Rev. Lett.*, 2:435–436.
- [18] Bazilevsky, A. (2008). Rhic polarimetry. RHIC and AGS User’s Meeting.
- [19] Bjorken, J. D. and Glashow, S. L. (1964). Elementary Particles and SU(4). *Phys. Lett.*, 11:255–257.

- [20] Bloom, E. D. et al. (1969). High-Energy Inelastic e p Scattering at 6-Degrees and 10-Degrees. *Phys. Rev. Lett.*, 23:930–934.
- [21] Boyle, K. (2007). Double Longitudinal Spin Asymmetry in Neutral Pion Production in Polarized p+p Collisions at $s^{**}(1/2) = 200\text{-GeV}$ at PHENIX. *AIP Conf. Proc.*, 915:335–338. [,335(2007)].
- [22] Breidenbach, M., Friedman, J. I., Kendall, H. W., Bloom, E. D., Coward, D. H., DeStaebler, H. C., Drees, J., Mo, L. W., and Taylor, R. E. (1969). Observed Behavior of Highly Inelastic electron-Proton Scattering. *Phys. Rev. Lett.*, 23:935–939.
- [23] Bunce, G., Saito, N., Soffer, J., and Vogelsang, W. (2000). Prospects for spin physics at RHIC. *Ann. Rev. Nucl. Part. Sci.*, 50:525–575.
- [24] Cacciari, M., Salam, G. P., and Soyez, G. (2008). The Anti-k(t) jet clustering algorithm. *JHEP*, 04:063.
- [25] Cacciari, M., Salam, G. P., and Soyez, G. (2012). FastJet User Manual. *Eur. Phys. J.*, C72:1896.
- [26] Courant, E. (2008). Spin motion and resonances in accelerators and storage rings. Technical report. C-A/AP/292 V2.
- [27] de Florian, D., Sassot, R., Stratmann, M., and Vogelsang, W. (2008). Global analysis of helicity parton densities and their uncertainties. *Phys. Rev. Lett.*, 101:072001.
- [28] de Florian, D., Sassot, R., Stratmann, M., and Vogelsang, W. (2014). Evidence for polarization of gluons in the proton. *Phys. Rev. Lett.*, 113(1):012001.
- [29] Derbenev, Ya. S. and Kondratenko, A. M. (1973). Polarization kinematics of particles in storage rings. *Sov. Phys. JETP*, 37:968–973. [Zh. Eksp. Teor. Fiz. 64, 1918(1973)].
- [30] Ellis, J. and Jaffe, R. (1974). Sum rule for deep-inelastic electroproduction from polarized protons. *Phys. Rev. D*, 9:1444–1446.

- [31] Ellis, J. R. and Karliner, M. (1995). Nucleon spin. In *Prospects of spin physics at HERA. Proceedings, Workshop, Zeuthen, Germany, August 28-31, 1995*, pages 141–152. [,141(1995)].
- [32] et al., K. A. (2003). Construction and performance of the {PHENIX} pad chambers. *Nuclear Instruments and Methods in Physics Research Section A: Accelerators, Spectrometers, Detectors and Associated Equipment*, 497(23):263 – 293.
- [33] Field, R. (2002). Accessed: 2017-05-25.
- [34] Field, R. (2004). The universality of pythia tune a. FermiLab MC Workshop.
- [35] Group, P. D. Structure functions.
- [36] He, H.-x. (1997). Quark contributions to the proton spin and tensor charge.
- [37] Hemmick, T. Dc track quality.
- [38] Herb, S. W. et al. (1977). Observation of a Dimuon Resonance at 9.5-GeV in 400-GeV Proton-Nucleus Collisions. *Phys. Rev. Lett.*, 39:252–255.
- [39] Herrero, M. (1999). The Standard model. *NATO Sci. Ser. C*, 534:1–59.
- [40] Hocker, A. and Kartvelishvili, V. (1996). SVD approach to data unfolding. *Nucl. Instrum. Meth.*, A372:469–481.
- [41] Huang, H. and Alekseev, e. a. (2015). ”operation experience of p-carbon polarimeter in rhic”.
- [42] Huang, H. et al. (2003). Commissioning of RHIC p carbon CNI polarimeter. *Nucl. Phys.*, A721:356–359. [,795(2000)].
- [43] Huth, J. E. et al. (1990). Toward a standardization of jet definitions. In *1990 DPF Summer Study on High-energy Physics: Research Directions for the Decade (Snowmass 90) Snowmass, Colorado, June 25-July 13, 1990*, pages 0134–136.

- [44] I. Estermann, R. Frisch, O. S. (1933). Magentic moment of the proton. *Nature*.
- [45] Jaffe, R. and Manohar, A. (1990). The g1 problem: Deep inelastic electron scattering and the spin of the proton. *Nuclear Physics B*, 337(3):509 – 546.
- [46] Jager, B., Stratmann, M., and Vogelsang, W. (2004). Single inclusive jet production in polarized pp collisions at $O(\alpha_s^3)$. *Phys. Rev.*, D70:034010.
- [47] Kim, M. (2013). Run13 local polarimeter analysis in polarized p+p collisions at $\sqrt{s} = 510$ gev. Technical report.
- [48] Kponou, A., Zelenski, A., Kokhanovski, S., and Zubets, V. (2008). Sona transition studies in the rhic oppis. *AIP Conference Proceedings*, 980(1):241–247.
- [49] Kuti, J. and Weisskopf, V. F. (1971). Inelastic lepton - nucleon scattering and lepton pair production in the relativistic quark parton model. *Phys. Rev.*, D4:3418–3439.
- [50] MacKay, W. W. et al. (2003). Commissioning Spin Rotators in RHIC. *Conf. Proc.*, C030512:1697.
- [51] Mukherjee, A. and Vogelsang, W. (2012). Jet production in (un)polarized pp collisions: Dependence on jet algorithm. *Phys. Rev. D*, 86:094009.
- [52] Nakamura, T. (2002). Introduction to phenix beam beam counter (bbc). PHENIX Focus Talk.
- [53] NIST (2015). The nist reference on constants, units, and uncertainty.
- [54] Patrignani, C. et al. (2016). Review of Particle Physics. *Chin. Phys. C*40(10):100001.
- [55] Salam, G. P. and Soyez, G. (2007). A Practical Seedless Infrared-Safe Cone jet algorithm. *JHEP*, 05:086.
- [56] Soyez, G. (2009). Recent progress in defining jets. *Nucl. Phys. Proc. Suppl.*, 191:131–140.

- [57] Srednicki, M. (2007). *Quantum Field Theory*. Cambridge University Press.
- [58] T. Roser, e. a. (2002). *Accelerating and Colliding Polarized Protons in RHIC with Siberian Snakes*.
- [59] T. Roser, W.W. MacKay, e. a. (2006). Configuration Manual Polarized Proton Collider at RHIC, 2006.
- [60] Timilsina, A. (2016). Inclusive jet production in proton-proton and copper-gold collisions at $\sqrt{s_{NN}} = 200\text{gev}$.
- [61] Zelenski, A. (2016). High-intensity Polarized H- Ion Source for the RHIC Spin Physics.
- [62] Zelenski, A., Atoian, G., Ritter, J., Steski, D., Podolyako, F., Sorokin, I., Vizgalov, I., Klenov, V., Zubets, V., Davydenko, V., Ivanov, A., and Kolmogorov, A. (2014). The rhic polarized source upgrade. *Physics of Particles and Nuclei*, 45(1):308–311.
- [63] Zelenski, A. et al. (2005). Absolute polarized H-jet polarimeter development, for RHIC. *Nucl. Instrum. Meth.*, A536:248–254.